UNIVERSITÀ
DEGLI STUDI
DI PADOVA

Head Office: Università degli Studi di Padova

Department of Geosciences

Ph.D. COURSE IN: EARTH SCIENCES
SERIES XXXII

From Bedrock to Sediments: Insights on the Ross Sea Ice-Flow Dynamics Inferred from Detrital Data

Coordinator: Prof. Claudia Agnini
Supervisor: Prof. Massimiliano Zattin

Ph.D. student: Xia Li

CONTENTS

Abstract

The Ross Sea received about one third of the Antarctic ice. It is a crucial area to investigate the ice dynamics during the Cenozoic as it records the evolution of both the East Antarctic Ice Sheet (EAIS) and West Antarctic Ice Sheet (WAIS), whose variations are a direct response to climate change. Reconstructions of the ice flow models are mainly based on multi-proxy provenance analysis of glacigenic sediments but so far, a well-established model is not existing. There are still disputes of the different ice contribution between the EAIS and the WAIS, and the ice confluence in the Ross Sea. Thus, the main target of this study is to provide new inputs to build a robust model of Ross Sea ice flow during the Cenozoic.

This work is based on 48 samples collected across the Ross Sea and analyzed by apatite fission track (AFT) dating. More in detail, a first set of 16 samples is from the drilling core CIROS-2, whose stratigraphic range is from early Pliocene to Quaternary. A second group of 32 samples derives from 18 post-Late Glacial Maximum (LGM) piston cores drilled across the Ross Sea. The obtained fission-track data have been modelled with statistical tools (among them, the Multidimensional Scaling) and finally interpreted in terms of thermal evolution by the HeFTy software.

The AFT age data of CIROS-2 samples show a large range of ages but most of the grains fit well with two main age components at 24-42 Ma and 43-70 Ma whereas the other components are not regularly distributed through the well. This pattern indicates a mixture of provenance from different areas along the Transantarctic Mountains (TAM). Furthermore, it suggests glacial expansion over the McMurdo Sound during the Pliocene, and periodically ice invading and retreating in Pleistocene.

The data of post-LGM piston cores samples also show a large range of individual grain ages. The lack of systematic trends across the Ross Sea indicates the presence of multiple sources with a complex and differentiated erosional history. The presence of apatites younger than 21 Ma, clearly of volcanic origin, such as ages older than 230 Ma represent a significant signature for a source related to evolution of East Antarctica. Moreover, thermal modelling and the presence of apatites with cooling

ages of about 30-40 Ma reveal a main exhumation phase of the TAM during the Oligocene associated to the last phases of the West Antarctic Rift System. The spatial distribution of key marker apatites (e.g. younger than 21 Ma or older than 230 Ma) allows to identify the Central High as a major ice-flow divide. West of the Central High, the ice flow is from East Antarctica, with general northwards trend but with local flows from outlet glaciers, especially during ice sheet retreat phases. East of the Central High, sediments derived mainly by West Antarctica, with only minor contributions from the southernmost portion of the TAM and the lack of any significant input from the inner Marie Byrd Land.

As a whole, this work supports the idea of a WAIS-dominated ice flow model during the early Pliocene, an EAIS-dominated ice flow model during the late Pleistocene and an EAIS-WAIS balanced ice flow model during the Last Glacial Maximum.

Chapter 1

Introduction

This work aimed to investigate the ice flow dynamics across the Ross Sea in Antarctica through detrital apatite fission-track analysis. It is based on samples from the off-shore drillhole CIROS-2 in the McMurdo Sound and from piston cores across the entire Ross Sea.

In this chapter, an introduction on glacial dynamics through Antarctica and the Ross Ice Sheet is provided, the scientific questions are detailed and the structure and main contents of this thesis are briefly outlined.

1.1 Overview

1.1.1 The Antarctic ice and the sea level rise

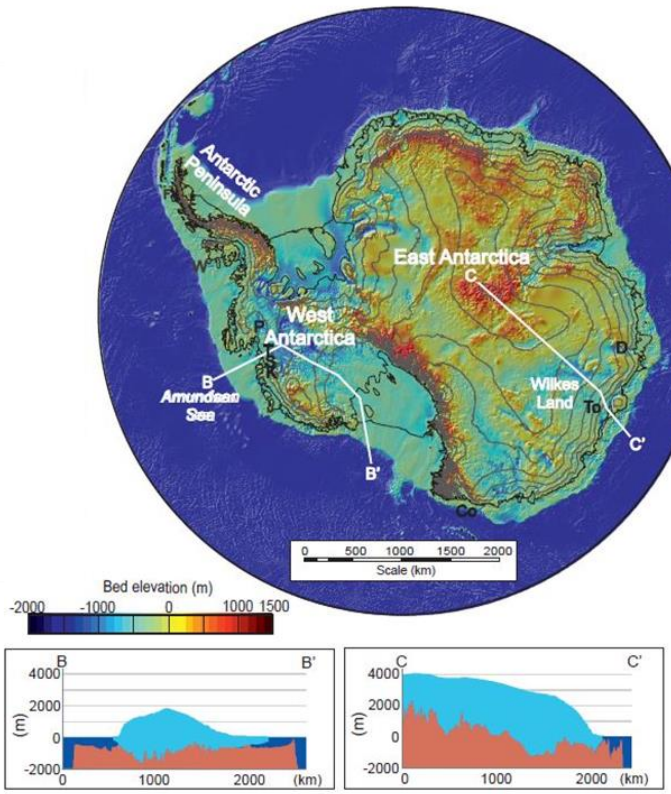

Fig. 1.1 Subglacial and seabed topography for Antarctica derived from digital

compilations. Blue areas highlight the marine-based parts of the ice sheets, which are extensive in Antarctica, Selected sections through the ice sheet show reverse bed gradients that exist beneath some glaciers in both ice sheets (Vaughan et al., 2013).

The Antarctic cryosphere is mainly made by two main components: The West Antarctic Ice Sheet and the East Antarctic Ice Sheet. A first difference between these ice sheets is about the thickness as East Antarctica ice is almost 3 kilometers thick whereas West Antarctica ice is almost 2 kilometers thick. However, what's more, most of West Antarctic Ice Sheet is grounded below the sea level and is much more sensitive to the temperature change of sea water than East Antarctic Ice Sheet (Fig. 1.1).

There is a general agreement on the fact that the Antarctic ice sheet is currently losing mass thus contributing to the sea level rising. The average ice mass change from the present assessment has been ~97 Gt yr^{-1} for a sea level equivalent of 0.27 mm yr^{-1} over the period 1993-2010, and ~147 Gt yr^{-1} corresponding to a sea level change of 0.41 mm yr^{-1} over the period 2005-2010 (Vaughan et al., 2013) (Fig. 1.2). Simply to say, the ice loss of Antarctica became faster in recent years.

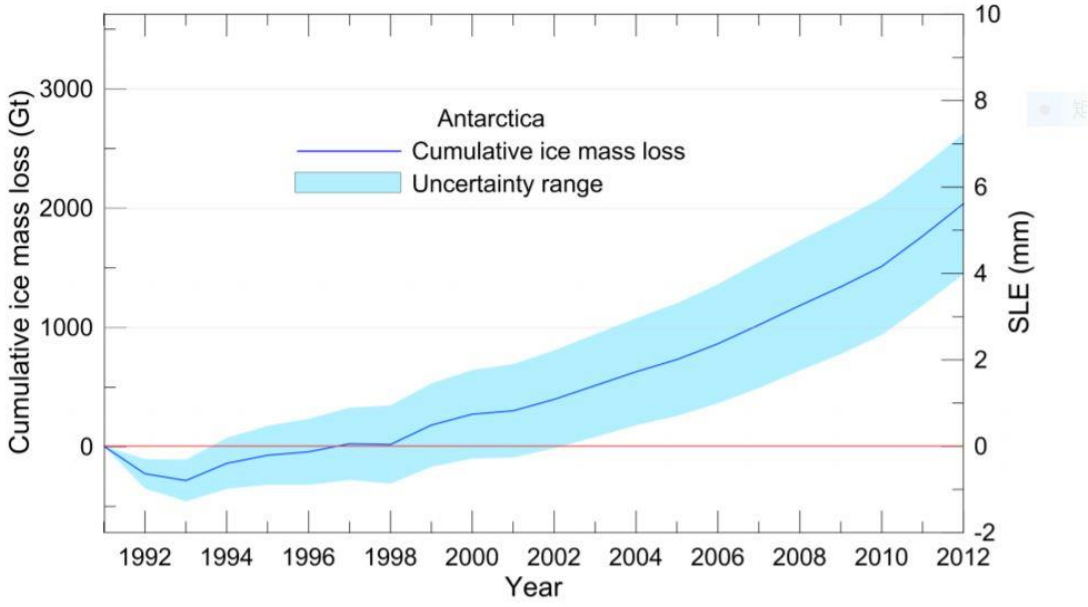

Fig. 1.2 The cumulative ice mass loss from the Antarctic ice sheet over the period 1992-2012 (Vaughan et al., 2013).

Actually, sea level changes occur over a wide range of spatial and temporal scales. There are many factors of contribution which makes it an integral measure of climate

change (Milne et al., 2009; Church et al., 2010). The expansion of the ocean due to warming is the dominate contributor to contemporary sea level change although the transfer of water currently stored on land to the ocean, particularly from land ice (glaciers and ice sheets), can be particularly important (Church et al., 2011a). The ice loss from glaciers between 1993 and 2009, measured in terms of sea level equivalent (excluding the glaciers peripheral to the ice sheets), is estimated to be of 13 mm. As shown in Fig. 1.3, the cumulative sea level equivalent from glaciers and the ice sheets in Greenland and Antarctic strongly contributes to sea level rise in recent decades.

Any realistic prediction of future sea-level changes needs therefore of a careful reconstruction of past changes in thickness and extent of the Antarctic ice sheets which represents the main input data for numerical models (Anderson et al., 2014).

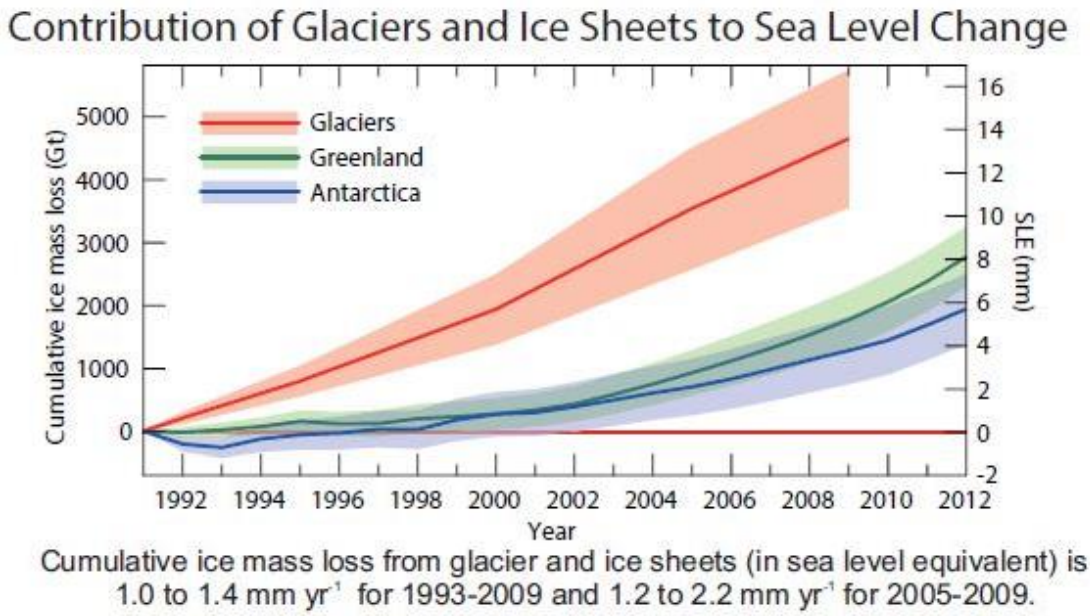

Fig. 1.3 Sea level equivalent rise from ice loss from the ice sheets of Greenland and Antarctica and continental glaciers except those in the periphery of the ice sheets. (Vaughan et al., 2013)

1.1.2 Overview of the Ross Ice Sheet

The Ross Sea received about one third of the Antarctic ice. It is a crucial area to investigate the ice dynamics of Antarctica as it records the evolution of both the East and West Antarctic Ice Sheets, whose variations are a direct response to climate change. The catchment for the Ross Sea sector today includes ~$1.65*10^6$ km^2 from the

East Antarctic Ice Sheet (EAIS), and $1.65*10^6$ km^2 from the West Antarctic Ice Sheet (WAIS) (Rignot et al., 2008).

The ice-flow dynamics is strongly controlled geomorphology of the Ross Sea bottom. It is characterized by 6 northeast trending troughs separated by the so-called Mawson (MB), Crary (CB), Pennell (PB), and Ross (RB) banks in the western Ross Sea and less prominent ridges in the east. The continental shelf has gentle gradients, with a depth seaward of about 500 m and a shelf break at 500-600 m (Fig. 1.4) (Anderson et al., 2014).

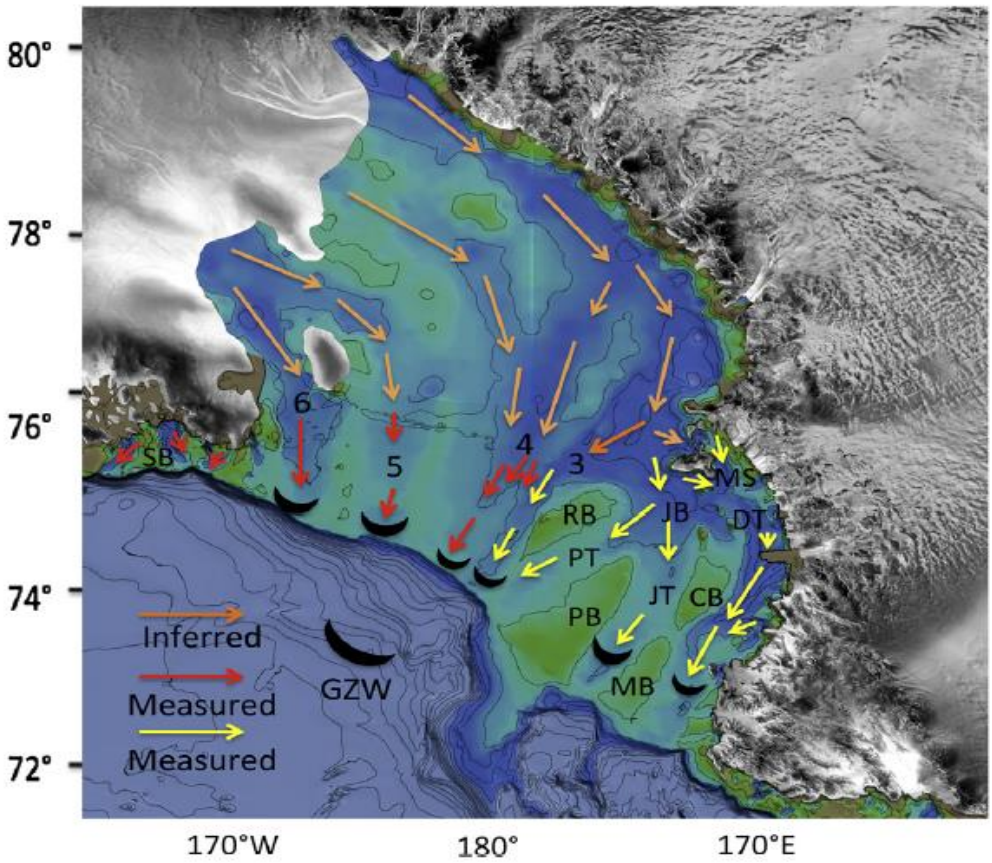

Fig. 1.4. Paleo-drainage map for the maximum ice sheet advance based on combined sediment provenance data and on the orientations of linear subglacial geomorphic features. The boundary between ice draining East Antarctica (yellow arrows) and ice draining West Antarctica (red arrows) is situated at approximately 180 longitude. The orange arrows reflect inferred paleodrainage in the area beneath the Ross Ice Shelf, which is based on locations of troughs. MS = McMurdo Sound, DT = Drygalski Trough, CB = Crary Bank, JB = JOIDES Basin (Trough), JT = JOIDES Trough, MB = Mawson Bank, PB = Pennell Bank, PT = Pennell Trough, RB = Ross Bank, SB = Sulzberger Bay and the numbers 3, 4, 5 and 6 correspond to the numbering system used by Mosola and Anderson (2006) to designate troughs. (Anderson et al., 2014).

The position of the maximum ice extent in the Ross Sea has been constrained by identifying the boundary between subglacial and glacial–marine sediment (Kellogg et al., 1979; Anderson et al., 1992; Licht et al., 1996, 1999; Domack et al., 1999), as well as the geometry of sedimentary packages and shelf morphologic features produced by glacial activity (Anderson et al., 1992; Shipp et al., 1999). Last Glacial Maximum (LGM) till thicknesses is variable across the Ross Sea, with the thickest strata occurring in the eastern Ross Sea, central Ross Sea, and on the outer shelf (Shipp et al., 1999). LGM sediments of western Ross Sea exhibit variable thickness, with LGM till generally confined to areas south of Coulman Island (Licht et al., 1996, 1999; Domack et al., 1999; Shipp et al., 1999). The position of maximum grounded ice extent in the eastern Ross Sea and central Ross Sea approximately follows the profile of the continental shelf break (Anderson, 1999; Shipp et al., 1999; Licht and Andrews, 2002). Maximum ice extent in the western Ross Sea, not absolutely arrived the shelf break indicates that the Ross Ice sheet did not reach an equilibrium position during the LGM (Licht et al., 2004, 2005).

Discriminating the contribution of the WAIS and EAIS to the Ross Ice Sheet and its variations in time since the formation of the Antarctic ice sheets has been object of research in recent years. This is of high relevance because WAIS and EAIS have different features and would respond differently to climate changes (Hollin, 1962; Hughes, 1973; Bindschadler and Scambos, 1991; MacAyeal, 1992; Alley and MacAyeal, 1993; Anderson, 2002). EAIS ice flows come from big outlet glaciers through the Transantarctic Mountains. WAIS, grounded under the sea level surface, is drained by rapidly moving ice streams and fringed by floating ice shelves (Hughes, 1977).

Although a relevant number of numerical modelling studies (Pollard and DeConto, 2009), the relative role and the stability of the ice sheets is still debated. Overall, the ice-flow evolution during the LGM in the Ross Sea has been interpreted according to 3 different models (Fig. 1.5): (1) WAIS-dominated model, based mainly on provenance studies, that predicts a flow from WAIS to a relatively narrow drainage along the western Ross Sea coastline (Stuiver et al., 1981); (2) WAIS-EAIS balanced model, in which the confluence of West Antarctic ice and East Antarctic ice occurs in the central Ross Sea and ice contribution from East Antarctic and West Antarctic is equivalent (Licht and Fastook, 1998; Denton and Hughes, 2000; Licht et al., 2005); (3) EAIS-dominated model, based on numerical modelling, in which the WAIS strongly

influenced the eastern Ross Sea and the EAIS contributed with most of the ice to the central and the western Ross Sea (Golledge et al., 2012). The definition of ice flow pathways during the LGM is highly complicated by repeated ice advance and retreat, the huge sea area and low sample density, despite several hundred sediment cores have been collected. A major advance in understanding the glacial history came with the development of multibeam swath bathymetry (Shipp et al., 1999, 2002; Mosola and Anderson, 2006; Bart and Cone, 2012), assuming that the present-day geomorphic features formed during the most recent glacial advance. However, the diachronicity of the expansion and retreat of the ice sheets through the Ross embayment such as the very different physiographic settings and the lack of a precise reliable radiocarbon ages preclude from unambiguous reconstructions.

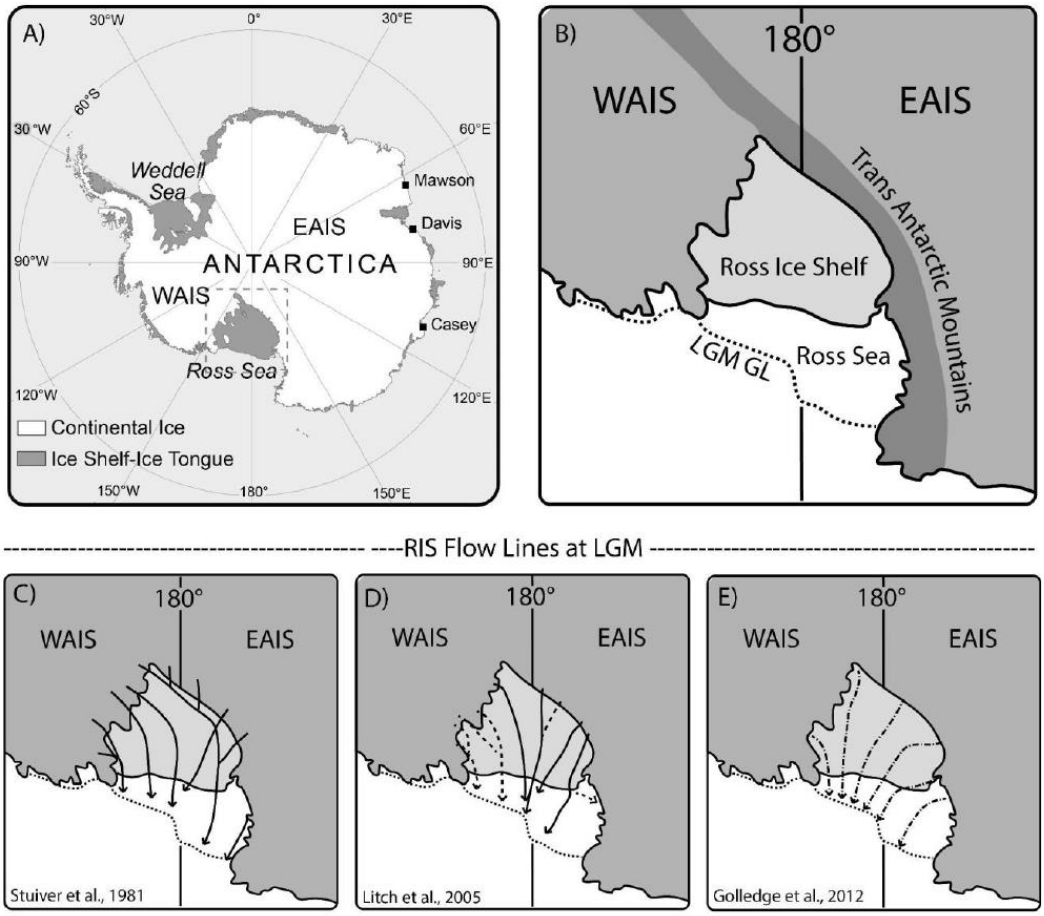

Fig. 1.5 A) Antarctica map, with study area (Ross Sea) indicated by the dashed gray perimeter; B) Detail of the Ross Sea, with the dotted line indicating the limit of the Ross Ice Sheet at the last glacial maximum (LGM); C), D) and E) represent three different interpretations of the flow lines during the LGM. C) and D) are based on provenance studies, whereas E) is based on numerical modelling (Stuiver et al., 1981; Licht et. al, 1998; Denton et. al, 2000; Licht et al., 2005; Golledge et al., 2012).

1.1.3 Overview of ice flow dynamics study through provenance analysis

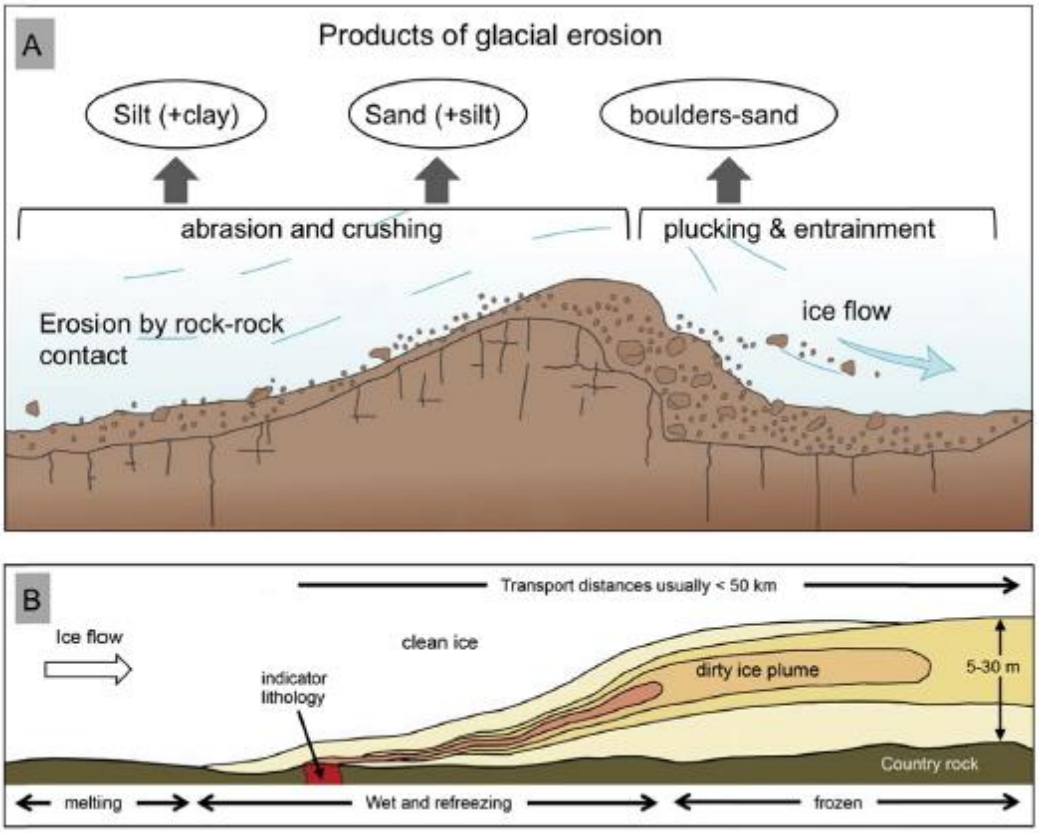

Fig. 1.6 Schematic diagram showing influence of bed roughness on glacial erosion. (A) Rock-rock contacts cause abrasion and crushing which typically produce sand-clay sized sediment whereas larger size fractions are produced by plucking (Boulton, 1978; Haldorsen, 1981). These processes are observed at a variety of scales. Entrained debris may move along the ice-bed contact or as englacial debris bands. (Base image - Pearson Prentice Hall, Inc., 2005). (B) Longitudinal cross section along ice flow showing sediment entrainment and dispersal by basal freeze on (modified from Hooke et al., 2013). Darker shading shows higher debris concentrations. The englacial plume collapses to a deposit <10 m thick (Licht and Hemming, 2017).

The above described models arise some key questions: how could we define a more precise ice flow pathway? Is it possible to derive information about glacial dynamics from a provenance approach? In fact, as the glaciers were expanded, they crushed and redistributed bedrocks. Transportation paths of glacigenic sediments could be therefore a valuable indicator of ice-flow paths (Fig. 1.6).

"Sediment provenance" or "provenance analysis" in the most general sense is the

reconstruction of the origin of sediment, that is the sources and processes on the landscape from which the sediment was derived. Provenance analysis has been widely used in glaciated areas of the northern hemisphere for both academic studies of ice sheet history and applied science such as mineral exploration, but it has only begun to be widely used in Antarctica in the past decade (Licht and Hemming, 2017).

Almost 98% area of Antarctica is covered by ice and thus exposure of bedrock is very limited to small areas, making provenance study very challenging. Reconstructions of Antarctic provenance must rely heavily on the glacigenic sediment compositions and textures to make inferences about the geology and geochronology of ice-covered areas. This approach is aided by comparison to the limited exposed outcrops and geophysical imaging beneath ice cover to characterize the sediments as tracers of ice flow (Licht and Hemming, 2017).

A valuable aid is represented by detrital geochronology and thermochronology that allow inferences about the location, age, and exhumation history of source terrains of sediments transported by ice. Because such data are sensitive to variations in the ice-flow patterns, they provide information for the reconstruction of ice sheet dynamics over time (Zattin et al., 2012).

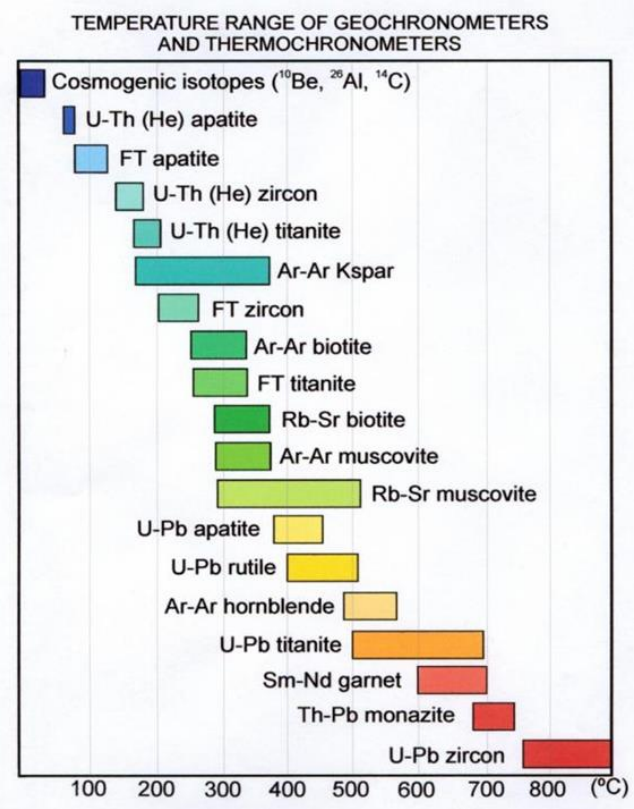

C

Fig.1.7 Nominal closure temperatures of various geochronometers and thermochronometers in current use (Cloetingh et al., 2007).

Apatite is a common accessory mineral in a wide range of rock types. The fission-track system in apatite is widely used as a thermochronometer (Gallagher et al., 1998; Zattin et al., 2010, 2014). The temperature above which the fission tracks are annealed in apatite depends on the cooling rate as well as the composition of the apatite, but is approximately 100°C (Fig. 1.7), so the fission-track age represents approximately the last time the apatite was at 3-4 km depth (for geothermal gradients of 35 to 25 °C/km respectively). Thermal modelling and statistic data processing of fission-track dataset make it to be a robust effective solution of source-to-sink signals in the condition of bad bedrock exposure as the Antarctica is poorly known.

1.2 Goals of the study

The main goal of this work is to provide reliable information for a reconstruction of ice flow dynamics of the Ross Sea in Antarctica. More in detail:

1. Most offshore drilling projects are located in McMurdo Sound in the western Ross Sea, providing important information of the ice flows in this area. The first goal of this study is to define the pathways of ice in the western Ross Sea in the last 5 Ma through the analysis of the stratigraphic record of the well CIROS-2.
2. A strong debate on the different contribution of East Antarctica and West Antarctica to ice flow in the Ross Sea during the LGM is still ongoing, especially about the confluence of ice near longitude 180° in the central Ross Sea. The second goal of this study is therefore to investigate the ice flow pattern in the central Ross Sea through samples from piston cores drilled all across the Ross Sea.
3. The third goal of this study is to explore the exhumation history of the Transantarctic Mountains (TAM) and their contribution to the detritus transported to the Ross Sea by the EAIS through the outlet glaciers.

1.3 Thesis outlines

Chapter 1 provides an overview of the rationale of the thesis and its goals, giving a

brief introduction to Antarctica, the ice-sheet dynamics and the study tools.

Chapter 2 is a presentation of the materials and methods used in this thesis.

Chapter 3 presents the results of the first part of the work. It is focused on the ice flow pathways of the western Ross Sea during the last 5 Ma, based on detrital apatite fission-track data from samples from the drillhole CIROS-2. The content of Chapter 3 is given by a paper which has been published in Terra Nova. Additional information not included in the paper is provided in Appendix.

Chapter 4 is about the results of the second part of the work. It is focused on discovering the fission-track signatures of different sources for the Ross Sea ice flows during the Last Glacial Maximum, through the analysis of samples from piston cores across the Ross Sea. The content of Chapter 4 constitutes another paper submitted to the Geochemistry, Geophysics, Geosystems.

Chapter 5 gives an overview of the results obtained in this thesis.

Appendix include data repository of Chapter 3 and data repository of Chapter 4.

Chapter 2

Materials and Methods

This work is based on 48 samples collected across the Ross Sea and analyzed with apatite fission-track dating. In this chapter, details of the samples are described and a general explanation of analytical methods are provided. Main references for Methods are the review papers of Reiners and Ehlers (2005), Fitzgerald and Malusà (2018), Vermeesch (2013).

2.1 Materials

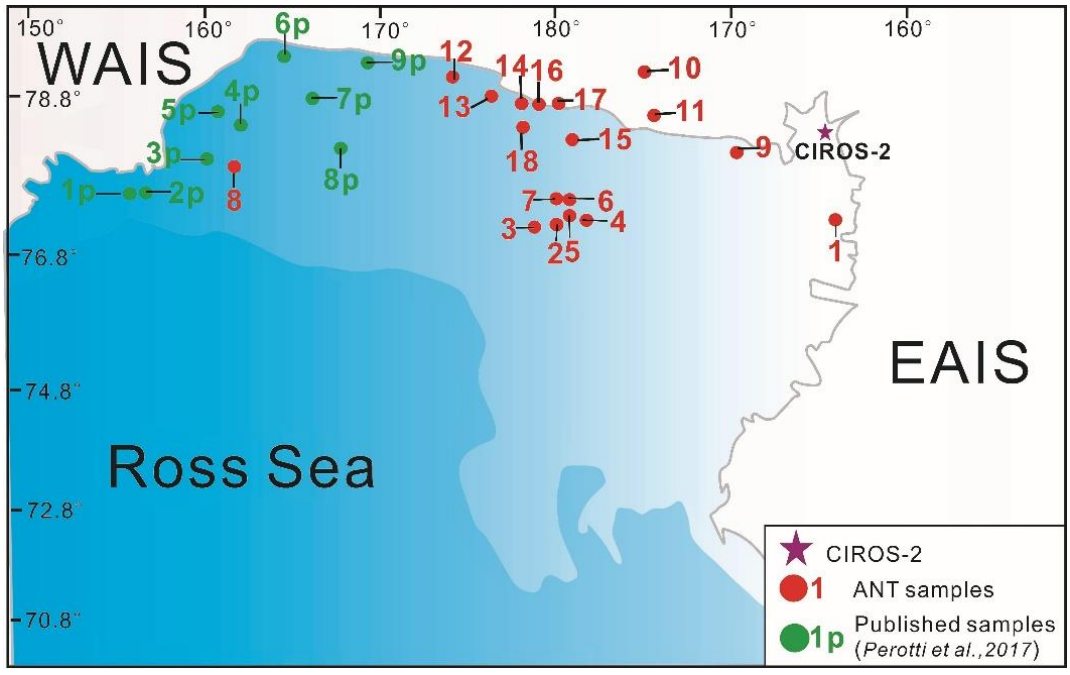

Fig. 2.1 Location of piston cores and CIROS-2

The 48 samples were divided into 2 groups. One group is given by 16 samples from the drilling core CIROS-2 which range from early Pliocene to Quaternary. The other group is made by 32 samples from 18 post-LGM piston cores drilled across the Ross Sea (Fig. 2.1).

2.1.1 Samples from CIROS-2

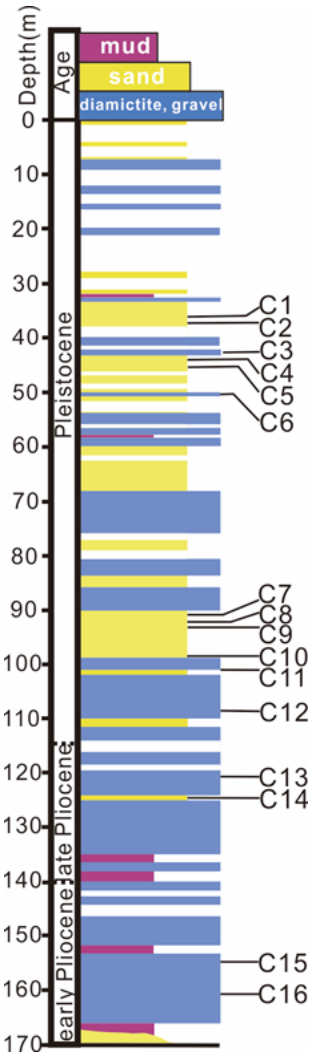

Fig. 2.2 The stratigraphy of CIROS-2 and samples distribution

CIROS-2 was drilled in 1984 in the sea ice off the Victoria Land Coast on the western shelf of McMurdo Sound, at latitude 77º41'S and longitude 163º32'E, and at water depth of 211 m (Fig. 2.2; Barrett and Scientific Staff, 1985). CIROS-2 is proximal to the East Antarctic ice sheet (EAIS): in fact, it is located only 1.2 km east of the floating tongue of the present-day Ferrar Glacier, which flows from the polar plateau through the Transantarctic Mountains (TAM) and drains the East Antarctica into a fjord. The stratigraphy of CIROS-2 core ranges from Lower Pliocene to Quaternary (Ehrmann and Polozek, 1999; Sandroni and Talarico, 2006). It was drilled down to 166.7 m below the sea floor and its sedimentary succession can be divided into two

main sequences (Fig. 2.2): a Pliocene lower sequence (from 167.7 to about 114 mbsf), dominated by diamictites, and a Pleistocene upper sequence, consisting of an alternation of sandstones and diamictites. The lower sequence is characterized by the presence of clasts dominated by monzogranites/granodiorites (Granite Harbour Intrusive Complex) and vesicular basalts (McMurdo Volcanic Group), with minor occurrences of gabbros/dolerites (Ferrar Supergroup), sandstones (Beacon Supergroup) and metamorphic rocks (Koettlitz Group). The upper sequence is dominated by tonalites, with very minor occurrences of gabbros/dolerites, strongly altered basalts and metamorphic rocks (Sandroni and Talarico, 2006). Within the Pliocene interval, the massive diamictites present were interpreted as lodgment tills deposited beneath an ancestral Ferrar Glacier, interbedded with mudstones indicative of a distal glaciomarine setting. In contrast, the Pleistocene diamictites were interpreted as waterlain tills related to the advances of grounded Ross Sea ice entering Ferrar Fjord and leading to the formation of an ice-dammed lake, where sand sedimentation occurred (Barrett and Hambrey, 1992; Hambrey and Barrett, 1993; Sandroni and Talarico, 2006).

2.1.2 Samples from piston cores in the Ross Sea

The 32 samples are from 18 piston cores were obtained from the Antarctica Research Facility at Florida State University. They were drilled by different scientific cruises across the Ross Sea: DF78, NBP94-07, NBP94-01, NBP96-01, DF62-01, DF76, NBP00-01, NBP94-07, NBP95-01 (Table 2.1). Subsamples for analysis were chosen from cores retrieved landward of the Last Glacial Maximum grounding line in the Ross Sea. Actually, most of cores are distributed in the central Ross Sea (Piston core 2,3,4,5,6,7,12,13,14,15,16,17) near the longitude 180°. Several cores located in the western Ross Sea (Piston core 1,9,10.11). Piston core 8 located in the eastern Ross Sea. Details on location are shown in Table 2.1. Besides, samples from 9 Piston cores (P1-P9) located in the eastern Ross Sea have already published by Perroti et al. (2017) (Fig. 2.1).

All of cores in this work yield samples of a stratigraphic age younger than the Last Glacial Maximum. Each of the sample, collected in the sand levels, integrates about 5 cm of materials: Piston core 1 samples from the core depth (25-32cm, 102-107cm,

187-192cm, 242-247cm,297-302cm); Piston core 2 samples from the core depth (0-3cm); Piston core 3 (12-17cm, 35-40cm); Piston core 4 (12-17cm, 126-130cm, 184-188cm); Piston core 5 (77-82cm, 92-97cm, 132-137cm, 154-159cm, 235-239cm); Piston core 6 (5-10cm, 73-75cm, 95-100cm); Piston core 7 (1-3cm, 81-84cm, 360-365cm); Piston core 8 (18-24cm); Piston core 9 (28-32cm); Piston core 10 (245-248cm); Piston core 11 (280-287cm); Piston core 12 (579-583cm); Piston core 13 (100-105cm); Piston core 14 (45-51cm); Piston core 15 (179-187cm); Piston core 16 (0-5cm); Piston core 17 (94-98cm); Piston core 18 (100-105cm) (Table 3.1).

Although the gravel fraction of till can provide valuable provenance information, it was not included in this study because the core samples did not contain enough gravel to provide statistically meaningful results.

Table 2.1 location of piston cores in the Ross Sea

Sample name	Cruise	Core	Latitude	Longitude	Water depth	Core length
1	DF78	014-PC	-76.5	164	424	334
2	NBP94-07	070-PC	-76.405	-179.657	512	308
3	NBP94-07	093-PC	-76.76	178.535	298	359
4	NBP94-01	027-PC	-76.522	178.881	312	235
5	NBP94-07	078-PC	-76.493	-179.963	375	270
6	NBP94-07	079-PC	-76.487	179.949	295	151
7	NBP96-01	002-JPC	-76.452	179.881	373	419
8	NBP96-01	006-JPC	-77.222	-161.476	649	341
9	DF62-01	005-PC	-77.3333	170	805	76
10	DF78	012-PC	-78.267	175.25	538	271
11	DF76	001-PC	-77.45	174.8	695	544
12	DF76	003-PC	-78.2	-174.183	558	671
13	NBP00-01	001-PC	-78.019	-176.252	578	237
14	NBP94-07	039-PC	-77.924	-178	694	103
15	NBP95-01	017-PC	-77.452	179.05	732	202
16	NBP94-07	041-TC	-77.921	-178.26	716	32
17	NBP94-07	043-PC	-77.917	-178.822	725	241
18	NBP94-07	051-PC	-77.659	-177.789	678	125

2.2 Methods

2.2.1 Apatite fission-track dating and modelling

The fission-track method is based on the accumulation of narrow damage trails in uranium-rich mineral grains (e.g., apatite, zircon, titanite) and natural glasses, which

form as a result of spontaneous nuclear fission decay of ^{238}U in nature. It provides detailed information on the low-temperature thermal histories of rocks (below 120±°C for tracks in apatite and 280±°C for zircon).

2.2.1.1 Formation of fission tracks

The formation of fission tracks occurs when highly charged nuclear particles pass through insulating solids during radioactive decay (Wagner, 1968). In geological scale, natural or spontaneous tracks are produced almost exclusively by spontaneous fission of ^{238}U as other naturally forming heavy isotopes (e.g. ^{232}Th and ^{235}U) have such long fission half-lives, they cannot form a significant source for spontaneous track formation (Table 2.2) (Wagner and Van den Haute, 1992).

Table 2.2 Relative abundances of U isotopes, total half-life and half-life due to spontaneous fission decay process

	Relative Abundance (with respect to ^{238}U)	Half life (yr)	Half life for spontaneous fission (yr)
^{232}Th	4^{d}	1.40×10^{10}	1.0×10^{21}
^{234}U	5.44×10^{-5}	2.46×10^{5}	1.5×10^{16}
^{235}U	7.25×10^{-3}	7.04×10^{8}	1.0×10^{19}
^{238}U	1	4.47×10^{9}	8.2×10^{15}

The formation of fission tracks is generally explained by the ion spike explosion model (Fleischer et al., 1965; 1975). When a heavy unstable nucleus decays by spontaneous fission, it splits into two nuclear fragments which are pushed away to each other by a combination of energy released by the nuclear fission and coulomb repulsion forces. The passage through the crystal lattice of the two positively charged nuclear fragments induces a change of electrostatic charge in the surrounding lattice region. Charge variation induces, in turn, widespread dislocation of atoms from their lattice positions, generating the high defect density which characterizes fission tracks (Figure 2.3).

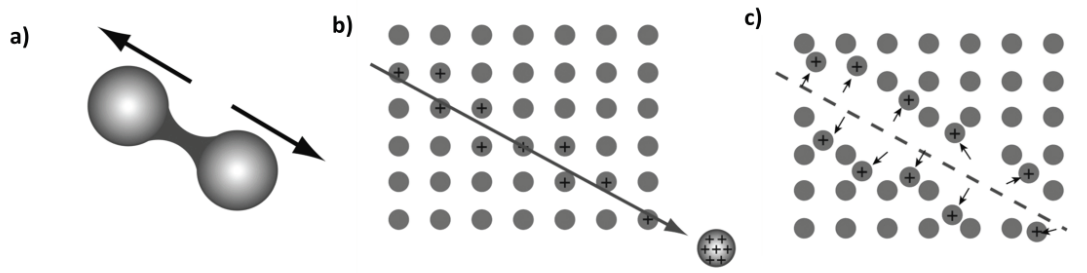

Fig. 2.3 The “Ion Explosion Spike” model for fission track formation (from Fleischer et al., 1975).

2.2.1.2 Observation of fission tracks

Unetched fission track is called latent track. Generally, latent tracks represent a cylindrical amorphous material in a crystalline matrix, with a sharp amorphous-crystalline transition. The elastic strain field around the disordered core extends a short distance into the matrix, likely with $1/R^2$ dependence (Bursill and Braunshausen 1990; R, radial distance), with no evidence for structural defects in its vicinity. Depending on the ion energy loss, the cross section of the track has a nearly circular shape with 6-10 nm widths in apatite (Paul, 1993), ~8 nm in zircon (Bursill and Braunshausen, 1990) and ~4-10 nm in muscovite mica, (Vetter et al. 1998). The track is a linear, continuous feature and has approximately a uniform diameter along most of its length. For its entire range, however, the track is a cylinder over a certain length and has a tapering-down in diameter near its end (Dunlap et al., 1997; Chadderton, 2003), which may be the case of both terminals of a fission track (Carlson, 1990).

Due to limited widths of only several nm, latent fission tracks can be viewed only by TEM (transmission electron microscopy) and other high-resolution microscopic techniques. However, latent tracks are conveniently scanned just in the condition of high track densities (i.e., $>10^{10}cm^{-2}$), which is generally not the case of terrestrial minerals such as apatite and zircon.

Chemical etching is the effective way to enlarge fission track as the disordered region of the track core is more rapidly dissolved than the surrounding undamaged bulk material, due to its lowered binding energy. Chemical etching is conducted by immersing a dielectric material into a particular reagent under strictly controlled temperature and time conditions. Therefore, only tracks that intersect the material’s

surface are etched and enlarged for observation (Fleischer et al., 1975; Durrani and Bull, 1987; Wagner and Van den haute, 1992) (Fig. 2.4). In theory, when all tracks that intersect the original surface become clearly visible under the optical microscope, etching should be stopped. Etching should be continued until the tracks that are etched most slowly and weakly become visible under the microscope, so that the number of etched tracks is approximately equal for all crystallographic orientations (Gleadow, 1981; Sumii et al., 1987)

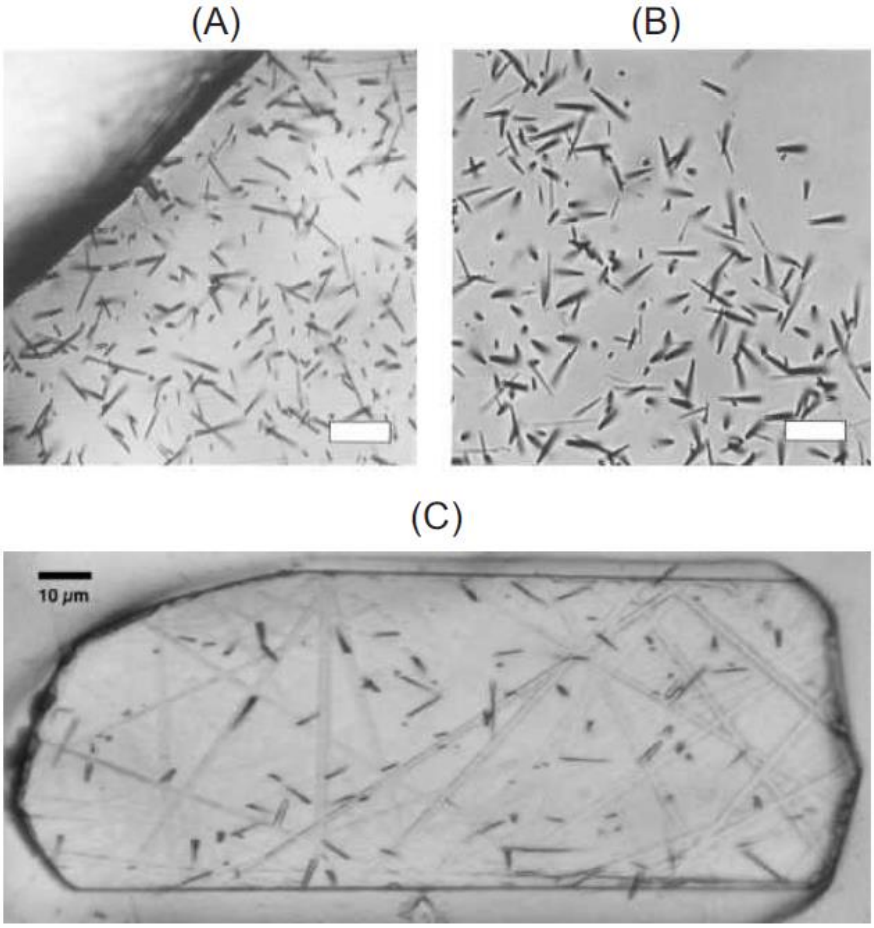

Fig. 2.4 Photographs of etched fission tracks viewed under optical microscope. (A) Spontaneous tracks revealed on a polished internal surface of ~27.8 Ma Fish Canyon Tuff zircon. The crystallographic c-axis lies approximately vertical. (B) Induced tracks implanted on a muscovite detector (Brazilian Ruby clear) that were derived from the region of the photograph (A). (C) Spontaneous tracks on a polished internal surface of ~33 Ma apatite crystal. The c-axis lies approximately horizontal. Scale bars are 10 μm (Tagami and O'Sullivan et al., 2005).

Confined tracks are those entirely contained within the boundaries of the crystal. They

can be divided into two categories: Track-in-Track (TINT) and Track-in-Cleavage (TINCLE) (Lal et al., 1969). Laslett et al. (1982) proved that the true length distribution of fission tracks can be obtained from the measurement of "horizontal" confined tracks (Fig. 2.5). The most popular approach at present is therefore consisting in the measurement of the length distribution of spontaneous fission tracks, given that this parameter is indispensable for quantitative modeling of rocks' thermal histories as well as for determining FT thermal annealing kinetics.

Fig. 2.5 Confined horizontal tracks: "Track in cleavage" (TINCLE) and "Track in track" (TINT) (Tagami and O'Sullivan et al., 2005).

2.2.1.3 Grain age calculation

At present, external detector method (EDM) is the most widely accepted method to date mineral grains with fission-track analysis (Fig. 2.6). It is based on the measurement of two different track densities: spontaneous tracks (ρ_S) and induced tracks (ρ_I). In mineral grains, spontaneous fission tracks are etched and revealed on an internal polished surface. At the same time, induced fission tracks are recorded on an external detector (e.g., a low-U thin muscovite mica sheet) that is stably attached onto the etched grain surface during neutron irradiation. Therefore, ρ_S and ρ_I are measured on the internal mineral surface and on the external detector surface respectively. The advantage of this procedure is that FT ages can be determined on individual mineral grains. It is particularly vital to date grains with variable ages and compositions within individual samples. Previous studies of both sedimentary rocks (Green et al., 1989a; Hurford and Carter, 1991; Burtner et al., 1994; Barbarand et al., 2003a) and some

basement rocks (O'Sullivan and Parrish, 1995) have shown that significant variations in grain ages can occur within individual samples, and thus it is imperative to date individual grains age instead of simply identifying a bulk sample age.

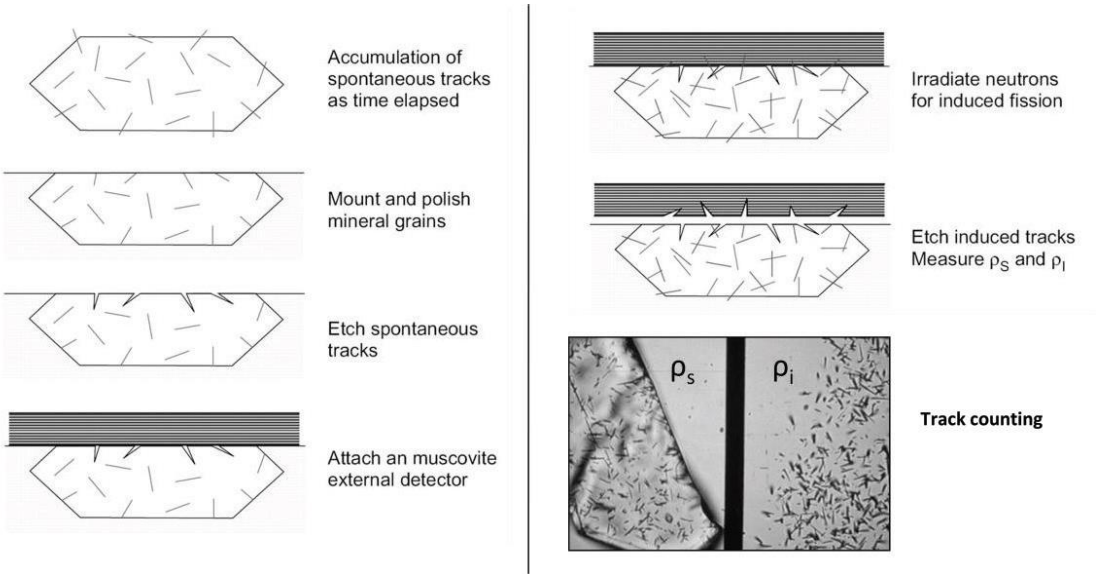

Fig. 2.6 Schematic illustration of the experimental steps involved in the external detector method. The technique is by far the most popular dating procedure for mineral samples collected from a variety of geologic settings. ρ_S = surface density of etched spontaneous fission tracks; ρ_I = surface density of etched induced fission tracks (Tagami and O'Sullivan, 2005).

The AFT age of a single apatite grain determined by EDM method is given by:

$$t = \frac{1}{\lambda_\alpha} \log\left[\left(\frac{\lambda_\alpha}{\lambda_f}\right)\left(\frac{N_s}{N_i}\right) \cdot I \cdot \sigma \cdot \phi + 1\right]$$

t= grain age, λα = α decay costant, λ_f= fission decay costant, Ns= number of spontaneous tracks, Ni = number of induced tracks, I= 7.2527 x 10-3, Φ= neutron fluence (neutrons/cm2)), σ = cross-section

The radial plot is the most widely used graphical method at present, in which the uncertainty in a single age estimate is isolated so that it is easier to judge the variation in ages between crystals. When multiple age populations are existing, statistical models can be applied to estimate the age components, (Galbraith and Green, 1990; Brandon, 1992; Galbraith and Laslett, 1993) (Fig. 2.7). This technique is essential for sedimentary provenance studies ("detrital FT thermochronology"; see Hurford and Carter, 1991; Carter and Moss, 1999; Garver et al., 1999; Ruiz et al., 2004) as well as

to identify and extract the “essential age” in dating volcanic ash layers (Naeser et al., 1973; Gleadow, 1980; Kowallis et al., 1986; Kohn et al., 1992; Andriessen et al., 1993; O’Sullivan et al., 2001)

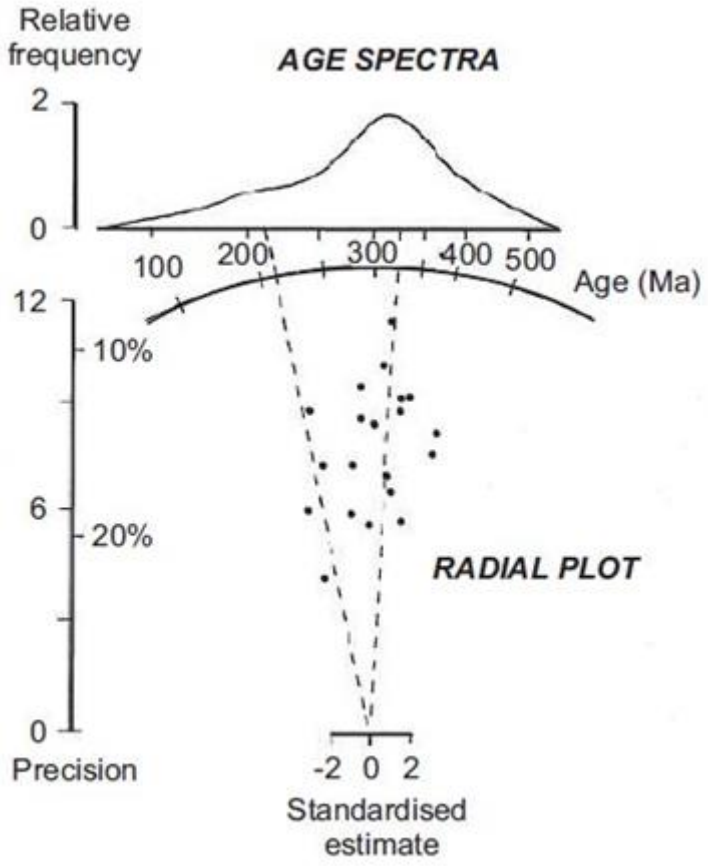

Fig. 2.7 The age spectra (top) and radial plot (bottom) of twenty apatite grains from a sample artificially composed of two age groups (i.e., ~240 and ~340 Ma) (Galbraith and Green, 1990; Wagner and Van den haute, 1992; O’Sullivan et al., 2005). The two dashed lines show the component age estimates. In the radial plot, the horizontal and vertical axes represent the standardized age estimate and reciprocal error, respectively.

2.2.2 Apatite fission track modelling

2.2.2.1 Retention and annealing of FT

Accumulation of the radiogenic daughter product below a certain temperature range is the concept of closure temperature. Above closure temperature, the system is open and radiogenic products are lost (after Dodson, 1973). Such closure is not instantaneous, and there is a transitional temperature range, the partial stability zone,

in which daughter products are partially lost. In fact, fission tracks are unstable and will tend to be repaired by solid-state diffusion processes ("annealing"). Annealing is essentially a function of time and temperature although other mechanisms have been considered. The setting of time and temperature boundaries for partial track stability (usually now referred to as the Partial Annealing Zone) shows the onset of a numerical description of the annealing process. Within the Partial Annealing Zone, measured FT ages could be explained in terms of a sample's thermal history (Fig. 2.8a).

As a result of annealing, the etchable length of the individual tracks, which is initially similar for all newly formed tracks in a given mineral structure (16 μm for apatite), is progressively shortened (Green et al., 1986). On geological time-scales, at temperatures >110 ± 10 °C fission tracks anneal completely in apatite (Wagner, 1968; Naeser, 1979; Gleadow and Duddy, 1981; Gleadow et al., 1986; Green et al., 1986). Annealing of fission tracks occurs at decreasing rates over geological time in the temperature range of 110-60 °C, known as the apatite partial annealing zone (APAZ) (Fig. 2.8) (Gleadow and Duddy, 1981; Naeser, 1981). Below 60 °C, annealing rates are very low and the tracks are generally considered stable. Annealing behaviour can be related to the etching characteristics of the host apatite through the measurable Dpar parameter, which is the c-axis parallel etch pit diameter intersecting a polished and etched apatite surface (Donelick, 1993; Burtner et al., 1994; Carlson et al., 1999; Ketcham et al., 1999; Barbarand et al., 2003b).

The effects of annealing can be quantified by measuring the lengths of horizontal confined tracks (Gleadow et al., 1986). This depends on the fact that tracks form continuously, and thus each track experiences a different portion of the integrated thermal history (Braun et al., 2006). Thus, the track lengths distribution, obtained by measuring a sufficient number of horizontal confined tracks (preferably ≥100), contains information on the thermal history experienced by the sample (Braun et al., 2006; Fig. 2.8b).

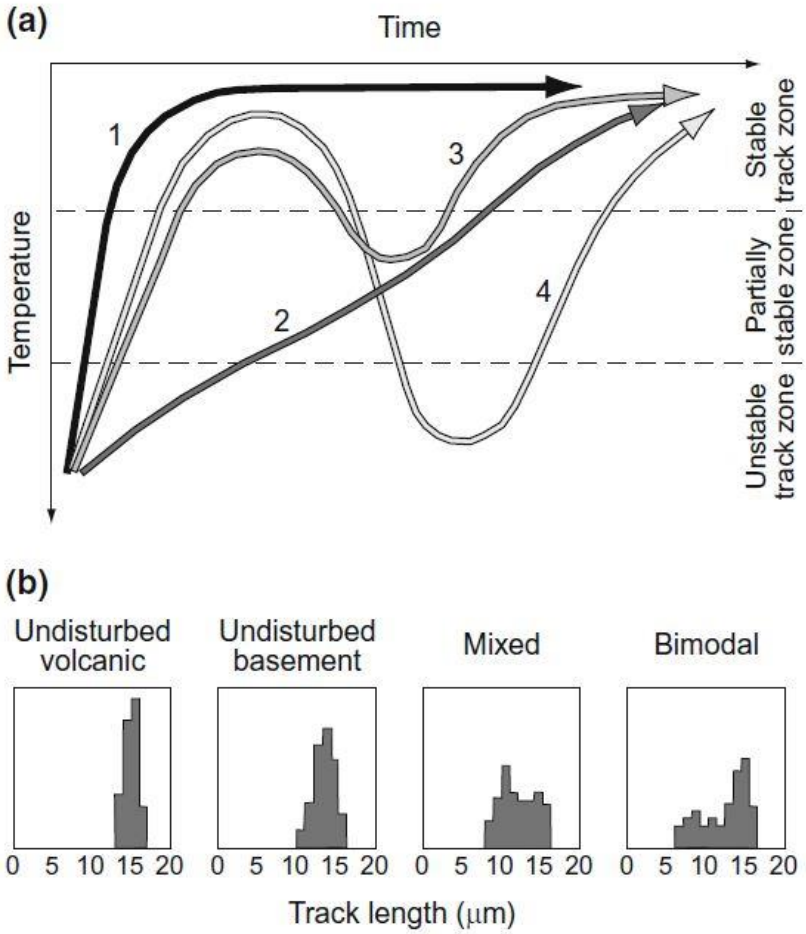

Fig. 2.8 a. Schematic cooling curves for rock and mineral systems considered in terms of fission-track accumulation (Wagner, 1972; Fitzgerald and Malusà, 2018). Curve 1 rapid cooling (e.g. Fish Canyon Tuff): all tracks are stable and measured age approximates to formation age. Curve 2 slow cooling (e.g. an Alpine gneiss): stability reached time after formation; tracks formed during residence in partial stability (or partial annealing) zone are partially annealed. Curves 1 and 2 only consider differences in initial accumulation of tracks. Curves 3 and 4 show reheating of already cooled samples. Curve 3 gives a mixed age: earlier-formed tracks partially annealed to a level dependent upon time and temperature experienced in partial stability zone; second family of tracks are stored on re-entry into stability zone. Intrusion of a dyke into granite could cause such partial resetting in granite samples near the contact. Curve 4 indicates a reset age: initial cooling into stability field is followed by reheating back into unstable zone. FT age would relate only to the time of re-emergence into the track stability zone. b Comparison of horizontal confined track-length distributions in apatite (after Gleadow et al., 1986). Undisturbed volcanic distributions characterise rapid cooling (Curve 1) with a dominance of long lengths, a narrow distribution and a mean track length ~14 μm. Undisturbed basement distributions are broader, with mean track lengths ~12-13 μm and would be found in samples following cooling curve 2. Partially reset samples (cooling curve 3) will also

show a broad track-length mixed distribution, sometimes resolving into bimodality. Total annealing (cooling curve 4) may show volcanic or basement-type distributions depending on the rate of cooling in the stability zone (Fitzgerald and Malusà, 2018).

2.2.2.2 Thermal modelling

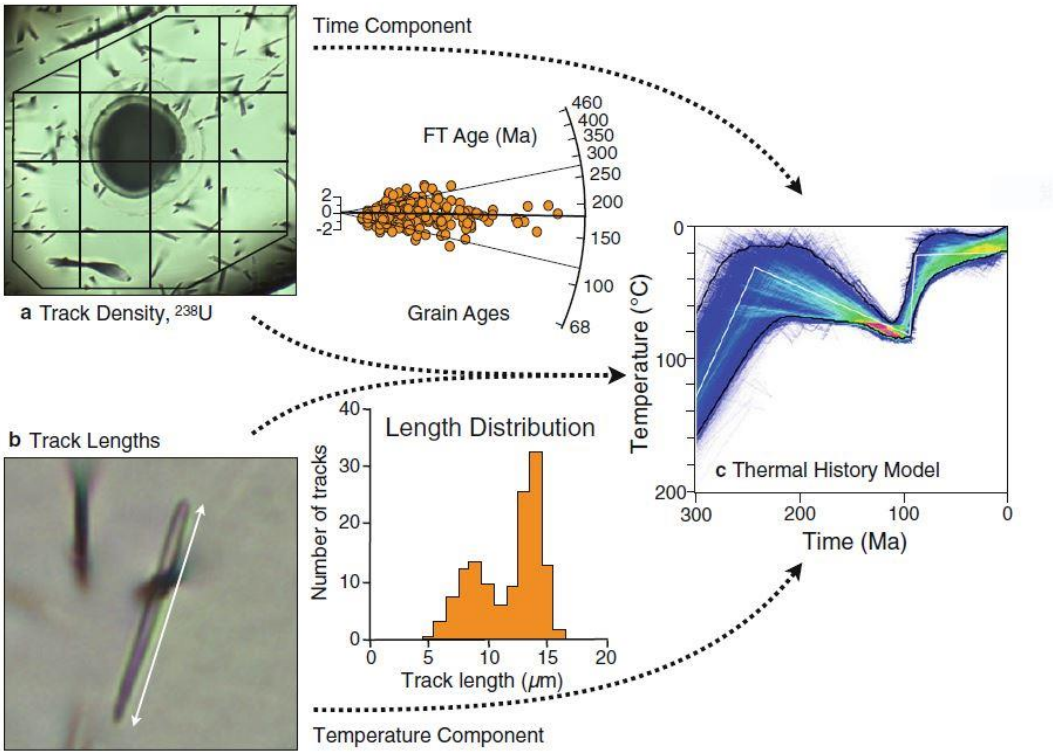

Fig. 2.9 Analytical sequence required for the reconstruction of thermal histories from primary measurements of a, the number, and b, the lengths of fission tracks in a mineral sample, together with the ^{238}U concentration, here indicated by a circular laser ablation pit in (a). Image an includes a region of interest outlining the area to be counted and an internal grid to assist in counting. Image b shows a confined fission track and its measured length. In the center, a radial plot shows the distribution all of grain ages, and a histogram the distribution of all lengths measured in a sample. These results can be thought of as primarily reflecting the time component, and the temperature component of the underlying thermal history, respectively. The thermal history reconstructed from such data is shown in the temperature-time plot, c, on the right. In practice, this FT analytical sequence is currently fully developed only for apatite and is the basis of the conventional approach described here (Fitzgerald and Malusà, 2018).

The EDM has become central to what we may now describe as conventional FT analysis, a combination of procedures that has progressively become the standard, and almost universally adopted, approach to FT dating in laboratories around the world. In this approach, FT ages are determined by the EDM using the empirical 'zeta' calibration against a set of independent age standards (Fleischer and Hart, 1972; Hurford and Green, 1983), combined with measurements of horizontal confined track lengths (Gleadow et al., 1986) usually measured using a microscope drawing tube and digitising tablet. In essence, these two complementary data sets comprising the FT grain-age distribution and the FT length distribution, contain, respectively, the time information and the temperature information that are required by forward modelling schemes to reconstruct the thermal history of a particular sample (Fig. 2.9). This approach has been widely applied to the common uranium-bearing accessory minerals apatite, titanite and zircon, of which apatite has been by far the most important, because of its common occurrence, its simple and consistent etching behaviour and its well-documented annealing properties relative to other minerals.

2.2.3 Multidimensional Scaling (MDS) method

Multidimensional Scaling (MDS) method has been proved to be an easy and efficient statistical technique for comparison of complex detrital geochronological dataset (Vermeesch, 2013). Actually, it is a dimension-reducing exploratory data analysis tool, but can capture the main features of detrital datasets. It is a robust and flexible superset of the Principal Component Analysis (PCA) which makes fewer assumptions about the data and produces a 'map' of points on which 'similar' samples cluster closely together, and 'dissimilar' samples plot far apart (Vermeesch, 2013). In this work, the MDS user-friendly interface provided by the website http://mudisc.london-geochron.com has been used.

2.2.3.1 Measuring the dissimilarity between two samples

Kolmogorov–Smirnov (KS) test is useful for comparing detrital age distributions because it makes no assumptions about how the data are distributed and is thus sensitive to both the position of age peaks and the shape of the overall probability

curve (Berry et al., 2001; DeGraaf-Surpless et al., 2003). Depending upon the combined sample size, the KS statistic corresponds to a probability value (P) representing the probability that differences between the two distributions are not more than would be expected based on random chance (Amidon et al., 2005).

$$KS = \max_t \left| F_i(t) - F_j(t) \right|$$

where |·| stands for the absolute value and F(t) is the empirical cumulative distribution function:

$$F(t) = (\text{number of ages less than t})/\text{N}.$$

The KS statistic is most sensitive to the region near the modes of the sample distributions, and less sensitive to their tails. Therefore, we just use the KS effect size as a dissimilarity measure.

2.2.3.2 Multidimensional scaling

Let δ be a matrix of pairwise dissimilarities between n samples:

$$\delta = \begin{pmatrix} \delta_{1,1} & \delta_{1,2} & \cdots & \delta_{1,n} \\ \delta_{2,1} & \delta_{2,2} & \cdots & \delta_{2,n} \\ \vdots & \vdots & \delta_{i,j} & \vdots \\ \delta_{n,1} & \delta_{n,2} & \cdots & \delta_{n,n} \end{pmatrix}$$

where $\delta_{i,j}$ is the dissimilarity between samples i and j. Let $f(\delta_{i,j})$ be a monotonically increasing function transforming the dis-similarities into 'disparities'. Then MDS produces an R-dimensional (where $R \leq n$) configuration of points $x=\{x_1,x_2,\ldots,x_i,\ldots,x_j,\ldots,x_n\}$ with $x_i=(x_{i1},x_{i\,2},\ldots,x_{i\,R})$ and $x_j=(x_{j\,1},x_{j\,2},\ldots,x_{j\,R})$ for $1 \leq i, j \leq n$. The Euclidean distance between any two points x_i and x_j in this configuration approximates the disparities between samples i and j:

$$d_{i,j} \approx f\left(\delta_{i,j}\right)$$

$$d_{i,j} = \sqrt{\left(x_i^1 - x_j^1\right)^2 + \left(x_i^2 - x_j^2\right)^2 + \ldots + \left(x_i^R - x_j^R\right)^2}.$$

we only consider the case where R=2, so that the configuration x can be plotted on a sheet of paper, like a map. Therefore, we will use the terms ‘configuration’ and ‘map’ interchangeably.

A graphical user interface has been created that implements MDS in a user-friendly way and can be downloaded from http://mudisc.london-geochron.com along with further details about the R code, input files and so forth (Vermeesch, 2013).

Chapter 3

This Chapter contains the first part work of the PhD period, is mainly about the study of ice flow pathways in the western Ross Sea Coastline over the last 5 Ma through the analysis of the stratigraphic record of CIROS-2. In this part of work, we focus on recovering the derivations of the sediments in the CIROS-2 by detrital apatite fission-track and then defining the ice flow lines. At the end, we identified the ice pathways during the early Pliocene and late Pleistocene. In the following chapter, the version of the manuscript published on Terra Nova is presented.

A detrital apatite fission-track study of the CIROS-2 sedimentary record: tracing ice pathways in the Ross Sea area over the last 5 million years

Xia Li[1]*, Massimiliano Zattin[1], Valerio Olivetti[1]

[1] – *Department of Geosciences, University of Padova, via G. Gradenigo 6, 35131 Padova (Italy)*

** corresponding author: xia.li@studenti.unipd.it, tel: ++39 049 8279186, fax: ++39 049 8279122*

RUNNING HEAD TITLE: DETRITAL THERMOCHRONOLOGY CIROS-2

DOI: 10.1111/ter.12396

ABSTRACT

The Ross Sea is a crucial area to investigate pathways of ice during the Cenozoic as it records the evolution of both the East and West Antarctic Ice Sheets. This work is based on detrital apatite fission track (AFT) data extracted from the sedimentary record of well CIROS-2, which spans through the last 5 million years. The AFT data show a large range of ages and most of the grains fit well with two main components that fall between 24-42 Ma and 43-70 Ma whereas the other components are not regularly distributed through the well, thus indicating a mixture of provenance from different areas along the Transantarctic Mountains (TAM). As a whole, our work suggests glacial expansion over the McMurdo Sound during the Pliocene, and periodically ice invading and retreating in Pleistocene.

3.1 Introduction

The Ross Sea is a crucial area to investigate the history of Antarctic ice during the Cenozoic as it records the evolution of both the East and West Antarctic Ice Sheets, whose variations are a direct response to climate change. In recent years, samples from offshore drilling projects have been investigated with different geochronological and thermochronological techniques (Hambrey et al., 2002; Barrett et al., 2009; Zattin et al., 2012; Olivetti et al., 2015; Talalay and Pyneb, 2017). These drillholes, mostly located in McMurdo Sound, provide information on the ice flows in the area of the western Ross Sea. The stratigraphy of the cores drilled during the Cape Roberts Project with a nearly continuous marine sedimentary record from early Oligocene to early Miocene suggests the presence of a West Antarctic Ice Sheet in the western Ross Sea since the Oligocene (Olivetti et al., 2013, 2015). The two drillholes of the Antarctic Geological Drill project (ANDRILL) investigated the last ca. 20 Myr, showing an ice pattern dominated by south to north trending flow lines parallel to the Transantarctic Mountains (TAM) front during the Miocene (McKay et al., 2009; Zattin et al., 2010, 2012; Cornamusini and Talarico, 2016). The drillholes CIROS-1 and MSSTS-1 recovered a late Eocene to early Miocene (ca. 34 Ma to ca. 5 Ma)

sedimentary record whose detritus was supplied mainly from the Dry Valleys Block of the TAM (Hall and Buhmann, 1989; Ehrmann, 1998; Roberts et al., 2003; Sandroni and Talarico, 2004). The common view of these works is that the West Antarctica Ice Sheet was the main contributor of ice in the western Ross Sea, although outlet glaciers from the East Antarctic Ice Sheet also made a contribution since the Oligocene.

In this paper, we focus on defining the pathways of ice spanning the last 5 Ma through the analysis of the stratigraphic record of CIROS-2. We focus on sediments span the lower Pliocene to Quaternary. The heavy mineral record (Ehrmann and Polozek, 1999) indicates that during the Pliocene, the ice discharged through the TAM into McMurdo Sound. The source area shifted in the Quaternary to the south, to the region of the present-day Ross Ice Shelf. A similar view is derived from lithologies of clasts which show that during the Pliocene sediments of CIROS-2 originated both from the Ferrar Glacier flowing through the TAM, as it does today, and the southern Mount Morning - Discovery Peninsula (Sandroni and Talarico, 2006). From the Pleistocene to present-day, the provenance shifted from the Blue Glacier area to the north along the coast and then into Ferrar Fjord from the east (Kyle, 1990; Sandroni and Talarico, 2006). Despite previous detailed work, there remains debate about the shifting of ice source areas, especially during the Plio-Pleistocene, when global climate changed from temperatures that were warmer than today (Naish et al. 2009). In particular, the contribution of eastward flowing ice form EAIS through the TAM is unclear. In this work, we provide new detrital apatite fission track (AFT) data on 16 samples from CIROS-2 that range in age from the early Pliocene to Pleistocene for obtaining new constraints on the pathways of ice over this interval.

3.2 Geological setting

The CIROS-2 drillhole was drilled in 1984 in the sea-ice platform off the Victoria Land Coast on the western shelf of McMurdo Sound (77°41’S; 163°32’E) (Fig. 3.1). It is located only 1.2 km east of the floating tongue of the present-day Ferrar Glacier, which flows from the polar plateau through the TAM and drains the East Antarctic Ice Sheet into a fjord (Barrett and Hambrey, 1992; Ehrmann and Polozek, 1999; Sandroni and Talarico, 2006).

The on-shore region west of McMurdo Sound consists of the southern Victoria Land

sector of the TAM, composed of a late Precambrian to early Paleozoic crystalline basement, which mainly occupies the coastal area, and an overlying sedimentary cover complex, restricted to the inner part of the on-shore region (ca. 25-40 km from the coast) (Gunn, 1962; Gunn and Warren, 1962; Sandroni and Talarico, 2006). The basement complex consists of late Precambrian to early Palaeozoic amphibolite-facies metamorphic rocks (Koettlitz Group) intruded by granitoid plutons of the Granite Harbour Intrusive Complex (Grindley and Warren, 1964) that includes a heterogeneous series of orthogneisses and plutons ranging in age from possibly Late Proterozoic to Early Ordovician (Allibone et al., 1993a, b). Emplacement of granitoid rocks was followed by uplift and erosion, with the development of the extensive Kukri Peneplain, overlain by sandstones, conglomerates, siltstones and minor coal beds of the Devonian to Triassic Beacon Supergroup rocks (Harrington, 1965). In Jurassic time, both the basement complex and Beacon Supergroup were intruded by dolerite sills and dykes of the Ferrar Supergroup, accompanied by an extrusive phase not present within the Dry Valley region (Kyle, 1981).

Geology of the southern and eastern parts of the McMurdo Sound is characterized by the presence of the Cenozoic alkalic McMurdo Volcanic Province (Cole and Ewart, 1968; Kyle, 1981, 1990; LeMasurier and Thomson, 1990; Ehrmann and Polozek, 1999; Fig. 1). Volcanic activity occurred during two main phases: the first (ca. 19 to ca. 10 Ma) characterized by trachytic rocks, and the second (last ca. 10 Ma), more voluminous, comprising basanitic to phonolitic sequences.

CIROS-2 was drilled down to 166.7 m below the sea floor and can be divided into two main sequences (Fig. 3.2): a Pliocene lower sequence (from 167.7 to about 114 mbsf), dominated by diamictites, and a Pleistocene upper sequence, consisting of an alternation of sandstones and diamictites (Sandroni and Talarico, 2006). The lower sequence is characterized by the presence of clasts dominated by monzogranites/granodiorites (Granite Harbour Intrusive Complex) and vesicular basalts (McMurdo Volcanic Group), with minor occurrences of gabbros/dolerites (Ferrar Supergroup), sandstones (Beacon Supergroup) and metamorphic rocks (Koettlitz Group). The upper sequence is dominated by tonalites, with very minor occurrences of gabbros/dolerites, strongly altered basalts and metamorphic rocks.

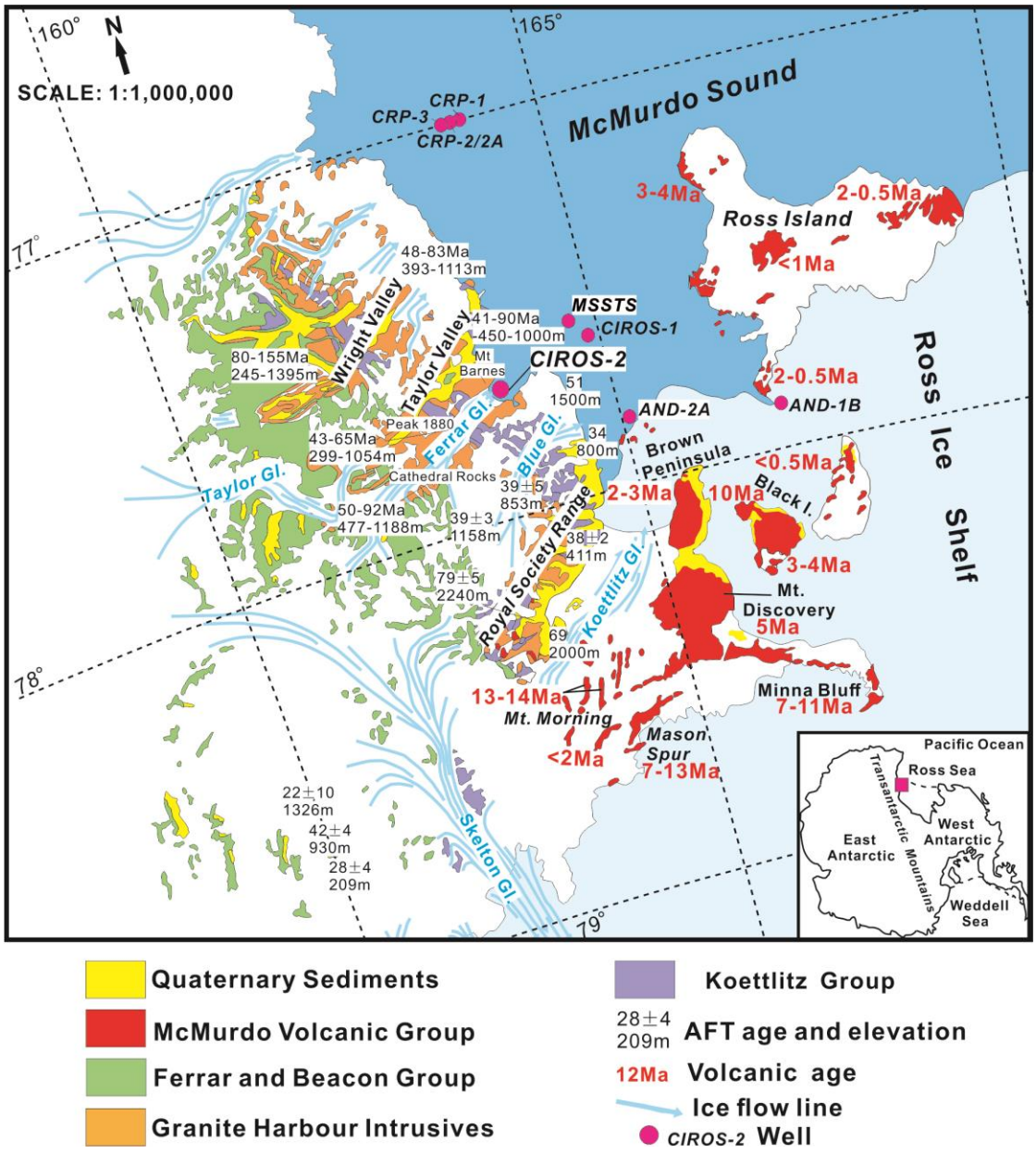

Fig. 3.1 Geological map of the southwest corner of the Ross Sea (modified from Warren, 1969; Kyle, 1990; Sandroni and Talarico, 2006). AFT ages are cited from Gleadow and Fitzgerald, 1987; Fitzgerald, 1992, 2002; Fitzgerald et al. 2006; Zattin et al., 2014 and Olivetti et al., 2018.

3.3 Material and Results

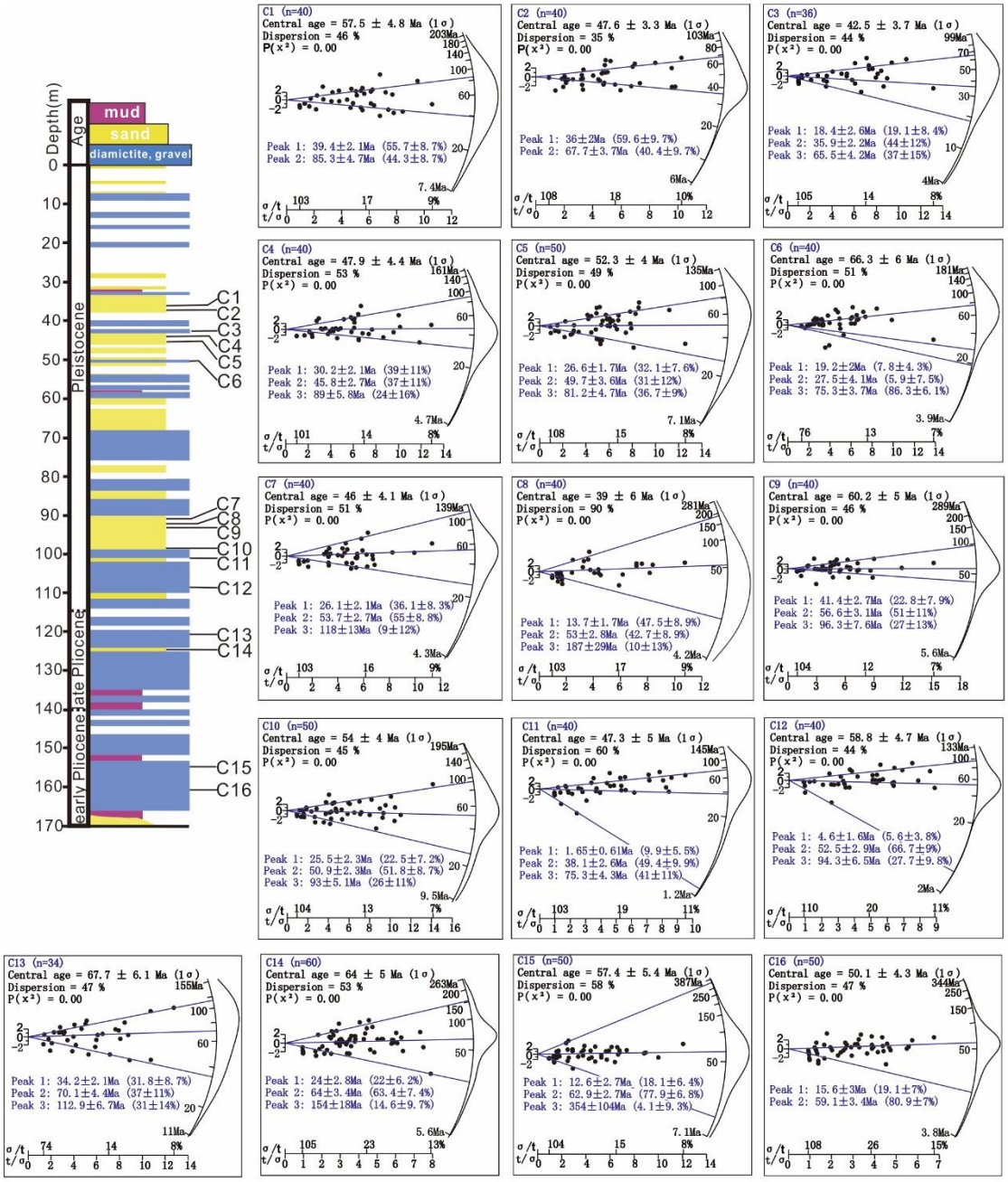

Fig. 3.2 Samples distribution along the sedimentary sequence of CIROS-2 (modified from Sandroni and Talarico, 2006) and abanico plots (Dietze et al., 2016) of analyzed data.

Apatite grains were separated from cores and then processed for fission-track analysis through standard processing techniques. AFT single grain ages were calculated using the external-detector and the zeta-calibration methods (Hurford and Green, 1983) with IUGS age standards (Durango and Fish Canyon apatites; Hurford, 1990) and a value of 0.5 for the $4\pi/2\pi$ geometry correction factor. The analyses were subjected to the $\chi 2$ test (Galbraith, 1981) to detect whether the data sets contained any extra-Poissonian

error. A $\chi 2$ probability of less than 5% denotes a significant spread of single grain dates. After using standard analytical procedures, grain-age distributions were decomposed into different components and plotted as combined radial and kernel density plots (Dietze et al., 2016) using the density plotter software of Vermeesch (2012), (Fig. 3.2).

As a whole, the AFT data show a large range of single grain ages and no samples vary within the range predicted by Poissonian statistics that would equate to a single age distibution (Table 3.1, Fig. 3.2). Most of the grains fall within two age groups between 24-42 Ma (here called P2 for simplicity) and 43-70 Ma (P3). The youngest grain ages (P1 < 20 Ma) show a large age range and in general are represented by a lower number of grains. Other age groups are represented by AFT age component 70-100 Ma P4 that from 124 m bsl depth, and in a few cases (C8, C13, C14), much older grains are present (P5).

3.4 Discussion

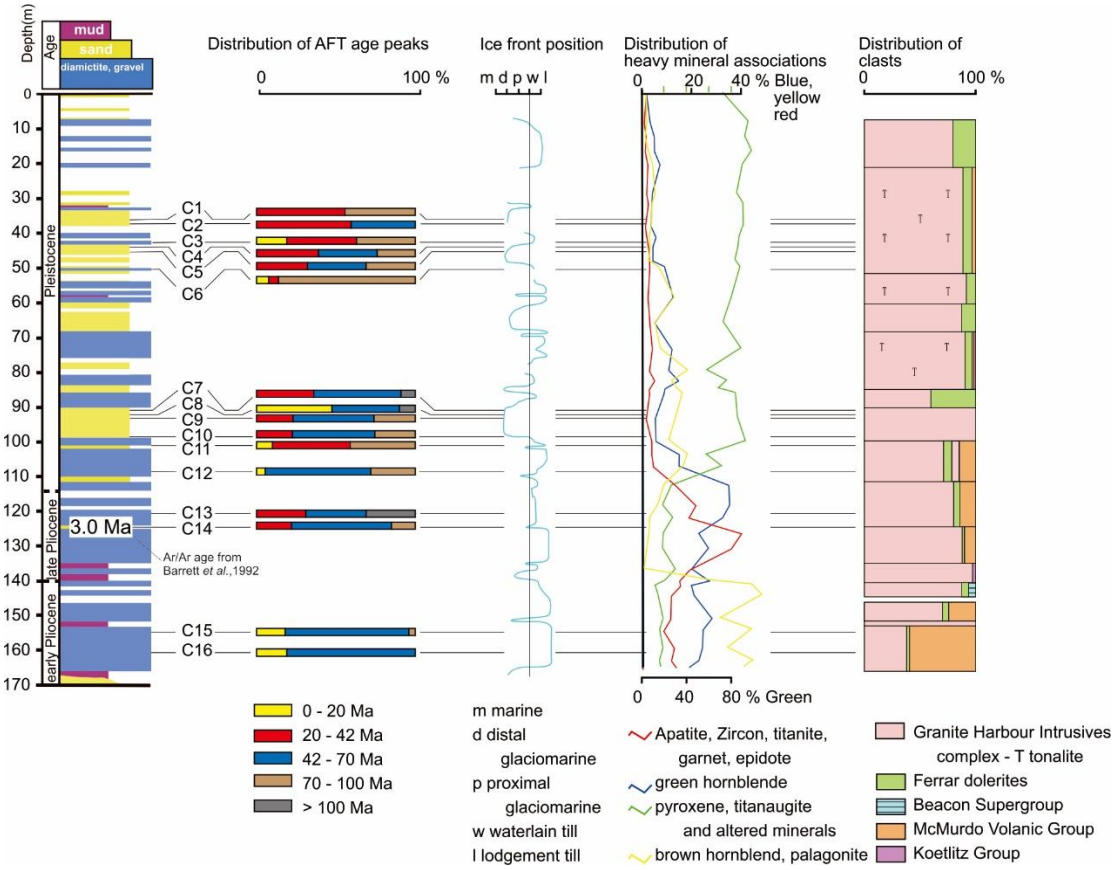

Fig. 3.3 Distribution of AFT age components (this work), ice front position (from Barrett and Hambrey, 1992), heavy mineral distribution (Ehrmann and Polozek, 1999) and clast lithologies (Sandroni and Talarico, 2006).

The distribution of AFT age populations in CIROS-2 show that apatites were derived from sources with different bedrock histories, some of which can be a diagnostic signal for the sediment provenance.

In order to investigate the sediment source and the consequent glacial flow pattern Figure 3.3 compares the AFT age population distribution from this study with results from published heavy mineral and clast analysis (Ehrmann and Polozek, 1999; Sandroni and Talarico, 2006).

The youngest AFT ages (P1, <20 Ma) matches the age of the widespread volcanic event in the western Ross Sea, whose presence has been already identified in CIROS-2 (Ehrmann and Polozek, 1999; Sandroni and Talarico, 2006) and in other drillholes such as ANDRILL (Talarico et al., 2010; Zattin et al., 2012). The possible volcanic sources are Cenozoic alkalic McMurdo Volcanic Province, including Mount Morning (13-14 Ma) - Mount Discovery (about 5 Ma), Brown Peninsula (2-3 Ma), Black Island (3-4 Ma) and Ross Island (0.5-4 Ma). The oldest centers of the McMurdo Volcanic Province are today situated around the base of Mount Morning (Fig. 3.1) such as Gandalf Ridge (18.7-15.5 Ma), Riviera Ridge (15.2-13.0 Ma), and Mason Spur (13.5-12.4 Ma) (Kyle, 1981, 1990).

Youngest grains from samples at the bottom of CIROS-2 (C16 and C15) are consistent with the abundance of volcanic clasts and the high quantity of brown hornblende and palagonite (yellow curve in Fig. 3.3), considered to be derived from McMurdo volcanic rocks. It is noteworthy that the massive diamictites with slickensides at the bottom of CIROS-2 have been interpreted as lodgment till. Together, this evidence suggests an expansion of glaciers flowing from the south to the north that occupied the Ferrar fjord at that time (late Pliocene) (Fig. 3.4A).

Grain ages between ca. 13 and 18 Ma are likely to be volcanic in origin and are present mainly in the early Pliocene samples (C15 and C16), but are less abundant or nearly absent since the boundary of late Pliocene and early Pliocene. Their presence is significant only in Pleistocene samples C3 and C8. Two main reasons could have controlled this pattern: (i) the burial of older volcanic rocks under the younger volcanic edifices protecting the older rocks from later erosion and (ii) a change in

topography. Prior to about 5 Ma ago, Minna Bluff, Ross Island, and White Island had not formed and most part of Mount Morning was also probably absent (Kyle, 1981) (Fig. 3.4A). Growth of the Mount Morning - Discovery volcanic province might have acted as barrier cutting off sediment transfer from the south (e.g. Mason Spur) as proposed by some authors (Kyle, 1981,1990; Ehrmann and Polozek, 1999; Sandroni and Talarico, 2006).

It is notable that although most of the exposed volcanic rocks are relatively young (i.e. <10 Ma), there are very few AFT grains with similar ages. The likely reason is related to lithology, as these rocks are mainly basaltic and devoid of apatites (where present, apatite usually has a very low U content).

Sample C14 (125 m bsl) shows the first occurrence of P2 population represented by 24 Ma that ages are not found in exposed bedrock in the immediate source area of the CIROS-2 location. A volcanic origin might be possible for ages between 20-30 Ma given that some volcanic apatites with a U-Pb age of about 30 Ma have been detected in AND-2A (Zattin et al., 2012) although the location of volcanic source unknown. However, these apatites could derive also from exhumed basement rocks because similar ages have been found in the Skelton Glacier. (Zattin et al., 2014; Olivetti et al., 2018).

Most of the populations in P2 have ages between 30 and 40 Ma and are related to apatites derived from erosion of exhumed bedrock exposed along the TAM front as they match exhumation phases described in literatures (Fitzgerald, 2002; Zattin et al., 2014; Olivetti et al., 2015; 2018). Such AFT ages are rare in the Dry Valley (Gleadow and Fitzgerald, 1987; Fitzgerald et al., 2006) but they have been detected in the Royal Society Range (Olivetti et al., 2018) and are also abundant to the south, between the Skelton and Byrd Glaciers (Huerta et al., 2011; Zattin et al., 2014) as well as much further (600km) to the south (Stump and Fitzgerald, 1992; Fitzgerald, 1994; Fitzgerald and Stump 1997; Miller et al., 2010) (Fig. 3.4).

Fitzgerald et al. (2006) and Fitzgerald (2002) dated samples on both sides of the Ferrar Glacier: 43.3Ma at 299 m in the Kukri Hills (Peak 1880), 50.3 Ma at 477 m in Cathedral Rocks, ~42 Ma at ~0 m and ~41 Ma at ~ -450 m in Mt Barnes. Given these age-elevation relationships, bedrock AFT ages < ~40 Ma should be present in ice-covered area at around 500 m below sea level, corresponding to the maximum depths of the Ferrar glacial trough. However, the portion of the Ferrar Glacier bed, with a depth of 500m beneath sea level is very limited.

The first occurrence of P2 grain ages in our samples overlaps minerals representative of intrusive and metamorphic rocks, and correspond also to an increase in clasts diagnostic of the Granite Harbour Intrusive complex suggesting a shift in the source area.

In all, the most P2 grains probably was derived from the northern Royal Society Range because of the abundant similar AFT ages (20-40Ma) detected in this area and the proximity of the location of CIROS-2; besides, minor part also could be derived from the lower portion of Ferrar Glacier although the portion of the area 500m below the sea level is very limited.

The ages of P3 are well represented in the Dry Valley region and from the higher elevation areas along the TAM front (Gleadow and Fitzgerald, 1987; Fitzgerald et al., 2006). On the whole, P3 is always the most abundant population, suggesting that local erosion is the main source for the sediments.

The two oldest populations match bedrock ages found in the inland of Dry Valleys (Gleadow and Fitzgerald, 1987). Considering the high elevations present in the Ferrar Glacier catchment (up to >3500m at Mt Feather for example) it is possible that grains with ages older than 70 Ma derive from a local or inland source and, thus, were transported eastward by outlet glaciers.

Sediments above 100 m bsf have been interpreted as result of a variety of environments shifting between open sea, glaciolacustrine and glacial proximal (Barret and Hambrey, 1992). The occurrence of young, volcanic P1 within massive diamictite at 50 m and 42 m bsf suggests a possible glacial transport from south to north and two glacial expansion events of the southern glacier into McMurdo Sound (Fig. 3.4B).

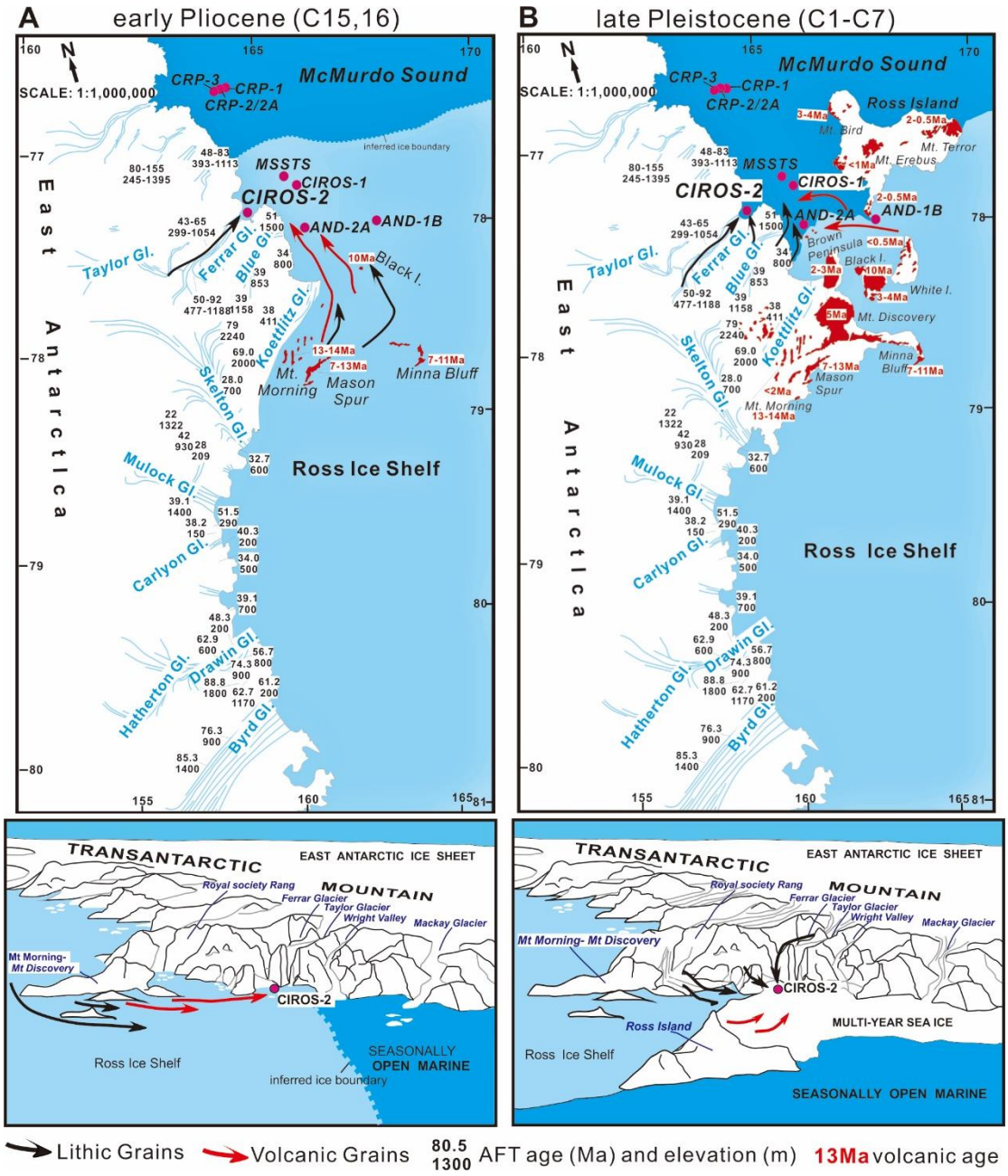

Fig. 3.4 Sediment dispersal patterns during the deposition of massive diamictites in the early Pliocene (a) and late Pleistocene (b) in the western Ross Sea (modified according to Warren, 1969; Levy et al., 2012; Kyle, 1981). AFT ages are cited from Gleadow and Fitzgerald, 1987; Fitzgerald, 1992, 2002; Fitzgerald et al. 2006; Zattin et al., 2014 and Olivetti et al., 2018.

3.5 Conclusions

This work, based on AFT detrital data from the CIROS-2 sedimentary record,

provides new information about ice flow in the Ross Sea area during the last 5 Ma.

(1) Two samples from an early Pliocene diamictite, include a volcanic component from the oldest McMurdo eruption centers, suggesting expansion of glaciers over the ice-free McMurdo Sound in early Pliocene, as showed in Fig. 3.4A, similar to the periodic advances of ice into the Ferrar Glacier region during the Pleistocene (Fig. 3.4B) (e.g. between ~ 23,840 14C yr BP to~ 8340 14C yr BP, Hall and Denton, 2000; Staiger et al., 2006).

(2) Two samples from the late Pliocene suggest a glacial expansion with a local source of sediments, probably associated with an advance of the Ferrar Glacier.

(3) Since the early Pleistocene AFT data record a dominantly local provenance (i.e. from the Ferrar and outlet glaciers) with an irregular mix of ages, due to ice periodic invading and retreating across McMurdo Sound.

(4) Two samples with volcanic apatites are best explained by distinct episodes of ice expansion from the south across McMurdo Sound.

		Sample	Depth(m)	*No. of crystal*	ρ s	Ns	ρ *i*	*Ni*	*P(χ)2*	ρ d	*Nd*	*Central age(Ma)±1* σ	P1(%)	P2(%)	P3(%)	P4(%)	P5(%)	P6(%)
Pleistocene	Unit 2.2	CIR1	37.46-37.56	40	7.09	1436	30.73	6217	0	13.8	6943	57.5±5.2			39.3±2.15 (54.9%)	80.5±4.7 (40.5%)	145.1±22.8 (4.6%)	
		CIR2	37.75-37.81	40	7.68	1349	37.28	6544	0	13.6	6864	47.6±3.6	6.3±5.4 (2.7%)		36.6±2.1 (56.8%)	67.7±3.8 (40.5%)		
		CIR3	42.08-42.17	36	8.05	1567	41.98	8171	0	13.4	6746	42.5±3.9	6.1±5.55 (8.7%)		32.5±1.85 (49.4%)	63.5±3.45 (41.9%)		
		CIR4	43.75-43.82	40	8.56	1819	43.38	9218	0	13.3	6707	47.9±4.6	10.1±5.4 (7.3%)		38.2±1.75 (67.4%)		87.7±5.45 (25.3%)	
		CIR5	44.30-44.35	50	8.03	2162	37.1	9982	0	13.2	6628	52.3±4.3		22.7±1.75 (24.9%)	38.4±2.9 (21.6%)	65.8±4.75 (38.7%)	99.4±9.9 (14.8%)	
		CIR6	50.07-50.17	40	8.97	1461	41.12	6698	0	12.9	6510	66.3±6.4	4.9±0.95 (5.1%)		30.9±2.25 (11.2%)	64.1±3.8 (58.8%)	114.6±9.95 (24.9%)	
		CIR7	90.85-91.00	40	6.14	1330	28.43	6156	0	12.7	6392	46±4.4	6.7±3.2 (8.7%)	28.2±2.5 (27.8%)		53.7±2.8 (54.6%)	118.3±13.35 (8.8%)	
		CIR8	91.66-91.86	40	4.34	868	20.66	4130	0	12.5	6313	39±6.1	13.7±1.75 (47.5%)			53.0±2.9 (42.7%)		186.9±29.05 (9.8%)
		CIR9	92.80-92.97	40	9.72	1777	36.65	6701	0	12.4	6235	60.2±5.4	5.7±1.75 (5.7%)			52.5±2.45 (64.5%)	91.9±6.75 (67.5%)	287.4±109.95 (2.4%)
		CIR10	98.62-98.70	50	11.25	2420	42.37	9114	0	12.2	6156	54±4.4		25.5±2.3 (22.4%)		50.8±2.45 (51.6%)	90.8±5.45 (24.1%)	191.2±52.6 (1.9%)
		CIR11	100.75-100.92	40	7.64	1221	36.23	5787	0	12.1	6077	47.3±5.2	1.6±0.55 (9.8%)		37.6±2.7 (47.6%)	67.5±5.55 (27.6%)	95.0±9.8 (15.0%)	
		CIR12	109.75-109.85	40	9.68	1275	33.63	4428	0	11.9	5998	58.8±5.1	4.6±1.7 (5.6%)			52.4±2.9 (66.5%)	94.2±6.5 (27.9%)	
	Unit2.2	CIR13	120.88-120.96	34	12.27	1736	38.39	5428	0	11.7	5920	67.7±6.5			34.2±2.15 (31.7%)	70.0±4.45 (36.6%)	112.8±6.8 (31.6%)	
		CIR14	124.33-124.40	60	6.09	1354	20.93	4649	0	11.7	5880	64±5.4		23.6±2.75 (21.4%)		63.7±3.4 (63.8%)	153.7±17.6 (14.7%)	
Early Plioc.	**Unit 1.1**	CIR15	156.37-156.46	50	6.97	1535	23.28	5127	0	11.6	5841	57.4±5.7	12.5±2.7 (18.1%)			62.8±2.85 (77.9%)		354.1±102.6 (4.1%)
		CIR16	160.70-160.97	50	4.4	686	17.13	2669	0	11.4	5762	50.1±4.6	15.5±3.0 (19.1%)			58.5±3.4 (79.2%)		331.2±236.75 (1.7%)

Table 3.1 Apatite fission track data of CIROS-2. Central ages calculated using glass dosimeter CN5 and ξ-CN5 = 344.09 ± 10.36 (analyst XL). ρs: spontaneous track densities (10 5cm-2) measured in internal mineral surfaces; Ns: total number of spontaneous tracks; ρi and ρd: induced and dosimeter track densities (106 cm-2) on external mica detectors (g= 0.5); Ni and Nd : total numbers of tracks; P(χ)2: probability of obtaining χ2-value for v degrees of freedom (where v= number of crystals-1); a probability >5% is indicative of a homogenous population. Samples with a probability <5% have undergone mixture modeling using the algorithm of Galbraith and Green (1990)

Chapter 4

This Chapter includes the second part work during the PhD period. The main content is about the defining the signatures of apatite fission-track for the Ross Sea ice flows during the Last Glacial Maximum, which is based on the apatite fission track dating and modelling, and MDS analysis of the samples from piston cores across the Ross Sea. At the end, we build an ice flow lines model of the Ross Sea based on detrital provenance analysis of glacial sediments. In the following chapter, the version of the manuscript has already submitted to Geochemistry, Geophysics, Geosystems.

Apatite fission-track signatures of the Ross Sea ice flows during the Last Glacial Maximum

Xia Li[1]*, Massimiliano Zattin[1], Valerio Olivetti[1]

[1] – *Department of Geosciences, University of Padova, via G. Gradenigo 6, 35131 Padova (Italy)*

** corresponding author: xia.li@studenti.unipd.it, tel: ++39 049 8279186, fax: ++39 049 8279122*

RUNNING HEAD TITLE: DETRITAL THERMOCHRONOLOGY, ROSS SEA, LGM

ABSTRACT:

The Ross Sea received one third of Antarctic ice both from West Antarctica and East Antarctica. Ice dynamics of it are the direct response to climate change which make it to be a crucial investigating area. Our work based on samples from 18 piston cores

across the Ross Sea with post-LGM (Last Glacial Maximum) age. We aimed to identify apatite fission-track signatures of the Ross Sea ice flows during the LGM through detrital apatite fission-track dating and modelling and multidimensional scaling (MDS) method. Thermal modelling and the presence of apatites with cooling ages of about 30-40 Ma reveal a main exhumation phase of the TAM during the Oligocene associated to the last phases of the West Antarctic Rift System. The presence of key marker apatites (e.g. younger than 21 Ma or older than 230 Ma) allows to identify the Central High as a major ice-flow divide in the Ross Sea.

4.1 Introduction

The Ross Sea embayment is a crucial area for understanding the ice dynamics as a direct response to climate changes. The Ross Sea embayment being unclosed for two-third by the two Antarctic Ice Sheets, is the natural storage of the sediments that are produced by the sub-glacial and aerial erosion and transported by glacial flows. The glacigenic sediments deposited in the Ross Embayment record the evolution of both the East and West Antarctic Ice Sheets, whose dynamics and stability along the geological time is still debated, although a number of sediments provenance studies (see Licht and Hamming, (2017) for a recent review), numerical modelling studies (e.g. Pollard and DeConto, 2009; Golledge et al., 2012; Dolan et al., 2018), and geomorphological studies have been carried out (Licht and Andrews, 2002; Mosola and Anderson, 2006).

Overall, the ice-flow evolution during the last glacial maximum (LGM) in the Ross Sea has been interpreted according to 3 different models (Fig. 1): (1) West Antarctic Ice Sheet (WAIS)-dominated model, based mainly on provenance studies, that predicts a flow from West Antarctic Ice Sheet to a relatively narrow drainage along the western Ross Sea coastline (Fig. 1B) (Stuiver et al., 1981); (2) WAIS-East Antarctic Ice Sheet (EAIS) balanced model, in which the confluence of West Antarctic ice and East Antarctic ice occurs in the central Ross Sea and ice contribution from East Antarctic and West Antarctic is equivalent (Fig. 1C) (Licht and Fastook, 1998; Denton and Hughes, 2000; Licht et al., 2005); (3) EAIS-dominated model based on numerical modelling, in which the WAIS strongly influenced the eastern

Ross Sea and the EAIS contributed with most of the ice to the central and the western Ross Sea (Fig. 1D) (Golledge et al., 2012).

The definition of ice flow pathways during the LGM is highly complicated by repeated ice advance and retreat, the huge sea area and low sample density, despite several hundred sediment cores have been collected. A major advance in understanding the glacial history came with the development of multibeam swath bathymetry (e.g. Shipp et al., 1999, 2002; Mosola and Anderson, 2006; Bart and Cone, 2012), assuming that the present-day geomorphic features formed during the most recent glacial advance and during the peak LGM, thick ice from WAIS was grounded in the western Ross Sea (Bart and Cone, 2012). However, the diachronicity of the expansion and retreat of the ice sheets through the Ross embayment such as the very different physiographic settings and the lack of a precise reliable radiocarbon ages, preclude from unambiguous reconstructions. However, understanding of ice sheet history has increased significantly over the past decade because of an increasing number of provenance studies of glacigenic sediments based on different approaches such as mineral composition of the sandy fraction (e.g. Hughes,1977; Balshaw, 1980; Anderson et al., 1992; Licht and Fastook, 1998; Denton and Hughes, 2000; Farmer et al., 2004, 2006; Licht et al., 2005; Hauptvogel and Passchier, 2012) or geochronological and thermochronological studies (e.g. Zattin et al., 2010, 2013; Olivetti et al., 2013, 2015; Licht et al., 2014; Farmer and Licht, 2016; Licht and Hemming, 2017; Perotti et al., 2017; Li et al., 2019). The key for interpret the provenance data is based on the comparison of the mineral composition of the sediment with the mineralogy of the source area. In the specific case of the thermochronology we can compare the ages of the sediments with the age of the bedrock, and moreover to have a supplementary information on the erosion history of the source. Therefore, in fact, glacigenic sediments provide a valuable amount of key-data concerning the history of sources that were eroded by the ice and thus a record of ice sheet history. Moreover, the limited exposure of bedrock geology and the inaccessibility of remote areas In Antarctica make thermochronological method a preferential tool to explore the complexity of the evolution of the Transantarctic Mountains (TAM) and also West Antarctica. This paper is based on detrital apatite fission-track data obtained on samples of post-LGM age from 18 piston cores across the Ross Sea. The distribution of different age population reveals a main exhumation phase of the TAM during the Oligocene and identifies the Central High as a major ice-

flow divide in the Ross Sea.

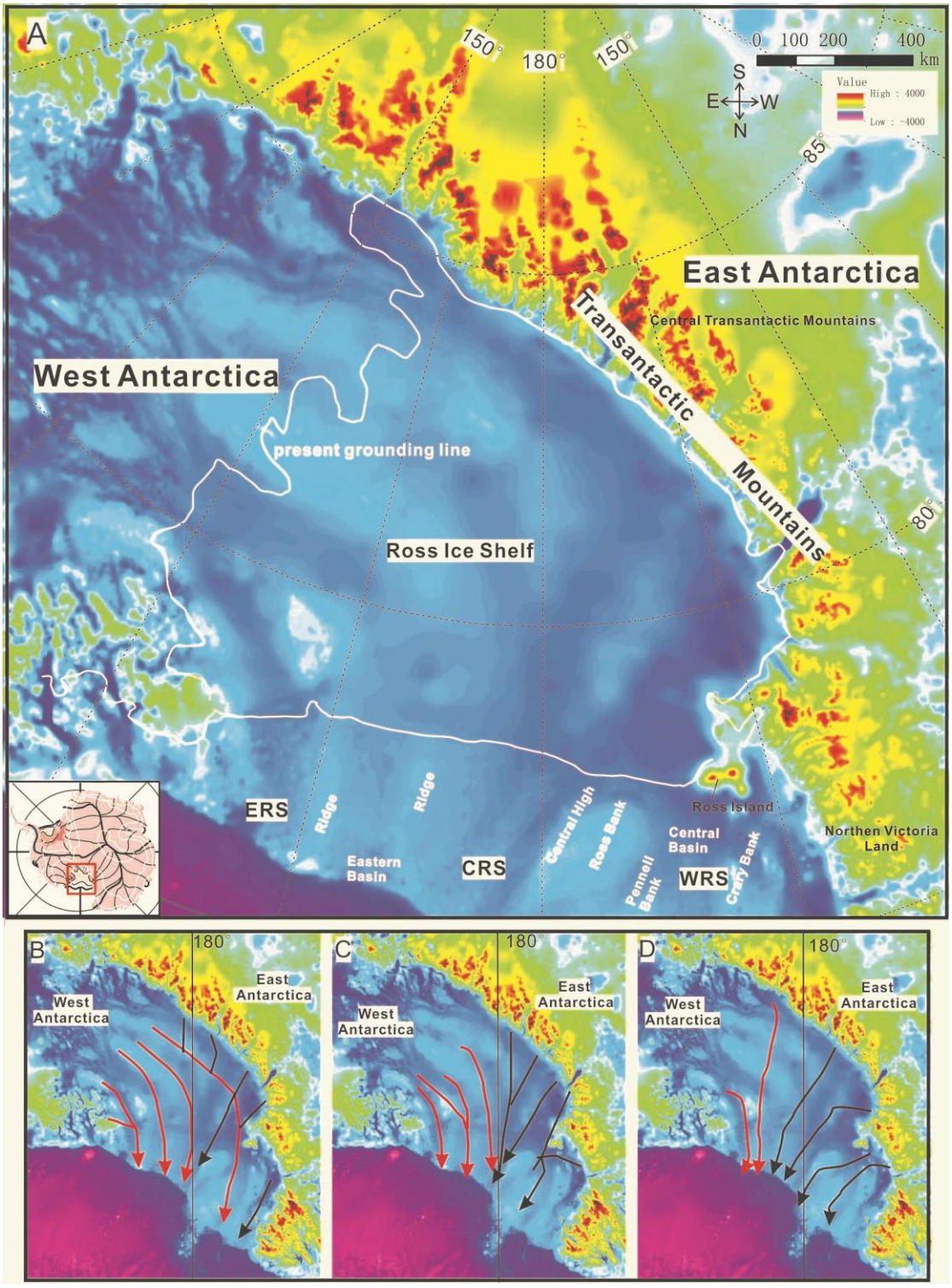

Fig. 4.1 A. the location of the study area B, C, D represent three different interpretations of the flow lines during the LGM. B and C are based on provenance studies, whereas D is based on numerical modelling (according to stuiver et al., 1981; Licht et. al, 1998; Denton et. al, 2000; Licht et al., 2005; Golledge et al., 2012).

4.2 Geological setting

4.2.1 Ross Sea

The Ross Sea, bounded by the Transantarctic Mountains along the coast of Victoria Land and the Marie Byrd Land (Fig. 4.2) is occupied mostly by the Ross Ice shelf. The present-day catchment includes about 1.65 * 106 km2 from the EAIS and 0.75 * 106 km2 from the WAIS (Rignot et al., 2008).The bathymetric features of Ross Sea consists of 6 northeast trending troughs separated by the so-called Mawson, Crary, Pennell, and Ross banks in the western Ross Sea and less prominent ridges in the east (Fig. 4.2). These troughs have similar dimensions to the ice streams that currently flow through this area. The continental shelf has gentle gradients, with a depth seaward of about 500 m and a shelf break at 500-600 m (Mosola and Anderson, 2006; Tinto et al., 2019).

The maximum ice extent in the Ross Sea has been identified at the shelf break in the central and eastern Ross Sea and slightly seaward of Coulman Island in the western Ross Sea (Kellogg et al., 1979; Anderson et al., 1992; Licht et al., 1996, 1999; Domack et al., 1999; Shipp et al., 1999; Licht and Andrews, 2002). Last Glacial Maximum till thickness is variable but all data point to eastern and central Ross Sea tills thicker than western Ross Sea tills (Shipp et al., 1999; Licht et al., 2005).

The typical stratigraphic succession of deposits sampled in piston cores from the western Ross Sea consists of an upward progression from till to proximal glacimarine to distal glacimarine sediments that generally show increasing abundance of diatomaceous material upwards (Anderson et al., 1992; Domack et al., 1999; Licht et al., 1999; McKay et al., 2008). This succession records a progressive landward shift in the retreating grounding line across the continental shelf and eventual onset of periodic open-marine conditions in the western Ross Sea (Anderson et al., 2014). Cores from the eastern Ross Sea generally consist of predominantly terrigenous glacimarine sediments resting in sharp contact on till. The absence of an upper diatomaceous facies in the central and eastern Ross Sea indicates the presence of widespread and persistent sea-ice cover that has restricted primary productivity (Dunbar et al., 1985; Licht and Andrews, 2002; Mosola and Anderson, 2006).

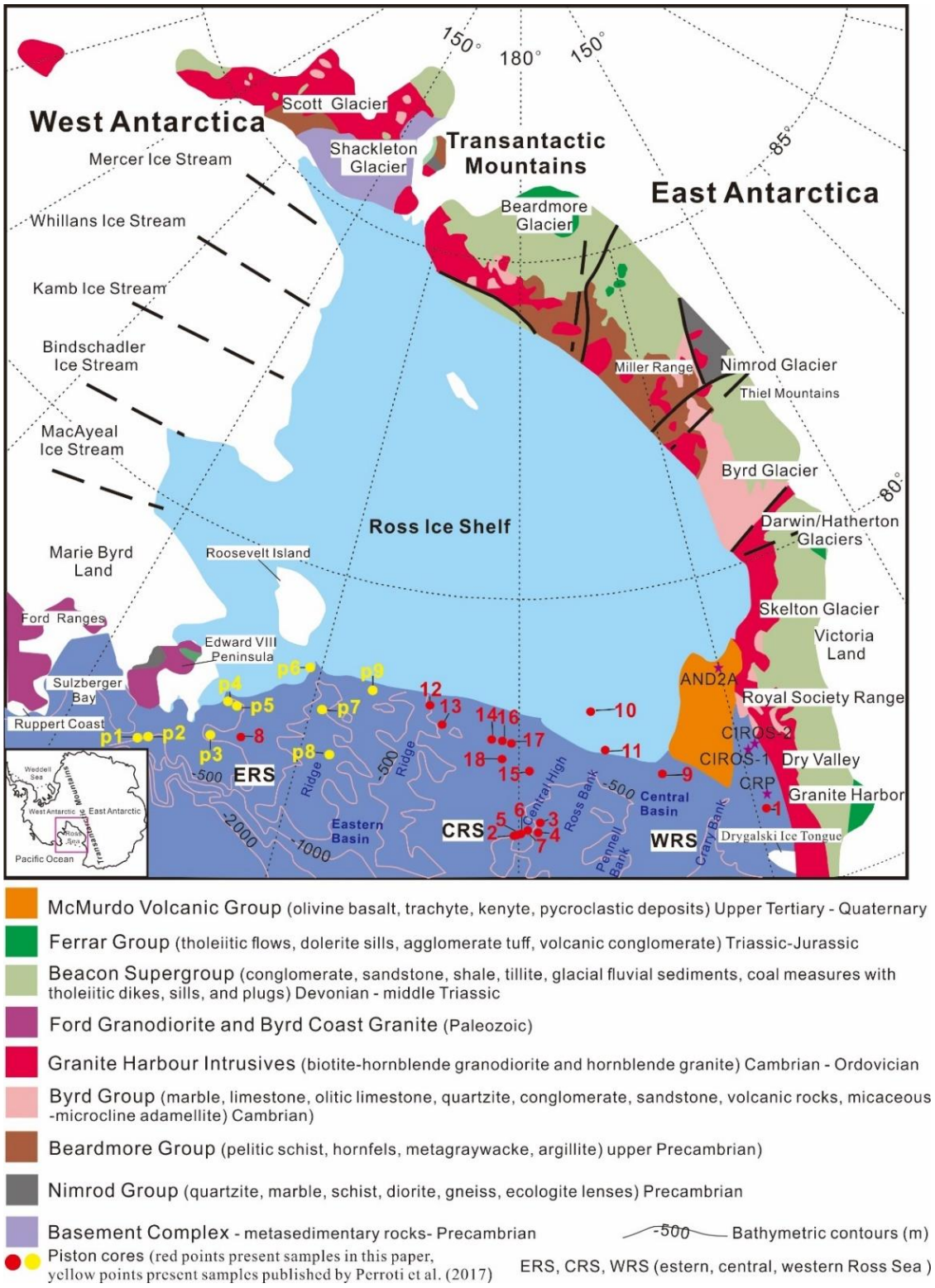

Fig. 4.2 Geological map of the Ross Sea, West Antarctic and East Antarctic with the distribution of piston cores (red points present samples in this paper, yellow points present samples published by Perroti et al. (2017). Bedrock distribution is modified according to Bushnell and Craddock, (1970), Litch et al. (2005); Bathymetric features are modified according to Mosola and Anderson, (2006).

4.2.2 The geology of West Antarctica and East Antarctica

West Antarctica is composed of four major crustal blocks: Antarctic Peninsula, Ellsworth-Whitmore Mountains, Thurston Island, and Marie Byrd Land (Dalziel and Elliot, 1982). Western Marie Byrd Land, situated today adjacent to the Ross Sea (Fig. 4.2) (Spiegel et al., 2016) is largely covered by the West Antarctic Ice Sheet and mostly grounded below sea level (Licht et al., 2005). The best-exposed rock outcrops in West Antarctic are in Marie Byrd Land (Perotti et al., 2017).

The basement is given by the Neoproterozoic-Cambrian Swanson Formation which was intruded by the Devonian-Carboniferous Ford Granodiorite suit (Bradshaw et al., 1983; Adams, 1986; Pankhurst et al., 1998; Weaver et al., 1991). It crops out mainly in the Ford Ranges in western Marie Byrd Land (Fig. 4.2) (Brand, 1979). The Swanson Formation and the Ford Granodiorite suite are both intruded by the Byrd Coast Granite (Weaver et al.,1992; Korhonen et al., 2010a, 2010b). The igneous activity involved the regions of Ruppert and Hobbs Coast (110-101 Ma) (Mukasa and Dalziel, 2000) and Ford Ranges-Edward VII Peninsula (Fig. 4.2) (Weaver et al., 1992; Pankhurst et al., 1998). Crustal extension in Cretaceous produced also the emplacement of mafic dykes throughout the Ford Ranges (Siddoway et al., 2005; Saito et al., 2013). Within the Ford Ranges, a migmatite granite complex is exposed in the Fosdick Mountains (Siddoway et al., 2004a), with orthogneisses and paragneisses which underwent at least two high-grade metamorphic events, in Devonian-Carboniferous and Cretaceous time, respectively (Korhonen et al., 2010a, 2010b, 2012; Yakymchuk et al., 2015). During the Cenozoic, starting from about 35 Ma, the region of Marie Byrd Land was affected by an intense alkaline volcanism and uplift (LeMasurier et al., 2011).

East Antarctic craton has been stable since the break-up of Gondwanaland starting at Jurassic. A major exposure of rocks of East Antarctic is in Transantarctic Mountains (TAM). The basement of the TAM is composed by the late Proterozoic- Cambrian Koettlitz and Skelton Groups (Gunn and Warren, 1962; Findlay et al., 1984; Cook and Craw, 2002) intruded by Cambrian-Ordovician Granite Harbour Intrusive Complex (Gunn and Warren, 1962; Allibone et al., 1993). Uplift and erosion followed pluton emplacement, furthermore resulting in regionally extensive Kukri Peneplain. Above

Kukri Peneplain, mainly non-marine Devonian to Triassic Beacon Supergroup deposited (Barrett, 1991). During Jurassic, a large magmatic event, both intrusive and effusive, took place along the TAM for more than 3500 km (Ferrar Large Igneous Province (Elliot and Fleming, 2008). A c. 160 Ma gap separates the Jurassic magmatism from the late Cenozoic alkaline volcanism of the McMurdo Volcanic Group. The emplacement of Ross Island volcanoes resulted in significant modification of the McMurdo Sound palaeogeography (Kyle, 1981, 1990).

The present-day exposure of the TAM is the result of different denudation episodes, well recorded by thermochronology techniques. The oldest event, based on fission-track ages, has been detected in the Thiel Mountains (Fig. 4.2) and is dated at 165-150 Ma (Fitzgerald and Baldwin, 2007). More widespread is a middle Cretaceous exhumation (ca.125-90 Ma), recorded in the Scott Glacier region (Fitzgerald and Stump, 1997), central Transantarctic Mountains (Fitzgerald, 1994) and both south and northern Victoria Land (Fitzgerald and Gleadow, 1988; Fitzgerald, 1992; Balestrieri et al., 1997; Lisker, 2002; Lisker et al., 2006; Storti et al., 2008; Welke et al., 2016). The Rb-Sr and 40Ar/39Ar age determinations on apophyllite in Ferrar basaltic rocks (Fleming et al., 1999; Molzahn et al., 1999), Rb-Sr relationships, K-Ar dates and palaeomagnetic pole positions in north Victoria Land (Faure and Mensing, 1993; Fleminget al., 1993) also support the Cretaceous denudation in large sectors of the TAM (Elliot, 2015).

Based once again on fission track data, major Cenozoic denudation and uplift of the TAM initiated during the Eocene-Oligocene between 55 to 45 Ma or 40 to 30 Ma depending on regional variability and authors (Fitzgerald 2002; Prenzel et al., 2018). This denudation event appears to get younger southward from north Victoria Land to the central TAM (Fitzgerald, 2002; Miller et al., 2010). The onset in northern Victoria Land is quite synchronous to the opening of the Adare Trough, which was active from 43 to 26 Ma (Cande and Stock, 2006). Oligocene apatite fission track ages are regionally clustered and patchy distributed all along the TAM, showing that some portion of the TAM continue to erode until the late Oligocene. This event is well described by thermochronology ages on bedrock (e.g. Fitzgerald, 1994; Miller et al., 2010; Zattin et al., 2014; Olivetti et al., 2018) and on detrital grains (Zattin et al., 2010, 2012; Olivetti et al., 2015; Li et al., 2019). Younger than Oligocene erosion is not reported in any portion of the TAM (Fitzgerald, 2002)

4.2.3 Overview of ice flow dynamics of the Ross Sea

4.2.3.1 Eastern Ross Sea

A review of the existing literature (Hughes,1977; Balshaw, 1980; Anderson et al., 1992; Farmer et al., 2004; Licht et al., 2005; Perotti et al., 2017) indicates that eastern Ross Sea (ERS in Fig. 4.2) tills are provided uniquely by West Antarctic Ice Sheet. This is proved, for example, by clay mineralogy of tills which shows the highest concentration of smectite in the ERS troughs, whereas the content in the western Ross Sea (WRS) and central Ross Sea (CRS) (Fig. 4.2) troughs is lower (Balshaw, 1980). Combining the view from Hughes (1977) that West Antarctic Ice Sheet expanded following the Ross Sea bathymetry, Balshaw (1980) speculated that high concentration of smectite in ERS probably sourced from Bindschadler, MacAyeal and Echelmeyer Ice Streams in West Antarctica. Further evidence derives from petrographic composition (pebble, coarse sand, and heavy minerals). Different works (Anderson et al., 1992; Licht et al., 2005; Perotti et al., 2017) show a significant variability from the east to west across the Ross Sea. ERS sand fraction is composed of schist and smaller quantities of gneiss, rounded quartz and granite which is quite different form WRS tills sand fraction dominantly composed of rounded quartz, granite, diamicton fragments, volcanic glass, and minor diabase and litharenite (Anderson et al., 1992). Furthermore, ERS tills are compositionally similar to West Antarctica tills, particularly in their abundance of quartz and dearth of mafic and extrusive lithic components (Licht et al., 2005). Besides, the isotopic compositional data also show strong similarities between West Antarctica and ERS (Farmer et al., 2004; Licht et al., 2005). U-Pb zircon age populations (100-110Ma, 450-475Ma, 330-370Ma) found in tills located in Bindschadler and Kamb ice streams are consistent with eastern Ross Sea tills (Licht et al., 2014). Multi analytical provenance analysis (petrographic analysis of gravel-sized clasts, geochronology and thermochronology) of samples in the eastern Ross Sea and Sulzberger Bay by Perotti et al. (2017) also implied a WAIS source. As a general pattern, the common view is that ERS is dominated by ice derived from West Antarctica, with minor if not null sources from East Antarctica.

4.2.3.2 Central Ross Sea

The analysis of sediment sources in the central Ross Sea is much more complex. The works by Farmer et al. (2006) and Farmer and Licht (2016), based on Nd, Sr and Pb isotopic signatures, indicate first that fine-grained detritus is the product of further comminution of coarser sediments. Comparison of present-day till isotopic data with existing data from fine-grained LGM tills in the central Ross Sea suggests that these were transported from East Antarctic ice that expanded through the TAM and indicates that the LGM sediments are a mixture of detritus eroded along the entire path of ice. However, the U-Pb zircon age distribution found in Whillans Ice Stream till (which is considered part of WAIS but partially originated in East Antarctica) is more similar to tills from the west- central Ross Sea (Licht et al., 2014). The region of converging East and West Antarctic ice has been hypothesized to be the CRS (Licht and Fastook, 1998; Denton and Hughes, 2000). The diagrams representing the petrographic composition of CRS till sample show a mixture of East and West Antarctic sources (Licht et al., 2005). Furthermore, most CRS till samples contain mafic intrusive lithic and mafic mineral components, which have been observed almost exclusively in the WRS and East Antarctica till samples. The mafic component is essentially absent in the ERS samples and those collected during the Ross Ice Shelf Project (Licht et al., 2005). An East Antarctica source for CRS till is also indicated by the presence of an oolitic limestone fragment in one CRS sample (Licht et al., 2005). Oolitic limestone has been mapped only in rocks of the Holyoake Range near the Nimrod Glacier, which bisects the Transantarctic Mountains (Bushnell and Craddock, 1970; Licht et al., 2005). Additionally, Nd and Sr analyses from CRS cores show low ε Nd values, indicative of an East Antarctic source terrane (Farmer et al., 2004). Most if not all the analyses support therefore the idea that the confluence of the East and West Antarctic ice sheets during the LGM occurred in the CRS (Licht et al., 2005).

4.2.3.3 Western Ross Sea

Balshaw (1980) supposed that low smectite concentration in the western Ross Sea tills probably derived from Mercer, Whillans and Kamb Ice Stream that flow from West

Antarctica. Anderson et al. (1992) found that the WRS sand fraction is dominantly composed of rounded quartz, granite, diamicton fragments, volcanic glass, and minor diabase and litharenite, therefore pointing to a source from the Beacon Supergroup, Ferrar Group, McMurdo Volcanic Group and exposures of biotite schists and gneisses near Priestly Glacier in East Antarctica. Licht et al. (2005) presented that the WRS till samples bear strong compositional similarity to East Antarctic till samples and are distinctly different from West Antarctic till samples, which supported by Nd and Sr isotopic analyses of the silt+clay fraction from the same samples by Farmer et al. (2004). Sand fraction of LGM glacier till indicates that western Ross Sea till samples exhibit mineralogic and lithological frameworks similar to East Antarctic till samples, West Antarctic-derived ice streams did not advance into the western Ross Sea (Licht et al., 2005). The U-Pb zircon age distribution found in Whillans Ice Stream till is most similar to tills from the west-central Ross Sea Results (Licht et al., 2014). Studies of till provenance and the orientations of geomorphic features on the Ross Sea continental shelf show that ice with East Antarctic origins extended across the continental shelf west of 180° (Anderson et al., 2014). Provenance studies of offshore drillings (MSSTS, CIROS-2, CIROS-1, CRP-1, CRP-2/2A, CRP-3, AND-1B, AND-2A) in McMurdo Sound in western Ross Sea reflect local geological source terrans from TAM and outlet glaciers of EAST Antarctica draining ice into western Ross Sea. What's more, Provenance studies of AND-1B, AND-2A (record the last 20 Ma) by Zattin et al. (2010, 2012) show an ice pattern dominated by south to north trending flow lines parallel to the TAM in the western Ross Sea. In all, EAIS dominated the western Ross Sea, probably with an ice flow originated from the WIS northward along the coast of TAM.

4.3 Material and Methods

The 32 samples from 18 piston cores in our work were obtained from the Antarctica Research Facility at Florida State University. They were drilled by different scientific cruises across the Ross Sea: DF78, NBP94-07, NBP94-01, NBP96-01, DF62-01, DF76, NBP00-01, NBP94-07, NBP95-01 (Table 4.1). Subsamples for analysis were chosen from cores retrieved landward of the Last Glacial Maximum grounding line in the Ross Sea. Actually, most of cores are distributed in the central Ross Sea (Piston

core 2,3,4,5,6,7,12,13,14,15,16,17) near the longitude 180°. Several cores located in the western Ross Sea (Piston core 1,9,10,11). Piston core 8 located in the eastern Ross Sea. Details on location are shown in Table 1. All of cores in this work yield samples of a stratigraphic age younger than the Last Glacial Maximum. Each of the sample, collected in the sand levels, integrates about 5 cm of materials (depth shown in Table 4.2)

Table 4.1 Information of each piston core in this work.

Sample name	Cruise	Core	Latitude	Longitude	Water depth(m)	Core length (cm)
1	DF78	014-PC	-76.5	164	424	334
2	NBP94-07	070-PC	-76.405	-179.657	512	308
3	NBP94-07	093-PC	-76.76	178.535	298	359
4	NBP94-01	027-PC	-76.522	178.881	312	235
5	NBP94-07	078-PC	-76.493	-179.963	375	270
6	NBP94-07	079-PC	-76.487	179.949	295	151
7	NBP96-01	002-JPC	-76.452	179.881	373	419
8	NBP96-01	006-JPC	-77.222	-161.476	649	341
9	DF62-01	005-PC	-77.3333	170	805	76
10	DF78	012-PC	-78.267	175.25	538	271
11	DF76	001-PC	-77.45	174.8	695	544
12	DF76	003-PC	-78.2	-174.183	558	671
13	NBP00-01	001-PC	-78.019	-176.252	578	237
14	NBP94-07	039-PC	-77.924	-178	694	103
15	NBP95-01	017-PC	-77.452	179.05	732	202
16	NBP94-07	041-TC	-77.921	-178.26	716	32
17	NBP94-07	043-PC	-77.917	-178.822	725	241
18	NBP94-07	051-PC	-77.659	-177.789	678	125

Fission track method on apatites allow to date the cooling of the rock under ~120°(and to reconstruct their time-temperature path (Reiners and Brandon, 2006). Cooling of the rock is usually produced by exhumation of the rock from depth to the surface as a consequence of surface erosion that in turn is controlled by tectonics activity and climatic forcing.

4.3.1 AFT dating and modelling

All 32 samples have been dated by apatite fission-track method. Apatite grains have been separated from piston cores and then processed for fission-track analysis through standard processing techniques. Usually 40 grains could be dated for each sample. AFT single grain ages were calculated using the external-detector and the zeta-calibration methods (Hurford and Green, 1983) with IUGS age standards (Durango

and Fish Canyon apatites; Hurford, 1990) and a value of 0.5 for the 4π/2π geometry correction factor. The analyses were subjected to the χ2 test (Galbraith, 1981) to detect whether the data sets contained any extra-Poissonian error. A χ2 probability of less than 5% denotes a significant spread of single grain dates. After using standard analytical procedures, grain- age distributions of each piston core were decomposed into different components (Table 4.2, Fig. 4.3) and plotted as combined radial and kernel density plots (Dietze et al., 2016) (Fig. 4.4).

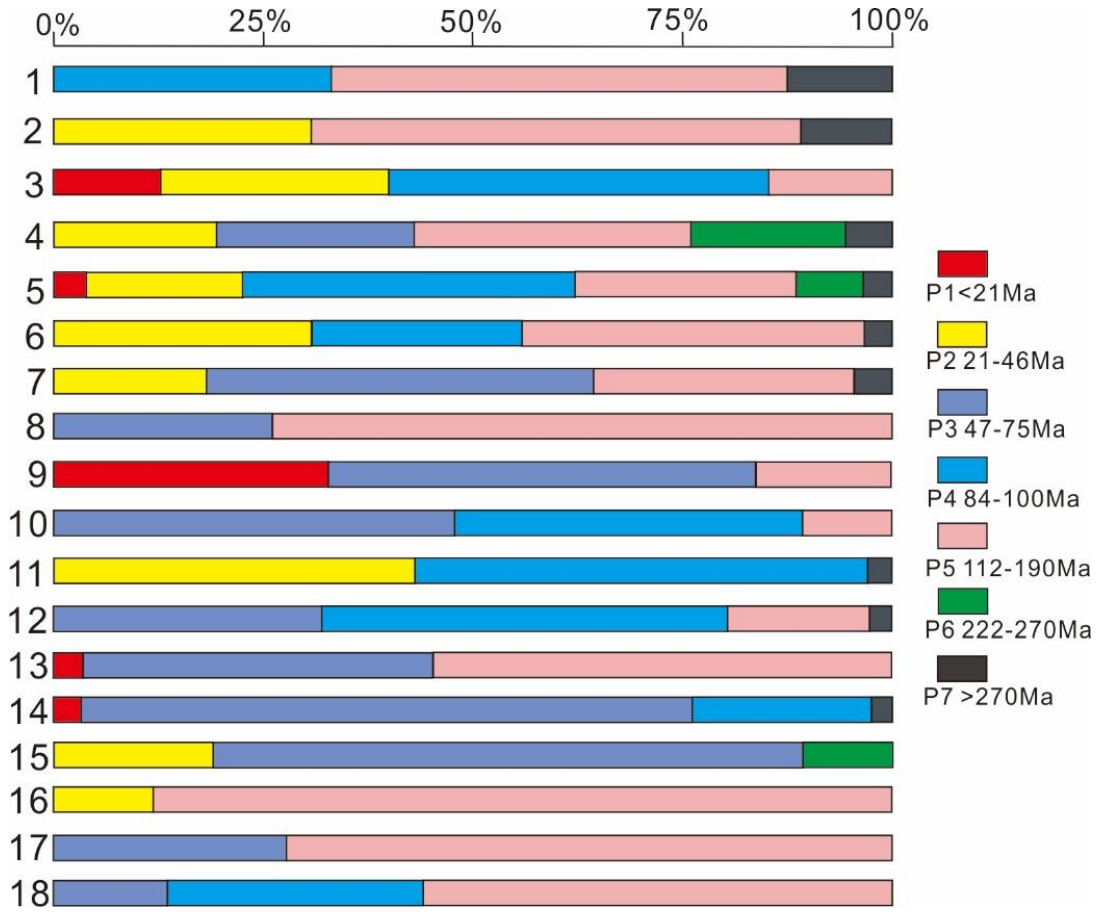

Fig. 4.3 Distribution of AFT age populations. The percentage scale on the top represents proportion of different population (sample locations show in Fig. 4.2).

Measurement of fission-track lengths was performed on all samples. In order to check the kinetics of annealing of fission tracks for each sample, we also measured the Dpar (the arithmetic mean of FT etch pit lengths measured parallel to the crystallographic c-axis (Donelick, 1993; Burtner et al., 1994).

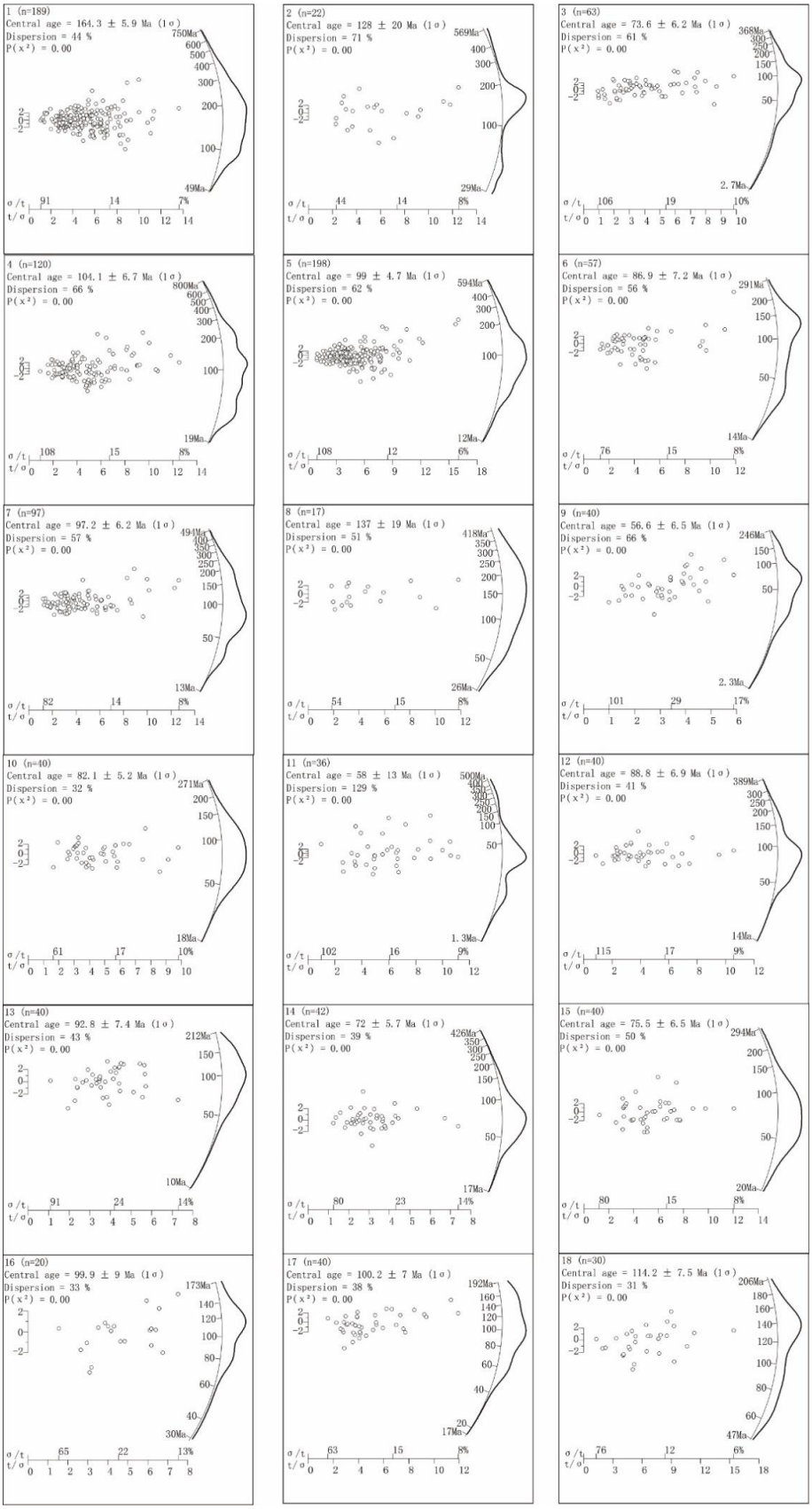

Fig. 4.4 Abanico plots (Dietze et al., 2016) of AFT age data in the Ross Sea (sample locations show in Fig. 4.2).

A

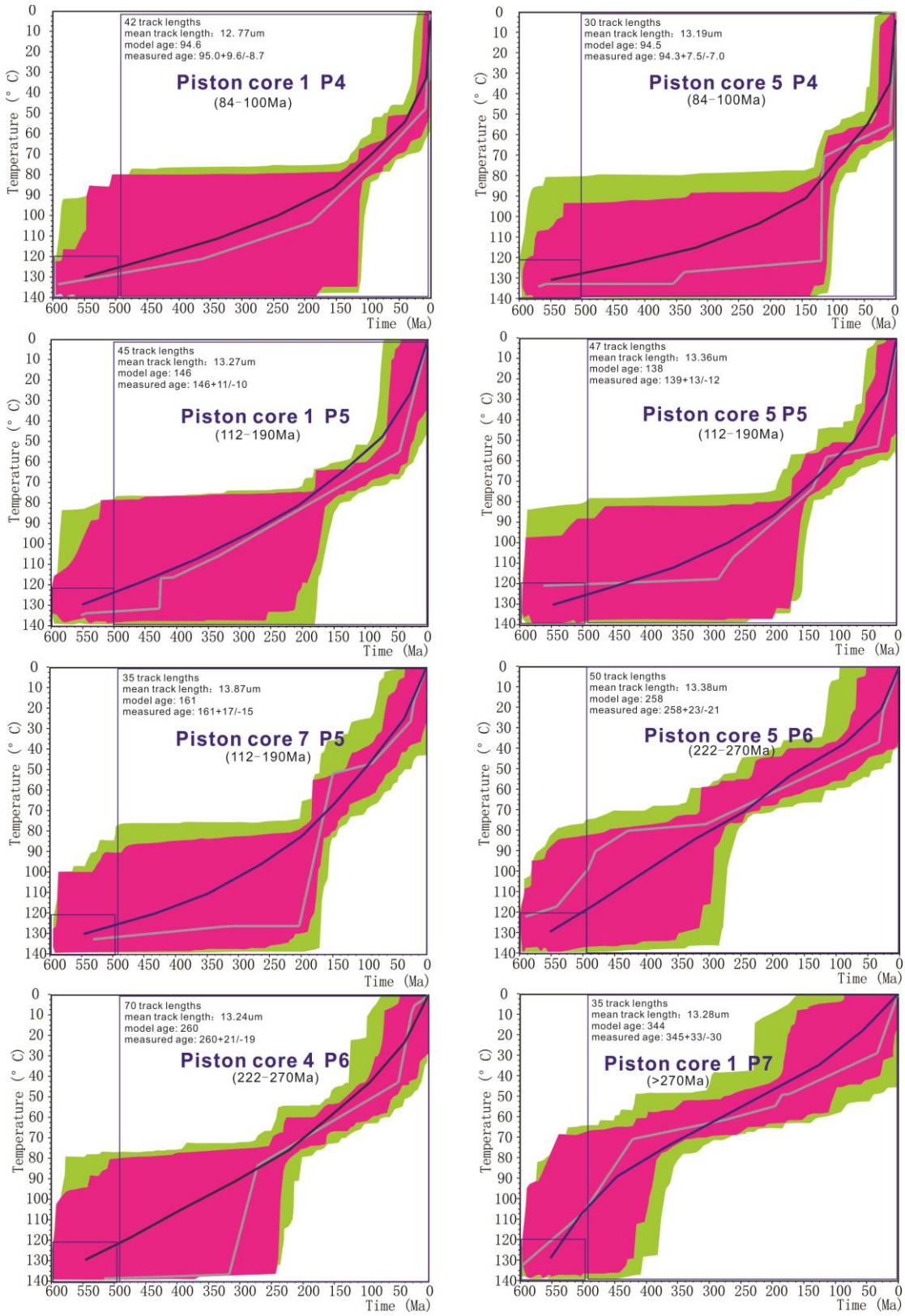
42 track lengths
mean track length: 12. 77um
model age: 94.6
measured age: 95.0+9.6/-8.7
Piston core 1 P4
(84-100Ma)
30 track lengths
mean track length: 13.19um
model age: 94.5
measured age: 94.3+7.5/-7.0
Piston core 5 P4
(84-100Ma)
45 track lengths
mean track length: 13.27um
model age: 146
measured age: 146+11/-10
Piston core 1 P5
(112-190Ma)
47 track lengths
mean track length: 13.36um
model age: 138
measured age: 139+13/-12
Piston core 5 P5
(112-190Ma)
35 track lengths
mean track length: 13.87um
model age: 161
measured age: 161+17/-15
Piston core 7 P5
(112-190Ma)
50 track lengths
mean track length: 13.38um
model age: 258
measured age: 258+23/-21
Piston core 5 P6
(222-270Ma)
70 track lengths
mean track length: 13.24um
model age: 260
measured age: 260+21/-19
Piston core 4 P6
(222-270Ma)
35 track lengths
mean track length: 13.28um
model age: 344
measured age: 345+33/-30
Piston core 1 P7
(>270Ma)
Temperature (° C)
Time (Ma)

B

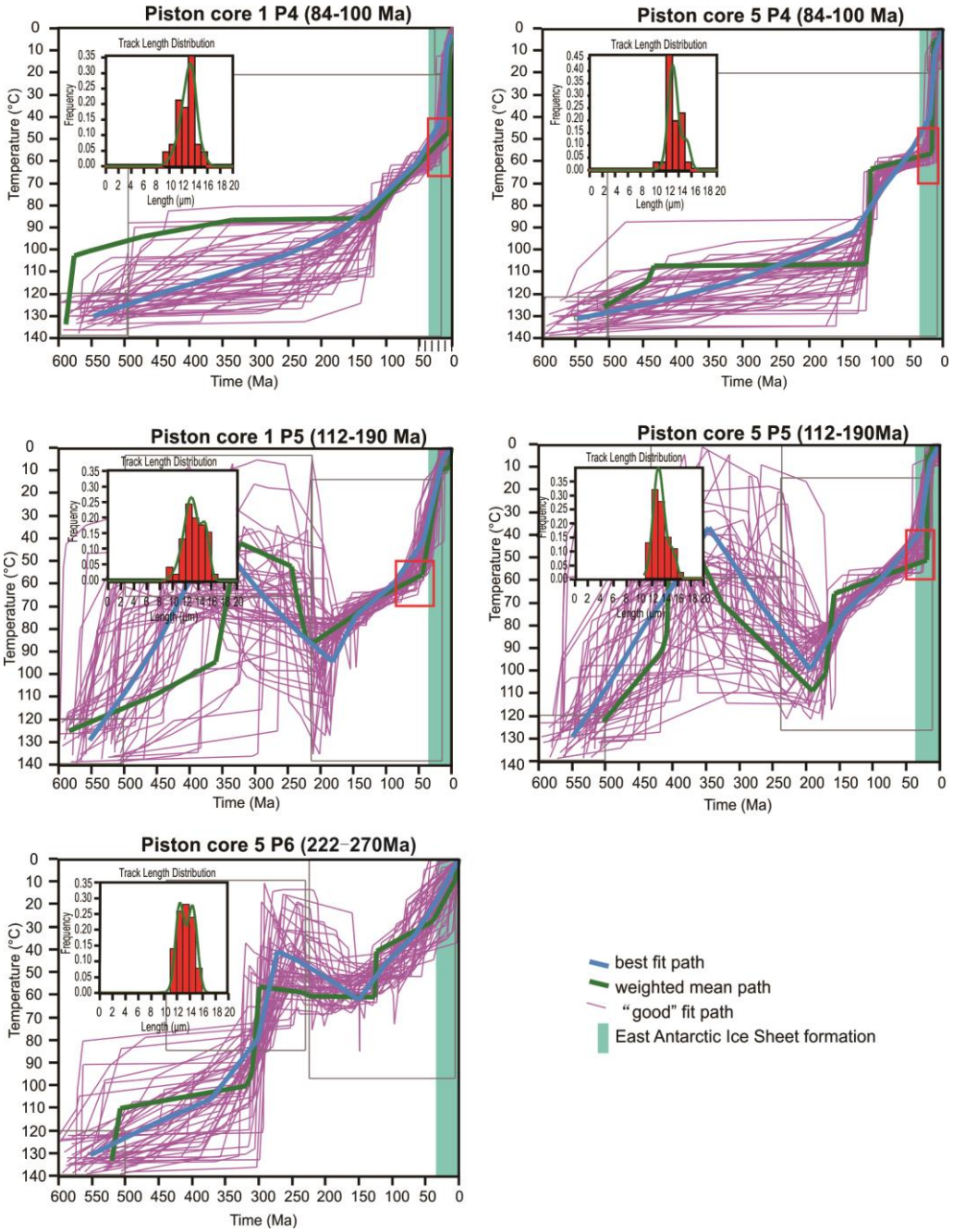

Fig. 4.5 Thermal histories resulted from inverse modeling of AFT data through HeFTy software (Ketcham, 2005). A. It shows modeling (without constrains) of P4, P5, P7 in piston core 1, P5, P6 in piston core 4, P4, P6 in piston core 5 and P5 in piston core 7. Blue lines are the weighted mean paths and grey lines are the best fit paths. Red clored zone is good path envelops and green clored zone is acceptable path envelops B. it shows modelling with constrains for P4, P5 in piston core 1, P6 in piston core 6 and P5, P6 in piston core 5.

Track length measurement can provide a further information on the thermal history of

the source rock. Length data were divided into different groups according to the age of the grain in which they were measured. As a whole, statistically meaningful length distributions have been measured on 8 populations from 4 piston cores. In order to give a quantitative evaluation of the thermal history and thus of the geologic evolution of the source rocks, these data were input into the HeFty software (Ketcham, 2005) for thermal modelling (Fig. 4.5). This program generates the possible T-t paths by a Monte Carlo algorithm and then finds a range of cooling paths compatible with the measured AFT data. Predicted AFT data were calculated according to the Ketcham et al. (2007) annealing model for fission tracks revealed by etching with HNO3 5.0 N.

4.3.2 Multidimensional Scaling (MDS) method

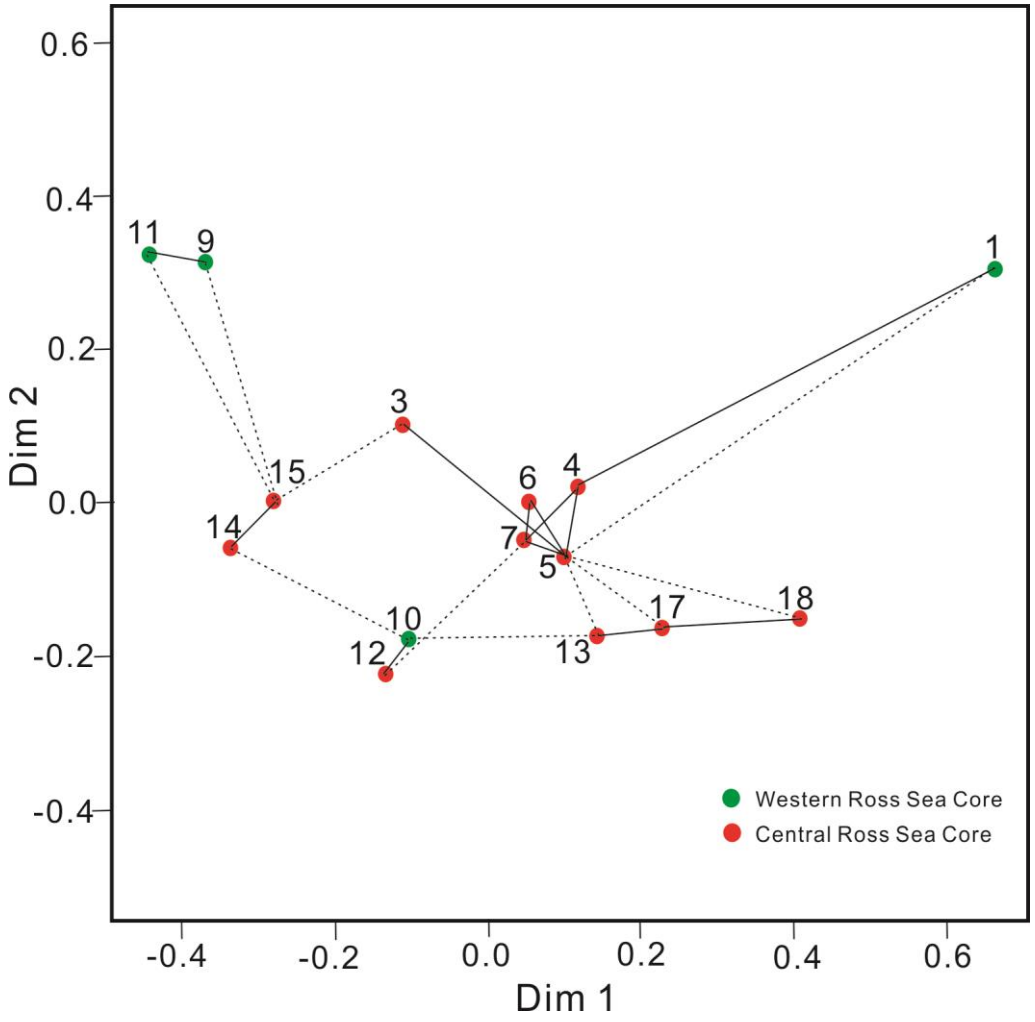

Fig. 4.6 Multidimensional Scaling results of samples related to table 4.1 showing the relative of each sample. Samples 2 and 8 are too less grains so not included. ‘similar’

samples cluster closely together, and 'dissimilar' samples plot far apart (Vermeesch, 2013). Location of samples showed in Fig 4.2. Multidimensional Scaling results of samples both in this work and in the work by Perotti et al., 2018 attached in Appendix.

The large single grain age dataset here obtained has been analyzed by the multidimensional scaling (MDS) method which has been proved to be an easy and efficient statistical technique for comparison of complex detrital geochronological data (Vermeesch, 2013). Actually, it is a dimension-reducing exploratory data analysis tool, but can capture the main features of detrital datasets. It is a robust and flexible superset of the Principal Component Analysis (PCA) which makes fewer assumptions about the data and produces a 'map' of points on which 'similar' samples cluster closely together, and 'dissimilar' samples plot far apart (Vermeesch, 2013). We use the MDS user-friendly interface provided by the website http://mudisc.london-geochron.com. In order to maximize the statistical significance of the data, we excluded some samples with few grains (sample 2, 8,16) (Fig. 4.6).

4.4 Results

4.4.1 AFT data and comparison of detrital age distribution

At least 40 apatite grains have been measured in each sample (except some samples that did not yield enough apatites). Samples analyzed from the same piston cores didn't show significant variability with depth. The same observation was done by Licht et al. (2014) on U-Pb age distributions. Therefore, considering also that the lack of high-resolution chronology within the till and thus any time-transgressive analysis of flow changes is not possible and that the number of available grains is usually very low given the scarcity of sampled material, we merged age data of different samples from the same piston cores in order to increase the robustness of statistics. As a whole, the single grain ages cover a large range, spanning from 7.9 Ma to 539.3 Ma, and all samples show over-dispersion of ages relative to values predicted for standard Poissonian variation for a single age component. We paid more attention on the youngest grains (AFT ages < ~20 Ma), those with AFT age ~30 - ~40 Ma, and the oldest population as these age groups have been revealed as the most significant in

terms of source signature (Zattin et al., 2012, 2014; Olivetti et al., 2013; Perotti et al., 2017; Li et al., 2019). However, to facilitate a discussion, we arbitrarily divided our AFT age distributions into 7 different age populations (Table 4.2, Fig. 4.3). We stress here the fact that any interpretation based on relative proportion among grain age populations must be done with caution. In fact, source of bias could be represented by vulnerability of grain-age distribution to hydraulic sorting effects and the mineral fertility of the source rock (Malusà and Garzanti, 2019).

The youngest age population (P1) comprises grains younger than 21 Ma. Generally, this age population is poorly represented in our dataset. However, it appears clearly in 3 piston cores, in core 3 and 5 located in the central Ross sea and in core 9 close to McMurdo island in western Ross Sea, although some grains are present also in piston cores 13 and 14.

Population P2 ranges from 28 Ma to 46 Ma and it is widespread present in many piston cores from the central Ross Sea (piston cores 2, 3, 4, 5, 6, 7, 15) but also in piston core 11 which is close to the western Ross Sea. It is noteworthy the absence of P2 population in the piston core 1, collected close to the Victoria Land coast.

For P3(53-75 Ma), P4(84-100Ma), P5(112-190Ma), P6(222-270) Ma, there are no clear trends of their presence in our samples. Generally, grains in these age ranges are much more abundant than other populations.

P7 groups the oldest grains, with ages higher than 270 Ma. This age population appears meaningfully in piston cores 1, 4, 5, 7 which are located in the central and the western Ross Sea. The number of grains is usually quite low with the exception of sample 1. In Figure 4.6 we show a graphical representation of the statistical similarity among the samples obtained by Multidimensional Scaling (MDS) method (Vermeesch 2013) where the solid lines mark the closest neighbors and dashed lines the second closest neighbors), Detrital data define different groups with most of samples (4-5-6-7) from the central Ross Sea that cluster closely together. Besides, samples 1 (East Antarctic coast) and samples 9-11 (western Ross Sea) both plots far from the other samples and from each other, pointing to a peculiar detrital age signature (Fig. 4.6).

Samples 4-5-6-7 are the closest neighbors. It is noteworthy that age distributions of these four piston cores show the largest age range among all piston cores. They yield 4 to 6 age populations with almost absence of grains belonging to P1 age population and similar grain abundance in populations P2 and P4. They are all located in the eastern flank of Central High (Ross Bank) in the central Ross Sea.

Samples 13-17 show most grains with an age of about 130 Ma (P5), and a further population P3 with an age of about 50-60 Ma. These two piston cores are both in the central Ross Sea and not far from the continental shelf.
The similarity of samples 10-12 is given by three main age populations at 60 Ma (P3), 90 Ma (P4) and 150 Ma (P5). They are located a bit far from each other, but at the similar latitude and very close to the border of the present Ross Ice Shelf (actually sample 10 is below the shelf).

4.4.2 Thermal model of detrital populations

Tracks for length measurement have been measured in dated grain, and only 4 populations (from a total of 4 samples) yielded a significant number of lengths. Number of the track for each population span between 35 and 71, considered a poor quantity for standard bedrock samples where it is current to use also grain not already dated. In our case, because the samples are detrital it is mandatory measure length in dated grain, that limit the amount of available grain. Track lengths relative to population P4 have been found in sample 1 and 5, track length relative to population P5 in sample 1, 5 and 7, track length relative of population P6 in sample 4 and 5 and population 7 in sample 1 for a total of 8 thermal histories (Fig. 4.5A). Mean Dpar values do not show remarkable variations (1.17 to 1.45 μm), thus indicating little if not null variation of annealing kinetics (Burtner et al., 1994; Donelick et al., 1999). The same kinetic model has been therefore applied to all the samples, whose age and length data could be modelled through the HeFty program. During the first explorative phase, no external constraints have been input because of the lack of any information about the geological evolution of possible source of the sediments. We assumed that samples were beneath the PAZ temperature between 600 and 500 Ma.
Population P4 (84 to 100 Ma) was modelled using data from samples 1 and 5 separately. Mean track length of P4 (sample 1 and sample 5) show 12.77 μm (± 1.39μm) and 13.19 μm (± 1.07 μm) respectively suggesting a slow cooling through the apatite Partial Annealing Zone (PAZ; about 120-60°C). Although the number of the measured track are limited, the thermal histories are very consistent between the two samples, showing a slow cooling through between 100 and 40 Ma when a marked increase of cooling rate occurred (Fig. 4.5A).

It could be interesting also to remark that the modeling suggests that at 95 Ma the samples were at low temperature, about 70-80 ° C, and the further flexure of the T-t paths occurred about 50-60 ° C.

Modelling of P5 (112 to 190 Ma) (in samples 1, 5, 7) gives also quite consistent results among the three samples (Fig. 4.5A). These samples are characterized by similar MTL (13.27±1.62μm, 13.36± 1.21μm and 13.87± 1.14μm respectively) that are slightly longer than younger population. Despite the longer MTL, thermal modeling of samples 1 and 5 shows a slow cooling well constrained between 160 Ma 50 Ma followed by an increase in cooling rate. Modeling of sample 7 suggests a more constant cooling rate and a faster cooling through the PAZ. The longer MTL of these samples could be due to the presence of some volcanic apatites coming from Ferrar dolerite (190 Ma) that generally are productive of apatites (see discussion of the source rock exhumation).

Track lengths relative to population P6 (200 to 270 Ma) have been found in sample 4 and 5 with values of MTL of 13.24±1.43μm and 13.38±1.14 μm respectively. Thermal modeling of the both samples yields a slow cooling from 250 to 50 Ma (Fig. 4.5A). It is interesting to remark that a constant cooling since 250 Ma is rule out and both the modelled samples suggest a slightly increase in cooling rate in the Cenozoic. Differently from younger populations, this change in cooling rate occurred a lower temperature, between 50 and 40 °C.

Population P7 （>270 Ma）could be modelled in only one sample 1 with value of MTL 13.28 ±1.50 μm, showing a slow cooling form 440 to 130 Ma with constant cooling rate.

4.5 Discussion

4.5.1 Identification of EAIS and WAIS sources

The large range of individual grain ages and the lack of systematic trends across the Ross Sea indicate the presence of multiple sources with a complex and differentiated erosional history, starting at least from to the Jurassic. Therefore, our major task was

the finding of key-data able to give an unambiguous signature to EAIS and WAIS provenance.

A first clue is given by the youngest age population (P1<21 Ma) in our AFT age dataset (Table 4.2, Fig. 4.3). Such young grains are also present in datasets detected on offshore drillholes such as CIROS-2 and ANDRILL, and were interpreted as related to the widespread Cenozoic volcanic event in the western Ross Sea (Zattin et al., 2012). On the contrary, these ages are not present in the AFT detrital distributions in the eastern Ross Sea (Perotti et al., 2017) and in the U-Pb detrital zircon signature of West Antarctic sites (Licht et al., 2014). Actually, some volcanic centers are existing in West Antarctica but their contribution to the detritus that is flowing into the eastern Ross Sea is very minor (Anderson et al., 1992; Licht et al., 2005; Perotti et al., 2017). However, it is possible that rare volcanic clasts could derive from the unexposed volcanic centers at present under the ice sheet in western Marie Byrd Land, although their emplacement ages are totally unknown (Behrendt et al., 1995, 2004; Ferraccioli et al., 2002; Luyendyk et al., 2003; Perotti et al., 2017). It is possible that erosion of these volcanic centers occurred earlier than the LGM (Licht et al., 2005). Therefore, we suggest that, where P1 population is present, a WAIS source can be excluded. In East Antarctica, except of course the surroundings of the McMurdo Volcanic Province, volcanic clasts have been detected in Royal Society Range foothills (Perotti et al., 2018) and Dry Valleys (Kyle, 1981,1990; Marchant et al., 1996; Ehrmann and Polozek, 1999; Sandroni and Talarico, 2006). Considering the location of sample 9, in which P1 clasts are abundant, we speculate that the youngest grains in this sample are derived from McMurdo Volcanic Group. Less obvious is the explanation for P1 grains in samples 3 and 5 which are located in the central Ross Sea, thus quite far from the McMurdo volcanic edifices, taking also in account that the young grains are absent in the nearby piston cores. Based on the location of existing McMurdo volcanic outcrops, Licht et al. (2005), given the widespread presence of volcanic glasses in samples from the WRS, suppose a transport distance from a few tens of kilometers to over 100 km. However, it is also possible that some apatites derived from volcanic sources located south of the McMurdo region but at present below the ice. This hypothesis was already mentioned by Zattin et al. (2012) to explain the presence of volcanic detritus in the drill-hole AND-2A. More broadly, the presence of P1 apatites, clearly of volcanic origin, represents the signature for a west-derived source, that is related to evolution of East Antarctica. In other words, the

presence of these grains in samples 3 and 5 and their absence in samples closer to West Antarctica (Perotti et al., 2017) suggests that the area of Central High was reached by EAIS-derived flows. This view is supported by the distribution of P7 apatites, that is older than 278 Ma. They appear meaningfully in piston cores 1, 4, 5, 7 which are located in the central and the western Ross Sea. Generally, exhumation ages detected on bedrock samples from East Antarctica are older than those from West Antarctica. For example, Fitzgerald (1994) detected AFT ages of 253-339 Ma in the Miller Range along the TAM whereas AFT ages in the Marie Byrd Land are Cretaceous or younger (Adams et al., 1995; Lisker and Olesch, 1998; Spiegel et al., 2016). Moreover, published detrital AFT ages from piston cores located in the eastern Ross Sea (therefore sourced certainly from West Antarctica), are all younger than 222 Ma (Perotti et al., 2017). On the contrary, sparse grains with ages older than 200 Ma have been detected offshore the TAM in the CRP, CIROS2 and Andrill wells (Zattin et al., 2010, 2012; Olivetti et al., 2013, 2015). We therefore infer that the presence of populations P1 and P7 may represent a significant signature of an East Antarctica source.

We rule out the possibility that P1 ages are not related to magmatic cooling but to exhumation. In fact, although extensional tectonics has been proved along the margins of the West Antarctic Rift System during the Neogene (Cooper and Davey, 1985; Hall et al., 2008; LaMasurier, 2008), AFT bedrock ages younger than about 20 Ma have been never found. The youngest exhumation event has been described by Spiegel et al. (2016) in eastern Marie Byrd Land at about 20 Ma.

On the contrary, the appearance of P2 apatites (28 Ma to 46 Ma) (Table 4.2, Fig. 4.3) is a clear signal of Oligocene exhumation in the source regions. These grains are well represented both in the central Ross Sea and the western Ross Sea samples. Detrital AFT ages ranging from 30 to 40 Ma have been already detected offshore the central TAM, although in older sediments (Zattin et al., 2010, 2012; Li et al., 2019). They derive from erosion of exhumed blocks exposed along the TAM front as they match exhumation phases detected on bedrock samples (Fitzgerald, 2002; Zattin et al., 2014; Olivetti et al., 2015; 2018). Actually, such AFT ages are rare in the Dry Valleys (Gleadow and Fitzgerald, 1987; Fitzgerald et al., 2006) and Granite Harbor region (Fitzgerald, 1992) but they have been detected in the Royal Society Range (Olivetti et al., 2018) and are also abundant to the south, between the Skelton and Byrd Glaciers (Huerta et al., 2011; Zattin et al., 2014) as well as much further (600 km) to the south

(Stump and Fitzgerald, 1992; Fitzgerald, 1994; Fitzgerald and Stump 1997; Miller et al., 2010). However, AFT data by Perotti et al. (2018), also show samples in the eastern Ross Sea (P3, P4, P6, P8, P9 in Fig. 4.2), possibly derived from West Antarctica, that yield grains with ages from 30 to 40 Ma. A further support to an Oligocene exhumation phase derives by results obtained by thermal modelling. In fact, a presence of a marked increase in cooling rates is visible in most of our simulations. It is noteworthy that the presence of this cooling event is irrespective of the AFT age of the modeled sample.

4.5.2 Erosion history of the source rock

The most remarkable result coming from the thermal modeling consists in the recurrent increase in cooling rate in the Cenozoic (Fig. 4.5A). In fact, a presence of a marked increase in cooling rates is visible in most of our simulations, and it is irrespective of the AFT age of the modeled sample. In this section we refined the modeling, testing different constraints derived by the known geological history of the regions surrounding the Ross Embayment (Fig. 4.5B).

In the modeling without constraints, the time-temperature paths of the P4 of the both samples (1 and 5) (Fig. 4.5A) suggests a very recent increase in cooling rate. From the geological history of the TAM, erosional event younger than 15 to 10 Ma is unlikely (see Fitzgerald, 2002), therefore we find thermal history forcing the path to be in surface during the last 15 Myr. In these modeling (Fig. 4.5B) the age of increased cooling event is contained between 32 and 29 Ma, consistent with erosional history of many region along the TAM (Prentzel et al., 2014). This increase in erosion rate occurred at low temperature (ca 60 °C) corresponding to an erosion of maximum of 2 km of crustal thickness, involving rocks were already come out from the PAZ. These paths are similar to what recently found in the internal domain of the Admiralty Mountains (same age and MTL) (Balestrieri et al., under revision), interpreted as an evidence of the Cenozoic erosional event active also in region far away from the TAM front.

Track length of population P5 show a complex distribution, therefore we tested a more complex cooling history taking into account a first Paleozoic cooling (Kukri peneplain formation) and persistence in surface during the late Paleozoic,

corresponding to sedimentation of sandstone during the Devonian (Fig. 4.5B). Even in this modeling, a Cenozoic erosional event is visible, spanning from 55 to 30 Ma (Fig. 4.5B). Similar to the P4 population this event is responsible of erosion of a limited crustal thickness of 1 or 2 km, depending on the assumed geothermal gradient.

Thermal history of population P6 is the most enigmatic. Its cooling age of 200 to 260 does not correspond to any erosional event in the TAM and probably in the entire Ross Sea region, and it is usually considered the time of the long-lasting continental sedimentation of the Beacon supergroup. In the modeling without constraint (Fig. 4.5A) a slightly increase in cooling rate seems occur between 70 and 40 Ma. It is likely that cooling age corresponds to mixed ages due to an older cooling event followed by a long-lasting persistence within the PAZ. Modeling with constraint of Beacon sedimentation are shown in figure 5B showing some paths with a Cenozoic erosional event and other paths following a constant cooling since 200 Ma. The lack of similar age along the TAM and the occurrence of this population in the sample from Central High and its absence in the sample 1 (close to TAM), may reflect the WAIS provenance and an erosional event recorded in the Marie Byrd Land only.

As a whole, this dataset suggests that an Oligocene exhumation phase was widespread in both the sides of the Ross Sea. It matched with the view that extension related to the West Antarctica Rift System was irregularly distributed across the breadth of the Ross Sea during the Paleogene (Harry et al., 2018).

Evidence of a Cenozoic (Oligocene) erosional event in sample with old AFT cooling age have interesting climatic and tectonic implication. Following the general structure of the TAM margin, the Cenozoic AFT ages are expected to be in the TAM front only, where exhumation and deformation associated to the rift shoulder uplift are focused. In the inland region, the AFT ages move rapidly toward age older than ca 50 Ma, until ca 200 Ma (Fitzgerald, 2002). It is likely that our population P4, P5 and P7 represent the rock coming from the inland of the TAM, where a Cenozoic erosion event due to tectonic uplift is not expected. Our result suggests, instead, that also inland region recorded a Cenozoic erosional event, that removed a thickness of 1 to 2 km of crust. The extent of this erosional event, not associated to a focused deformation along the TAM front, could be the evidence of a climatic signal due to the Cenozoic general descent into icehouse condition that for the East Antarctica is dated at ca 35 Ma.

4.5.3 Implications on ice flow dynamics

Given the widespread presence of P2 apatites in most of the samples, it is noteworthy its absence in the piston core 1 (Table 4.2, Fig. 4.3), located close to the East Antarctica coast. As already mentioned, on the basis of the MDS statistics (Fig. 4.6), site 1 yields a very peculiar distribution of single grain ages, clearly different from the samples collected in the central Ross Sea (piston cores 4-5-6-7) and from those more to the east. Nearby site 1 (55 km south), single grain ages of about 30 Ma had been detected on samples from Pliocene sediments in the offshore drillhole CRP (Olivetti et al., 2013). Furthermore, similar ages are present in the Plio-Pleistocene samples from the CIROS-2 well (Li et al., 2019). In general, literature agrees on a northward ice flow along the coast of TAM, that was able to bring sediments from the outlet glaciers of East Antarctica (Zattin et al., 2010; 2012; Olivetti et al., 2013; 2015). Our data demonstrate that sediments transported by the ice flow from the south did not reached the site 1 (Fig. 4.7) and therefore the supply is mainly from the local East Antarctica outlet glaciers. However, although maximum ice sheet advance reached site 1, as demonstrated by Anderson et al. (2014), the interplay between west- and south-derived ice flow along the Drygalski Through was complex, with one prevailing on the other, during the ice retreat after the LGM.

Considering the AFT populations P1 and P7 (Table 4.2, Fig. 4.3) as marker signals for a provenance from East Antarctica as discussed above, the Central High seems to represent a major divide between EAIS and WAIS flows (Fig. 4.7). A similar conclusion was suggested by Licht and Fastook (1998), Denton and Hughes (2000), Licht et al. (2005, 2014) on the basis of different datasets. From a topographic point of view, the convergence of ice is marked by two merging sets of mega-scale glacial lineation detected by multibeam swath bathymetry (Shipp et al., 1999; Anderson et al., 2014; Tinto et al., 2019). These results are also broadly consistent with the paleo-flows estimated by numerical modelling by Golledge et al. (2013).

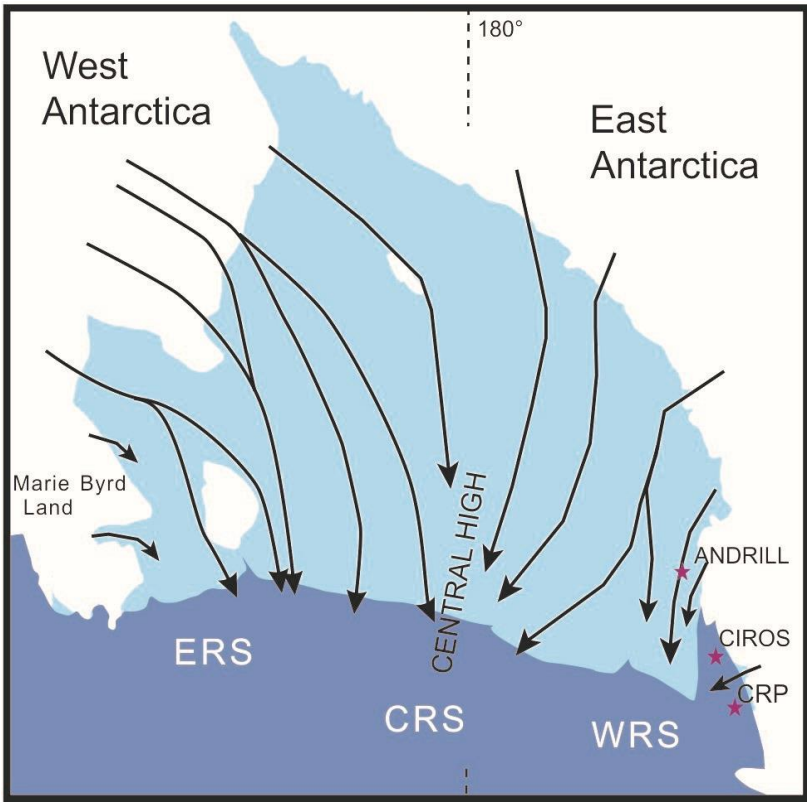

Fig. 4.7 Ice flow lines of the Ross Sea Ice Sheet during the LGM (Based on Apatite fission-track signatures and references according to Licht et al., 2005, 2014; Zattin et al., 2010,2012; Anderson et al., 2014; Perotti et al., 2017 and Li et al., 2019).

4.6 Conclusions

This work shows that detrital AFT analysis can be a valuable tool to reconstruct not only the sedimentary provenance pattern but also the erosional history of a region where bedrock geology is poorly known. In fact, the samples here analyzed offer a picture of the ice-flow dynamics after the LGM in the Ross embayment but, at the same time, capture the signals given by differential exhumation of East and West Antarctica.

The overall framework derived from statistical analysis of age groups indicates a complex exhumation of the Transantarctic Mountains and the regions belonging to West Antarctica starting at least since the Jurassic. However, thermal modelling and the presence of apatites with cooling ages of about 30-40 Ma suggests that an Oligocene exhumation event, associated to the last phases of the West Antarctic Rift System, is widespread all along the margins of the Ross Sea, therefore affecting both

West and East Antarctica. Further tectonics related to the rift during the Neogene did not produce any relevant exhumation.

The presence of key marker apatites (e.g. younger than 20 Ma or older than 230 Ma) allows to identify the Central High as a major ice-flow divide (Fig. 4.7). West of the Central High, the ice flow is from East Antarctica, with general northwards trend but with local flows from outlet glaciers, especially during ice sheet retreat phases. East of the Central High, sediments derived mainly by West Antarctica, with only minor contributions from the southernmost portion of the TAM and the lack of any significant input from the inner Marie Byrd Land (Fig. 4.7).

sample name	cruise-sample	Depth(m)	*No. of crystal*	P1(%)	P2(%)	P3(%)	P4(%)	P5(%)	P6(%)	P7(%)
1	DF78-014	25-32 102-107 187-192 242-247 297-302	189				98.8±4.3 (36.2%)	189.4±7.75 (51.1%)		393.2±22.01(12.7%)
2	NBP94-07-070	0-3	22		40.3±3.65 (30.6%)			155.8±7.45 (58.5%)		539.3±103.45 (10.9%)
3	NBP94-07-093	12-17 35-40	63	7.9±1.7 (12.1%)	45.8±3.1 (27.9%)		90.7±4.95 (45.3%)	170.7±15.15 (14.7%)		
4	NBP94-01-027	12-17 126-130 184-188	120		36±2.8 (19.5%)	64.3±4.7 (23.5%)		112.3±5.3 (33.4%)	214.6±12.25(18.3%)	466.4±35.7 (5.3%)
5	NBP94-07-078	77-82 92-97 132-137 154-159 235-239	198	19±1.9(4.4%)	41.4±2.35(18.7%)		84.1±4 (39.8%)	145.8±6.9 (26.5%)	268.4±13.75 (7.6%)	462.9±36.7 (3.1%)
6	NBP94-07-079	5-10 73-75 95-100	57		34±2.6(31.2%)		84.6±6.05 (25%)	137.2±8.05 (41.5%)		286.3±25.95 (2.4%)
7	NBP96-01-002	1-3 81-84 360-365	97		30.9±3.9 (13.2%)	73.5±3.7 (46.3%)		147.5±7.55 (31.3%)		278.7±19.35 (9.2%)
8	NBP96-01-006	18-24	17			55.2±10.4 (26.6%)		160.9±8.75(73.4%)		
9	DF62-01-005	28-32	40	20.8±2.9(33.3%)		64.4±7.2(51.1%)		149.6±20.6(15.6%)		
10	DF78-012	245-248	40			61.2±5.9(48.8%)	97.7±10.45(40.8%)	153.4±24.65(10.4%)		
11	DF76-001	280-287	36		28.3±3.5(43%)		84.1±7.95(54.2%)			485.3±253.45(2.8%)
12	DF76-003	579-583	40			57.4±6.55(31.6%)	88±3.5(48.2%)	148.5±18.4(17.5%)		378.2±108.4(2.7%)
13	NBP00-01-001	100-105	40	13.6±6.8(3.8%)		63.6±7(41.6%)		132±2.9(54.7%)		
14	NBP94-07-039	45-51	42	18.7±6.3(3.7%)		64±7.05(72.9%)	99.5±23.45(20.8%)			412.6±159(2.6%)
15	NBP95-01-017	179-187	40		34.1±4.6(19%)	74.5±6.45(70.2%)			222.1±27.2(10.7%)	
16	NBP94-07-041	0-5	20		35±8.5(12.1%)			112.6±4.6(87.9%)		
17	NBP94-07-043	94-98	37			53.4±9.65(28%)		125.8±8.5(72%)		
18	NBP94-07-051	100-105	30			56.7±8.75(13.6%)	93.3±10(30.3%)	144.3±12.55(56.1%)		

Table 4.2 Apatite fission track data of samples collected from piston cores in the Ross Sea (the location of piston cores shows in Fig. 4.2). Each data is from emerging several samples' AFT age data together which are collected from different depth in the same piston cores.

Chapter 5

Conclusion

1. The work based on detrital AFT data from the CIROS-2 sedimentary record provides new information about ice flow in the McMurdo Sound area during the last 5 Ma:

(1) In early Pliocene, the presence of a volcanic component (P1) from the oldest McMurdo eruption centers suggests a south-north ice flow over the McMurdo Sound. This south-north ice flow is related to a WAIS expansion.
(2) In the late Pliocene, local source of sediments (P2, P3, P4, P5) testifies a glacial expansion of outlet glaciers, therefore supporting the idea of an EAIS expansion.
(3) Since the early Pleistocene, AFT data record a dominantly local provenance (i.e. from the Ferrar and outlet glaciers) with an irregular mix of ages, due to ice periodically invading and retreating across the McMurdo Sound.

2. The work based on detrital AFT data from the post-LGM piston cores across the Ross Sea provides new information on the exhumation of TAM and new inputs about ice flow model of Ross Sea.

(1) The overall framework derived from statistical analysis of detrital ages indicates a complex exhumation of the Transantarctic Mountains and the regions belonging to West Antarctica starting at least since the Jurassic. However, thermal modelling and the presence of apatites with cooling ages of about 30-40 Ma suggests that an Oligocene exhumation event, associated to the last phases of the West Antarctic Rift System, is widespread all along the margins of the Ross Sea, therefore affecting both West and East Antarctica. Further tectonics related to the rift during the Neogene did not produce any relevant exhumation.
(2) The presence of key marker apatites (e.g. younger than 21 Ma or older than 230 Ma) allows to identify the Central High as a major ice-flow divide. West of the

Central High, the ice flow is from East Antarctica, with general northwards trend but with local flows from outlet glaciers, especially during ice sheet retreat phases. East of the Central High, sediments derived mainly from West Antarctica, with only minor contributions from the southernmost portion of the TAM and the lack of any significant input from the inner Marie Byrd Land.

3. As a conclusive remark, this work shows that detrital AFT analysis can be a valuable tool to reconstruct not only the sedimentary provenance pattern but also the erosional history of a region where bedrock geology is poorly known.

Appendix

Data repository Chapter 3

1. Single grain AFT data

C1 40				C2 40				C3 36				C4 40			
Zeta:	344.09	Zeta err.:	10.36	Zeta:	344.09	Zeta err.:	10.36	Zeta:	344.09	Zeta err.:	10.36	Zeta:	344.09	Zeta err.:	10.36
		RhoD:	1378182			RhoD:	1362545			RhoD:	1339091			RhoD:	1331273
		Nd:	6943.636			Nd:	6864.909			Nd:	6746.818			Nd:	6707.455
Ns	Ni	Area(μm^2)	Age (Ma)	Ns	Ni	Area (μm^2)	Age (Ma)	Ns	Ni	Area(μm^2)	Age (Ma)	Ns	Ni	Area(μm^2)	Age (Ma)
126	323	7352	91.96	39	96	3453	94.36	1	39	9626	5.91	3	51	7034	13.45
1	23	5138	10.31	28	111	5198	58.75	15	77	2591	44.75	6	90	6319	15.24
9	36	6274	59.08	4	24	2123	38.88	48	532	8450	20.77	47	417	3630	25.74
42	135	5594	73.44	64	202	3664	73.71	115	377	6835	69.94	160	1182	7762	30.9
3	35	2054	20.32	2	84	6876	5.57	15	77	1789	44.75	74	112	3902	149.44
43	105	1749	96.5	27	173	5283	36.41	1	32	6489	7.2	108	605	3447	40.72
32	74	5240	101.86	5	45	7461	25.95	39	251	8194	35.72	5	38	3727	30.04
7	18	4415	91.68	32	125	2763	59.62	88	374	8623	54.02	47	117	3877	91.27
1	32	4863	7.42	5	23	2508	50.67	80	378	8731	48.61	70	358	5882	44.59
5	67	8835	17.69	35	79	2872	102.84	1	60	6053	3.84	54	331	1992	37.22
83	513	9483	38.3	12	138	3263	20.31	1	9	2867	25.56	24	113	5253	48.42
48	257	8115	44.19	52	344	4355	35.27	85	645	8375	30.31	13	64	2756	46.31
1	18	8726	13.18	36	237	6531	35.44	12	92	2886	30	133	415	3080	72.92
64	390	5324	38.84	5	24	1726	48.56	1	34	6349	6.78	40	236	5209	38.67
24	101	5427	56.17	115	452	3965	59.26	151	473	3097	73.18	204	915	4905	50.81
35	96	6004	85.98	13	55	1800	55.07	13	175	5209	17.1	12	56	7713	48.85
68	222	6516	72.32	5	28	3016	41.65	70	229	5808	70.09	12	21	7768	129.45
75	121	3437	145.51	1	6	7007	38.88	95	535	5873	40.81	16	124	7831	29.46
21	48	3840	103.04	4	61	2344	15.32	197	1381	3871	32.8	60	134	4874	101.65
2	17	8510	27.87	27	111	2660	56.66	42	322	6039	30	48	134	2289	81.45
76	272	4722	66	23	127	4416	42.24	2	8	5521	57.38	21	122	2092	39.27
3	35	2345	20.32	40	320	5605	29.18	9	44	2296	46.98	86	600	5888	32.71
52	416	2504	29.61	12	100	4690	28.02	51	135	3579	86.51	47	393	7516	27.31
13	15	2105	202.55	26	179	3422	33.9	14	120	6559	26.84	63	399	8527	36.03
35	246	2260	33.69	6	38	1906	36.84	35	158	3725	50.87	21	103	4289	46.48
2	18	7736	26.33	92	307	8034	69.74	68	262	5761	59.56	37	96	6233	87.59
53	149	7283	83.9	15	45	5395	77.53	29	130	2761	51.22	15	70	7306	48.85
50	150	2413	78.66	30	119	5006	58.72	73	169	8530	98.82	1	49	3904	4.67
28	144	2590	46	107	654	5464	38.17	34	177	4378	44.13	6	61	5353	22.47
45	225	5545	47.31	8	48	2214	38.88	75	412	5518	41.83	26	134	5156	44.25
40	110	3090	85.76	12	69	5286	40.56	2	15	2932	30.67	23	226	4514	23.25
13	62	3547	49.59	13	70	2141	43.31	5	47	2470	24.48	125	584	5901	48.79
34	115	2840	69.81	60	208	7891	67.14	21	77	6604	62.57	5	38	4976	30.04
34	212	3207	37.97	112	680	9439	38.42	74	286	7673	59.38	45	210	7156	48.85
18	84	3203	50.68	32	90	4615	82.66	4	16	2236	57.38	48	166	7130	65.83
16	38	4403	99.2	138	439	4378	73.14	1	23	6314	10.02	51	139	4944	83.41
70	465	7668	35.64	5	34	3193	34.32					29	136	5699	48.61
135	650	8972	49.12	20	90	3996	51.79					15	21	7688	161.41
4	14	5576	67.48	24	141	6490	39.7					18	110	3554	37.33
25	166	3375	35.66	63	368	3078	39.93					1	48	5406	4.77

C5 50				C6 40				C7 40				C8 40			
Zeta:	344.09	Zeta err.:	10.36	Zeta:	344.09	Zeta err.:	10.36	Zeta:	344.09	Zeta err.:	10.36	Zeta:	344.09	Zeta err.:	10.36
		RhoD:	1315636			RhoD:	1292182			RhoD:	1268727			RhoD:	1253091
		Nd:	6628.727			Nd:	6510.636			Nd:	6392.545			Nd:	6313.818
Ns	Ni	Area(μm^2)	Age (Ma)	Ns	Ni	Area(μm^2)	Age (Ma)	Ns	Ni	Area(μm^2)	Age (Ma)	Ns	Ni	Area(μm^2)	Age (Ma)
73	702	7940	23.57	15	41	3536	80.69	55	245	3925	48.86	2	20	9057	21.47
23	158	4764	32.97	60	152	6115	87.02	26	71	2445	79.52	18	28	4469	136.79
30	280	4003	24.29	218	1531	4987	31.52	66	103	3869	138.51	3	28	2484	23
42	192	5536	49.49	31	302	5918	22.74	3	86	3536	7.62	13	12	2974	228.87
83	231	7002	81.09	4	22	1981	40.23	13	49	3539	57.71	1	22	5537	9.77
2	25	4254	18.14	13	63	3403	45.63	25	177	5610	30.79	3	41	9853	15.72
39	65	4568	134.84	11	48	4898	50.66	167	556	5949	65.3	38	395	9609	20.66
181	1236	4676	33.17	29	178	4461	36.06	32	65	2746	106.68	3	32	4414	20.13
25	55	5431	102.41	2	12	4280	36.88	13	63	3009	44.93	3	16	2884	40.2
62	187	8114	74.86	45	186	5185	53.47	30	208	6006	31.44	7	37	3263	40.56
11	47	3543	52.93	75	165	7187	100.1	54	286	8168	41.12	2	27	7179	15.91
102	258	7987	89.16	8	31	3762	57.02	1	17	4885	12.84	24	95	2158	54.1
35	79	4586	99.84	9	19	1791	104.28	1	23	5511	9.49	22	33	1612	141.8
51	188	7052	61.31	10	20	2439	110.02	26	98	6451	57.71	14	41	2858	73.02
43	72	3342	134.22	56	189	8951	65.43	16	37	1780	93.8	1	36	2365	5.97
1	6	2362	37.74	5	22	5425	50.24	30	91	5097	71.63	3	58	6270	11.11
91	280	7645	73.39	3	28	2933	23.74	52	99	2328	113.76	32	24	3102	280.55
5	94	6837	12.07	16	576	5816	6.16	11	41	4407	58.36	45	247	4364	39.06
32	310	8891	23.4	64	94	3242	149.36	3	31	5834	21.11	1	33	3785	6.51
45	122	4086	83.23	37	58	3132	140.05	15	57	2093	57.24	24	144	3946	35.74
52	236	4610	49.85	23	40	2387	126.37	35	178	8071	42.82	75	247	5047	64.97
59	216	4288	61.74	14	57	3450	54.28	45	157	6082	62.32	2	23	5095	18.67
45	210	5691	48.48	59	192	5810	67.84	28	268	4968	22.79	2	23	3542	18.67
166	516	7741	72.65	12	23	2193	114.77	12	99	6730	26.43	2	12	4079	35.74
76	320	6572	53.71	11	18	1658	134.22	13	39	4519	72.42	20	103	5228	41.62
7	18	2849	87.72	14	65	3473	47.63	1	48	7635	4.55	148	526	4434	60.23
8	88	7904	20.61	11	33	1859	73.56	37	177	4979	45.51	90	320	5104	60.2
3	35	3539	19.44	20	74	2954	59.71	54	365	6220	32.24	3	67	4473	9.62
24	70	6307	77.4	38	46	3256	180.78	20	85	4128	51.21	1	30	5355	7.16
9	87	6198	23.45	73	214	5044	75.27	123	514	5347	52.08	2	35	8205	12.28
30	298	4210	22.82	50	207	3462	53.39	1	51	9061	4.28	66	237	7829	59.61
65	384	7519	38.33	51	142	4369	79.22	85	343	8879	53.92	2	27	8029	15.91
51	185	2059	62.3	48	145	4731	73.05	36	186	5237	42.15	1	30	2111	7.16
30	360	8197	18.9	13	741	4800	3.89	23	105	7029	47.68	68	218	6635	66.74
3	12	5445	56.53	6	25	2736	53.05	12	126	7130	20.78	23	121	5153	40.75
53	279	6614	43	30	130	6904	51.01	2	30	2784	14.55	2	102	8318	4.22
75	376	3924	45.14	15	34	1760	97.18	38	154	6981	53.69	80	398	4997	43.08
47	183	3187	58.06	124	464	4988	59.04	45	339	7644	28.94	18	72	2780	53.54
28	158	5995	40.12	33	90	2796	80.87	48	206	8366	50.71	3	153	6038	4.22
10	71	4951	31.91	105	221	4807	104.59	33	283	7513	25.43	1	17	5236	12.64
44	146	3776	68.08												
28	70	6849	90.21												
38	135	5453	63.61												
1	32	4601	7.09												
48	156	4037	69.5												
108	234	8888	103.97												
13	97	1906	30.36												
3	12	3451	56.53												
27	258	3482	23.72												
35	153	6136	51.74												

C9 40				C10 50				C11 40				C12 40			
Zeta:	344.09	Zeta err.:	10.36	Zeta:	344.09	Zeta err.:	10.36	Zeta:	344.09	Zeta err.:	10.36	Zeta:	344.09	Zeta err.:	10.36
		RhoD:	1237455			RhoD:	1221818			RhoD:	1206182			RhoD:	1190545
		Nd:	6235.091			Nd:	6156.364			Nd:	6077.636			Nd:	5998.909
Ns	Ni	Area(μm^2)	Age (Ma)	Ns	Ni	Area(μm^2)	Age (Ma)	Ns	Ni	Area (μm^2)	Age (Ma)	Ns	Ni	Area(μm^2)	Age (Ma)
59	115	6253	108.53	31	66	1731	97.84	16	91	5072	36.5	80	279	5060	58.44
93	382	7344	51.73	3	12	3471	52.26	2	6	2533	69.02	23	35	2339	133.15
18	13	2015	288.82	17	84	5472	42.34	1	16	6000	13	23	41	2900	113.84
7	14	2445	105.8	297	612	3427	101.06	27	102	3991	54.87	50	196	1977	52.02
9	344	3571	5.58	95	231	1910	85.75	4	28	6121	29.67	62	125	4526	100.76
6	13	2067	97.72	150	640	7763	49.01	99	298	7419	68.79	88	160	6241	111.63
39	98	3796	84.34	53	219	4256	50.6	89	199	5280	92.44	50	221	3523	46.15
25	210	5928	25.35	36	126	4475	59.69	4	35	1822	23.75	43	141	4346	62.14
2	76	6908	5.61	8	118	3229	14.21	45	102	1877	91.19	10	16	2434	126.71
30	60	5008	105.8	79	352	4392	46.94	38	192	4490	41.07	33	125	2452	53.82
53	209	6262	53.87	3	38	8037	16.55	9	61	3833	30.64	14	65	2365	43.95
55	190	4710	61.46	29	103	2493	58.83	26	77	2724	69.91	51	80	3273	129.21
65	277	2579	49.87	85	618	9524	28.8	40	91	4014	90.86	39	135	3600	58.88
42	70	3296	126.75	130	668	6950	40.72	10	173	1794	12.02	36	142	4103	51.7
3	16	2622	39.88	22	42	3728	109.02	36	51	2316	145.3	14	51	2545	55.96
14	58	2757	51.29	29	95	3877	63.76	30	111	1988	56.02	9	48	2350	38.27
35	167	5114	44.56	62	274	7489	47.32	68	213	7875	66.12	52	195	4084	54.37
50	162	2297	65.51	69	171	6697	84.14	9	42	2132	44.46	1	104	3460	1.97
36	71	2503	107.27	5	13	3698	80.23	1	30	3736	6.94	3	12	3664	50.98
20	77	1722	55.18	21	144	2377	30.54	2	23	4856	18.08	1	16	2631	12.78
73	194	3678	79.78	32	34	1725	194.58	6	868	5376	1.44	14	35	2065	81.38
29	78	3369	78.83	105	364	3427	60.26	122	351	3124	71.95	16	94	2623	34.75
2	12	6907	35.46	21	92	4597	47.73	72	171	4990	87.06	1	5	2016	40.82
18	48	5429	79.51	109	445	2920	51.21	1	39	3323	5.34	24	65	1938	75.15
92	541	8942	36.18	5	11	3369	94.71	16	40	3284	82.74	1	6	2657	34.03
69	276	4343	53.11	1	20	4001	10.49	4	10	5008	82.74	36	123	2971	59.65
16	70	2296	48.58	2	7	1701	59.69	45	258	3478	36.21	14	85	2574	33.63
116	267	6841	92.03	142	484	4373	61.29	85	447	6146	39.46	11	54	3002	41.57
1	14	2221	15.22	51	135	1904	78.81	2	352	3593	1.18	103	265	5549	79.09
38	153	3644	52.77	7	29	3983	50.47	84	369	3933	47.22	8	43	4986	37.98
181	657	6942	58.51	42	189	4310	46.48	20	33	2935	124.95	40	136	4274	59.94
305	966	8326	67.01	3	22	5067	28.56	8	34	1626	48.8	36	94	3537	77.94
12	48	5937	53.11	1	16	7985	13.11	1	27	4779	7.71	2	9	2412	45.34
10	38	5597	55.9	1	22	3763	9.53	36	138	3108	54.08	34	114	2979	60.77
26	81	5622	68.12	144	346	4087	86.77	85	278	4710	63.34	97	427	4742	46.34
1	13	3010	16.39	50	123	3054	84.76	18	117	2705	31.95	5	31	2266	32.94
33	84	4068	83.27	19	196	2733	20.31	5	51	1607	20.38	40	103	2051	79.02
23	122	3678	40.09	22	41	4439	111.65	17	76	3923	46.4	7	261	3624	5.49
46	323	7609	30.31	104	500	6786	43.51	4	12	4224	69.02	69	157	4150	89.36
25	94	5167	56.49	29	117	3806	51.82	34	175	7971	40.32	35	134	3345	53.25
				23	94	1920	51.15								
				33	208	5108	33.21								
				2	32	3708	13.11								
				1	12	4776	17.47								
				11	33	1731	69.59								
				8	64	1927	26.18								
				28	63	2529	92.62								
				14	149	8990	19.69								
				65	261	7385	52.06								
				121	379	3978	66.67								

C13 34				C14 60				C15 50				C16 50			
Zeta:	344.09	Zeta err.:	10.36	Zeta:	344.09	Zeta err.:	10.36	Zeta:	344.09	Zeta err.:	10.36	Zeta:	344.09	Zeta err.:	10.36
		RhoD:	1174909			RhoD:	1167091			RhoD:	1159273			RhoD:	1143636
		Nd:	5920.182			Nd:	5880.818			Nd:	5841.455			Nd:	5762.727
Ns	Ni	Area(μm^2)	Age (Ma)	Ns	Ni	Area(μm^2)	Age (Ma)	Ns	Ni	Area(μm^2)	Age (Ma)	Ns	Ni	Area (μm^2)	Age (Ma)
107	218	6155	98.05	3	32	6979	18.84	20	10	2144	387.27	38	146	3954	50.85
13	27	1762	96.2	25	69	3586	72.52	25	38	2159	129.98	2	88	6056	4.46
11	23	2024	95.56	34	98	2404	69.46	44	121	4877	72.17	10	66	2623	29.65
33	66	3704	99.87	71	275	6975	51.76	8	43	4439	37.02	1	12	2286	16.32
88	223	3379	78.95	4	28	2071	28.69	25	108	3706	46.03	5	16	2292	61
103	305	9876	67.62	21	47	2164	89.32	63	144	2390	86.73	28	85	2681	64.29
256	447	2933	114.26	9	17	3618	105.7	48	129	6597	73.83	1	33	4290	5.94
14	33	1664	84.84	45	152	4444	59.32	75	204	7388	72.96	1	52	3563	3.77
8	15	2280	106.47	3	58	4055	10.4	35	145	6789	47.99	23	43	2045	104.06
46	163	1952	56.56	52	121	3544	85.93	4	21	5142	37.9	40	143	3436	54.63
58	161	8023	72.11	11	46	2374	47.96	2	54	6862	7.39	1	14	4243	13.99
21	64	1727	65.71	1	25	6158	8.05	2	24	5405	16.61	7	38	2125	36.03
183	311	4920	117.37	76	184	8705	82.61	2	13	4890	30.63	25	83	1636	58.81
85	281	5329	60.6	11	41	1761	53.78	1	16	2562	12.46	2	17	3060	23.03
5	33	2320	30.43	32	51	2173	125.08	2	13	3723	30.63	28	101	2780	54.15
4	73	8128	11.02	43	151	4750	57.07	22	109	4680	40.16	21	98	2684	41.89
2	24	9367	16.75	13	35	2436	74.34	27	68	3345	78.76	9	5	2587	343.71
3	6	3828	99.87	26	123	6556	42.41	10	17	1772	116.34	2	6	3298	65.05
41	67	2045	122.02	6	7	3020	170.27	27	155	1606	34.67	23	195	4675	23.09
92	557	7930	33.16	20	54	1790	74.13	15	9	2867	324.32	1	11	3587	17.81
15	59	3330	50.97	50	228	3637	43.99	12	28	2353	84.97	11	38	4545	56.53
17	134	2506	25.49	19	59	4083	64.5	18	69	3321	51.85	2	8	4501	48.85
137	736	6383	37.36	32	34	1618	186.72	55	120	3250	90.83	20	70	2350	55.8
50	144	3268	69.52	9	20	2495	89.95	127	477	5748	52.92	19	73	2097	50.85
60	348	4636	34.61	10	33	2087	60.71	63	172	5722	72.69	63	166	2288	74.01
83	202	1727	82.18	37	58	2950	127.15	2	56	8670	7.12	3	4	1821	145.45
4	17	9408	47.19	6	40	2534	30.12	58	196	4488	58.79	1	8	4979	24.47
14	18	4030	154.69	15	48	4063	62.6	18	50	2530	71.45	45	124	5600	70.79
42	201	2751	41.92	12	15	6268	159.06	102	329	7104	61.58	14	39	3141	70.02
15	32	1628	93.67	1	19	2146	10.59	36	127	6250	56.32	19	28	3266	131.73
21	106	1937	39.76	28	58	3972	96.45	3	22	4730	27.16	8	36	4264	43.44
45	63	3157	142.2	19	41	1623	92.61	49	256	5196	38.09	10	23	2066	84.72
28	41	2457	136.02	14	18	3593	154.69	1	14	3306	14.24	24	105	3654	44.67
32	230	4824	27.95	12	32	4241	75.05	7	61	4929	22.86	28	59	1794	92.41
				40	43	2676	184.58	2	32	2912	12.46	28	116	4702	47.17
				13	40	3184	65.09	4	7	2687	113.04	5	23	5004	42.5
				12	14	2744	170.27	9	176	6022	10.2	20	61	1939	63.99
				11	19	1859	115.5	40	187	7021	42.55	6	45	2009	26.1
				13	33	4315	78.81	13	24	6678	107.21	13	36	1654	70.44
				45	136	2881	66.26	205	501	5071	81.15	2	55	3534	7.13
				13	41	4598	63.51	106	333	4775	63.22	10	28	2337	69.67
				28	149	3258	37.72	35	66	2377	104.97	4	9	1600	86.59
				70	581	2304	24.21	62	186	2366	66.18	3	43	5622	13.67
				1	9	5726	22.33	4	15	3467	53	16	83	2760	37.7
				48	164	2803	58.65	3	13	3787	45.89	2	6	1855	65.05
				7	63	1739	22.33	2	23	4042	17.33	9	33	2779	53.27
				20	15	2013	262.95	2	30	6272	13.29	16	32	2044	97.33
				38	110	6727	69.17	21	48	2580	86.73	1	6	2074	32.61
				17	45	2811	75.6	14	60	5426	46.4	2	11	2608	35.56
				46	139	2408	66.27	5	8	3771	123.54	14	49	2940	55.8
				3	55	8204	10.97								
				13	90	4592	29.01								
				54	151	4193	71.59								
				37	107	3331	69.23								
				14	96	3734	29.29								
				1	36	8221	5.59								
				14	52	2155	53.97								
				5	25	4119	40.13								
				5	53	4004	18.96								
				16	66	2558	48.61								

Data repository Chapter 4

1. Sample details

Name of the sample	Name of the cruise	Individual samples collected through the core
1	DF78-014	A49 A57 A63 A69 A74
2	NBP94-07-070	A260
3	NBP94-07-093	A268 A270
4	NBP94-01-027	A300 A301 A302
5	NBP94-07-078	A336 A337 A338 A339 A340
6	NBP94-07-079	A341 A343
7	NBP96-01-002	A350 A351 A352
8	NBP96-01-006	A353
9	DF62-01-005	A22
10	DF78-012	A84
11	DF76-001	A90
12	DF76-003	A111
13	NBP00-01-001	A208
14	NBP94-07-039	A259
15	NBP95-01-017	A313
16	NBP94-07-041	A323
17	NBP94-07-043	A324
18	NBP94-07-051	A330

2. Single grain AFT data

A49	35			A57	39			A63	45			A69	35		
Zeta:	344.09	Zeta err.:	10.36	Zeta:	344.09	Zeta err.:	10.36	Zeta:	344.09	Zeta err.:	10.36	Zeta:	344.09	Zeta err.:	10.36
		RhoD:	1397787			RhoD:	1389671			RhoD:	1381555			RhoD:	1365322
		Nd:	5663.029			Nd:	5622.059			Nd:	5581.088			Nd:	5499.147
Ns	Ni	Area(μm^2)	Age (Ma)	Ns	Ni	Area(μm^2)	Age (Ma)	Ns	Ni	Area(μm^2)	Age (Ma)	Ns	Ni	Area(μm^2)	Age (Ma)
256	116	3257	510.78	43	30	1607	333.97	127	45	1972	637.47	20	16	3862	288.09
47	46	2185	241.52	116	111	5414	245.19	63	117	1915	126.59	112	145	3515	179.54
55	39	2126	331.03	40	23	2104	403.03	95	132	2320	168.65	31	42	2734	171.66
15	14	1757	253.04	90	103	3716	205.64	15	20	4072	175.65	24	38	1719	147.17
68	93	1676	173.75	16	41	2492	92.65	14	19	1686	172.61	38	55	1789	160.83
98	118	5310	197	37	40	2385	217.5	16	29	1622	129.68	48	116	3232	96.8
10	19	1966	125.54	3	4	2261	176.91	35	48	2335	170.84	24	20	2226	276.81
60	145	3241	98.9	74	102	2155	171.2	23	36	1615	149.93	10	24	1899	97.47
45	55	2113	194.12	46	143	5127	76.47	72	79	1706	212.83	44	58	1989	176.37
56	70	2819	189.87	101	111	1763	214.01	34	75	1853	106.74	12	23	2327	121.82
26	53	4386	117.09	46	126	2985	86.72	39	32	1865	283.05	51	80	3255	148.54
45	57	1687	187.4	9	40	2553	53.58	46	151	3968	71.92	81	75	3528	249.66
42	77	2552	130.06	73	107	4024	161.12	48	43	1608	259.73	184	368	3021	116.79
55	86	3490	152.23	63	109	4860	136.76	45	110	2787	96.4	108	191	1855	131.92
92	292	1619	75.45	91	63	1642	336.49	22	14	2526	362.69	67	138	3316	113.43
30	38	2617	187.4	23	23	1763	234.81	96	231	2313	97.92	69	116	2039	138.7
48	37	2106	305.13	240	278	2231	203.22	19	37	1823	120.78	18	23	1621	181.87
8	3	2206	612.28	75	161	2594	110.45	23	56	1674	96.78	60	47	1603	294.08
22	26	2080	200.65	71	182	4092	92.62	13	28	2011	109.3	9	21	2027	100.23
122	156	2464	185.67	5	24	4312	49.63	23	49	1627	110.49	78	145	2779	125.56
31	43	1637	171.35	19	27	3090	166.13	132	195	2254	158.75	67	116	1781	134.72
69	63	3922	258.55	2	3	2701	157.49	48	46	2295	243.1	21	75	2849	65.66
52	58	1859	212.41	67	161	1732	98.76	30	79	2443	89.54	44	31	1857	326.15
192	296	3150	154.37	18	41	3930	104.14	63	69	2186	213.21	93	177	1630	122.67
28	29	1614	228.46	21	18	2227	273.13	32	20	2067	369.1	146	209	4071	162.59
53	97	1800	130.28	17	40	1861	100.84	20	43	2172	109.49	8	14	2399	133.3
68	117	2081	138.49	83	133	2788	147.54	42	47	1621	208.75	87	85	3100	236.84
66	154	2974	102.41	71	158	3393	106.58	17	21	1647	189.39	43	71	4319	141.19
29	63	2066	109.93	11	34	1617	76.91	119	106	3326	261.18	312	147	5374	481.8
115	75	1684	359.13	60	63	3739	223.82	31	56	2056	130.11	14	13	2508	248.96
98	352	4219	66.71	26	38	3664	161.58	42	65	1706	151.61	98	232	1930	98.8
86	45	3112	444.62	9	4	1959	516.79	57	96	1852	139.45	59	68	5696	201.33
23	38	2167	144.16	10	26	1606	91.33	13	29	2331	105.56	58	68	1630	197.97
41	132	2303	74.38	14	38	2360	87.51	40	47	2632	198.96	217	303	3447	166.63
14	49	1977	68.45	48	31	2808	360.04	4	3	3230	309.04	87	92	2379	219.12
				10	27	1644	87.97	45	139	1794	76.41				
				30	136	2715	52.54	3	3	1649	233.15				
				26	31	2553	197.51	109	168	1745	152.23				
				3	6	2504	118.48	40	30	2841	309.04				
								39	34	1850	266.74				
								20	42	2660	112.08				
								55	95	2906	136.01				
								63	187	1735	79.49				
								36	45	1897	187.19				
								133	130	2846	238.44				

A74	35			A260	22			A268	23			A270	40		
Zeta:	344.09	Zeta err.:	10.36	Zeta:	344.09	Zeta err.:	10.36	Zeta:	344.09	Zeta err.:	10.36	Zeta:	344.09	Zeta err.:	10.36
		RhoD:	1375062			RhoD:	1332858			RhoD:	1324741			RhoD:	1316625
		Nd:	5548.312			Nd:	5335.265			Nd:	5294.294			Nd:	5253.324
Ns	Ni	Area(μm^2)	Age (Ma)	Ns	Ni	Area(μm^2)	Age (Ma)	Ns	Ni	Area(μm^2)	Age (Ma)	Ns	Ni	Area(μm^2)	Age (Ma)
44	28	1731	355.02	306	319	2069	215.84	15	24	1939	140.4	32	85	3523	84.93
74	48	4651	348.48	218	302	3188	163.09	26	86	2482	68.29	10	34	1732	66.45
47	51	3473	210.57	17	23	2075	166.95	8	43	1777	42.11	45	116	1884	87.5
17	5	1977	744.94	22	35	2426	142.25	14	28	3871	112.56	2	30	1641	15.12
45	115	1669	90.25	139	232	5254	135.66	69	263	3102	59.31	2	88	2460	5.16
107	97	2920	251.24	32	149	4274	48.96	91	209	4201	98.13	15	19	1643	176.84
61	59	1848	235.77	31	12	3415	565.57	27	42	2106	144.36	64	152	2283	94.92
15	27	4351	127.76	125	254	5399	111.64	49	121	3863	91.32	5	77	1845	14.73
62	72	3000	196.96	60	100	5279	135.85	10	6	1857	367.8	93	139	2415	150.18
24	37	2521	148.92	7	24	4469	66.4	8	24	2302	75.26	8	16	1685	112.56
59	113	3838	120.14	12	94	4359	29.15	9	7	1632	285.57	18	36	4637	112.56
18	33	1856	125.46	6	42	3890	32.61	71	211	2800	75.97	68	87	3029	175.1
131	115	3104	259.29	59	72	4639	184.83	19	84	2737	51.16	26	65	3109	90.21
69	112	1670	141.52	39	289	6742	30.81	16	21	1903	170.75	85	524	3763	36.73
349	396	3971	201.51	43	56	3363	173.35	26	65	2139	90.21	19	53	2434	80.9
21	19	2155	251.73	103	189	6718	123.51	13	84	4207	35.05	1	8	1639	28.33
54	33	1895	369.28	16	81	5546	45.04	32	176	1846	41.16	1	34	1646	6.68
22	16	2261	311.7	233	349	5509	150.98	66	75	3524	196.81	5	95	2698	11.94
35	58	3356	138.66	65	25	6561	569.06	31	122	3933	57.45	14	15	3070	208.55
168	130	1943	293.37	52	72	4478	163.18	10	40	1941	56.53	19	91	1937	47.24
35	69	2835	116.75	61	295	9485	47.14	27	68	2422	89.55	101	299	5553	76.26
141	165	4820	195.48	19	13	3283	326.04	23	25	2386	205.62	24	55	3572	98.34
28	96	1851	67.39					7	30	3029	52.77	29	89	2153	73.58
29	68	1621	98.3									13	40	2765	73.39
8	4	1734	448.55									19	46	1608	93.13
112	296	3362	87.29									11	43	2142	57.83
13	12	6187	246.83									15	36	3744	93.94
105	244	2206	99.18									3	193	3938	3.53
8	10	2566	183.18									6	106	2263	12.84
21	53	3380	91.38									5	29	3445	39.04
29	30	2182	220.7									31	170	2205	41.28
50	28	1602	401.96									1	85	2183	2.67
10	15	2185	153.01									17	105	2987	36.66
187	216	1867	198.01									34	184	3211	41.83
26	90	2461	66.75									54	134	1746	90.87
												52	212	3844	55.46
												143	296	2917	108.79
												80	154	4090	116.91
												5	25	1923	45.26
												2	8	2190	56.53

A300	40			A301	40			A302	40			A336	40		
Zeta:	344.09	Zeta err.:	10.36	Zeta:	344.09	Zeta err.:	10.36	Zeta:	344.09	Zeta err.:	10.36	Zeta:	344.09	Zeta err.:	10.36
		RhoD:	1308509			RhoD:	1284160			RhoD:	1259812			RhoD:	1243579
		Nd:	5212.353			Nd:	5089.441			Nd:	4966.529			Nd:	4884.588
Ns	Ni	Area(μm^2)	Age (Ma)	Ns	Ni	Area(μm^2)	Age (Ma)	Ns	Ni	Area(μm^2)	Age (Ma)	Ns	Ni	Area(μm^2)	Age (Ma)
11	14	1810	174.69	12	37	2584	71.03	24	49	1917	105.31	22	85	5897	54.98
5	35	2331	32.12	215	188	1911	247.05	42	20	3218	439.88	11	30	3164	77.75
43	118	2867	81.61	12	14	1795	186.05	40	75	2149	114.59	45	87	5111	109.41
92	304	2709	67.85	78	148	4300	115.03	42	44	2467	203.67	16	28	4013	120.77
28	161	2170	39.08	13	25	2316	113.51	7	8	4050	186.94	26	61	2223	90.29
29	194	2294	33.6	158	41	2903	797.25	22	63	1698	75.26	39	215	2377	38.58
36	155	2584	52.13	13	10	2095	280.11	163	359	3334	97.68	14	22	3683	134.35
9	10	3382	199.72	146	124	2639	254.21	17	36	3214	101.56	53	513	6431	22
40	124	3119	72.3	36	86	1801	91.53	14	37	2669	81.51	36	122	3991	62.65
34	180	3176	42.43	11	35	3237	68.84	133	166	1938	171.38	19	61	1617	66.11
18	28	2838	143.28	37	25	3996	317.95	248	141	2521	370.43	2	4	1602	105.8
17	30	1837	126.47	4	47	2349	18.71	48	68	1798	151.23	23	129	4811	37.92
42	38	1891	244.41	144	58	2427	524.79	17	76	2380	48.31	29	61	5480	100.63
25	41	2156	135.98	39	40	2356	211.21	10	35	2129	61.64	543	453	5590	250.78
12	46	2025	58.53	41	130	2209	69.08	52	198	5771	56.68	27	128	6618	44.84
1	6	1602	37.45	30	142	2577	46.36	15	16	1612	200.09	59	99	2539	125.9
25	25	2550	221.53	59	74	2155	173.23	9	33	2808	58.85	58	84	3235	145.65
17	43	5113	88.49	236	341	2860	150.63	131	243	4559	115.82	1	16	2530	13.32
12	6	1760	435.7	26	43	1779	131.8	95	219	4725	93.36	14	24	2803	123.26
23	79	3217	65.28	5	5	2054	216.54	35	185	2979	40.88	8	6	3808	278.35
12	21	2520	127.52	9	52	2929	38	31	86	3491	77.67	58	131	2606	93.77
58	86	2586	150.24	46	126	1733	79.9	75	162	2859	99.59	265	343	2060	162.75
8	37	2208	48.55	28	25	2495	242.04	25	137	6220	39.44	60	152	3905	83.67
45	196	2271	51.54	26	27	1612	208.65	26	274	2752	20.54	22	43	2543	108.23
29	171	2272	38.11	141	165	2323	185.49	18	123	2916	31.65	31	32	4558	203.43
15	100	1643	33.72	48	150	4684	70.09	39	116	3417	72.47	58	166	5327	74.11
166	380	3654	97.71	6	31	3218	42.48	8	35	3100	49.36	33	27	1844	255.61
39	77	2663	113.15	37	65	2623	124.15	47	86	1875	117.4	35	98	1951	75.74
47	26	2280	395.06	20	30	2287	145.16	42	256	3021	35.47	38	124	4259	65.05
22	42	1669	116.99	12	5	2761	507.97	7	32	2651	47.25	28	76	3741	78.12
32	41	2244	173.55	69	141	4110	106.88	17	89	3408	41.27	24	72	5455	70.72
42	123	2686	76.5	124	234	2509	115.65	26	188	4339	29.91	19	25	5414	160.13
22	37	2366	132.64	12	15	1987	173.81	15	32	3128	100.82	66	90	3737	154.58
17	29	3678	130.78	3	18	1685	36.6	126	239	2562	113.28	112	183	2211	129.26
25	211	3356	26.65	34	102	1824	72.99	6	17	1891	76.06	4	17	2204	50
13	67	2566	43.58	96	100	3556	208.02	56	222	8221	54.45	58	131	2490	93.77
136	128	1605	235.12	9	59	1883	33.51	37	102	1913	78.16	81	372	3080	46.29
99	83	2085	263.37	245	436	2304	122.57	14	73	2532	41.44	45	117	3718	81.53
49	215	2161	51.16	87	188	5103	101.11	9	33	2230	58.85	16	30	3436	112.79
17	36	1853	105.56	6	35	1775	37.64	60	151	5464	85.57	18	108	3302	35.46

A337	40			A338	38			A339	40			A340	40		
Zeta:	344.09	Zeta err.:	10.36	Zeta:	344.09	Zeta err.:	10.36	Zeta:	344.09	Zeta err.:	10.36	Zeta:	344.09	Zeta err.:	10.36
		RhoD:	1235463			RhoD:	1227347			RhoD:	1219231			RhoD:	1202998
		Nd:	4843.618			Nd:	4802.647			Nd:	4761.676			Nd:	4679.737
Ns	Ni	Area(μm^2)	Age (Ma)	Ns	Ni	Area(μm^2)	Age (Ma)	Ns	Ni	Area(μm^2)	Age (Ma)	Ns	Ni	Area(μm^2)	Age (Ma)
55	112	2804	103.92	108	55	7198	402.69	76	137	5155	115.4	39	90	1725	88.85
14	60	2291	49.59	81	230	4064	74.1	45	39	2116	237.75	38	166	3400	47.09
16	17	1928	197.72	63	66	3293	198.9	91	117	3420	161.22	6	28	1608	44.09
7	4	1997	362.93	73	146	2370	104.95	19	35	3387	112.95	14	9	1879	313.41
162	422	3473	81.38	61	165	5292	77.76	28	43	4546	135.25	61	291	3915	43.13
14	31	2347	95.63	12	51	2454	49.6	16	58	1637	57.64	75	113	5708	135.59
57	85	3228	141.5	23	26	3913	184.53	269	296	4532	187.98	7	25	2545	57.55
13	112	1603	24.71	9	18	1801	104.95	16	53	2283	63.06	19	28	2045	138.59
33	593	2271	11.86	598	448	9506	276.46	110	146	2915	156.23	37	16	3438	460.57
5	8	1699	131.97	276	183	4134	311.51	87	183	3671	99.02	20	28	3013	145.81
86	201	4404	90.64	31	72	2733	90.47	2	2	2377	206.55	8	61	4896	27.02
12	41	2239	62.14	40	67	2156	125.12	8	10	4089	165.77	17	73	1616	47.9
110	187	1729	124.29	6	69	1701	18.38	24	57	2536	87.78	31	58	1898	109.41
9	22	1800	86.69	44	45	2380	203.66	21	81	3364	54.19	26	17	1709	308.26
19	29	2410	138.28	62	21	4281	596.32	33	22	2237	307.4	19	32	2627	121.43
5	13	2528	81.53	106	155	3902	143.12	146	267	2081	113.76	40	114	3502	72.04
12	44	2347	57.92	5	15	1923	70.16	1	6	1952	34.89	27	64	2218	86.51
17	90	1765	40.17	35	84	2211	87.58	5	15	1758	69.59	26	48	1681	110.87
59	194	2003	64.56	9	25	3588	75.73	27	23	3364	241.81	3	35	2925	17.67
3	10	1875	63.69	45	137	4780	69.14	2	4	1730	104.1	81	182	3344	91.23
35	37	2268	198.71	10	20	3577	104.95	25	67	2268	77.85	21	245	2233	17.67
33	141	3257	49.74	46	173	4232	56.02	12	15	1722	165.77	148	194	7578	155.61
31	98	2348	67.13	30	49	3407	128.28	16	25	2518	132.95	20	16	2507	253.04
39	75	3159	109.99	27	56	2011	101.23	91	528	6430	36.07	27	11	2862	487.82
26	53	3479	103.81	89	143	1769	130.38	123	248	3217	103.27	79	133	3639	121.48
14	45	3347	66.03	8	22	3451	76.5	8	40	1844	41.84	31	134	2013	47.59
38	116	3268	69.51	101	140	4231	150.89	39	222	3141	36.77	18	116	3000	31.96
25	75	1613	70.72	216	103	2507	429.17	30	69	2087	90.62	79	51	5423	312.12
23	40	2722	121.52	225	87	2690	525.29	26	203	2260	26.83	58	309	7694	38.64
48	107	3205	95	23	88	2748	55.07	18	43	2003	87.27	11	57	2360	39.72
10	40	2867	53.11	56	271	3462	43.58	18	67	3282	56.14	25	118	4581	43.59
21	87	2412	51.29	38	43	2455	184.35	89	63	2540	289.9	55	280	1815	40.43
68	92	6989	155.79	20	45	4517	93.37	72	413	5277	36.49	8	20	2118	82.06
28	63	2557	94.13	19	51	2501	78.36	2	32	1894	13.11	26	44	1979	120.86
108	91	2326	248.34	27	37	1894	152.6	7	11	3015	132.2	27	60	1816	92.24
78	240	4295	68.96	22	21	3563	217.97	36	74	7293	101.31	26	202	1647	26.52
4	59	3212	14.45	188	201	2525	194.95	8	27	2630	61.89	34	109	3559	64.08
131	320	2910	86.75	37	37	1823	208.22	12	61	1895	41.16	147	237	4591	126.8
21	49	3892	90.79					48	87	3998	114.78	30	263	5395	23.51
72	123	1991	123.69					80	212	4407	78.72	22	32	3887	140.4

A341 37	37			A343	20			A350	35			A351	34		
Zeta:	344.09	Zeta err.:	10.36	Zeta:	344.09	Zeta err.:	10.36	Zeta:	344.09	Zeta err.:	10.36	Zeta:	344.09	Zeta err.:	10.36
		RhoD:	1178650			RhoD:	1170533			RhoD:	1162417			RhoD:	1154301
		Nd:	4556.824			Nd:	4515.853			Nd:	4474.882			Nd:	4433.912
Ns	Ni	Area(μm^2)	Age (Ma)	Ns	Ni	Area(μm^2)	Age (Ma)	Ns	Ni	Area(μm^2)	Age (Ma)	Ns	Ni	Area(μm^2)	Age (Ma)
35	61	2084	115.44	11	48	3313	45.97	8	54	2926	29.5	15	30	1731	98.17
121	283	3809	86.22	12	12	1671	198.21	226	122	3289	359.49	59	102	1859	113.44
3	7	2621	86.42	53	52	3280	201.97	5	18	3134	55.2	29	32	1793	176.85
24	138	2999	35.21	29	94	4558	61.8	60	104	2810	114.12	47	119	4271	77.67
15	13	2085	230.09	16	22	2164	144.76	54	50	3012	212.01	76	210	3638	71.21
5	14	3192	72.1	14	32	3338	87.47	10	22	1773	90.08	11	78	2206	27.84
10	12	2420	167	10	17	2660	117.33	14	76	3557	36.66	214	187	2838	222.53
20	22	3342	181.96	26	40	2222	129.53	18	31	2258	114.85	47	118	2344	78.33
29	66	5750	88.59	9	134	1606	13.51	38	121	3077	62.37	43	67	4067	125.75
2	14	2047	28.94	37	59	3318	125.01	9	61	2471	29.38	5	75	3733	13.18
35	58	2436	121.36	4	33	1841	24.35	30	50	2598	118.64	6	14	2045	84.24
34	79	2670	86.79	13	20	2938	129.53	24	38	3315	124.83	18	13	3130	268.29
9	14	3332	129.2	50	91	2712	109.66	22	68	4811	64.25	23	51	2705	88.62
9	36	1736	50.55	28	231	2877	24.35	57	162	3330	69.84	6	15	2260	78.66
21	68	1612	62.39	347	236	2364	289.38	11	64	2479	34.21	19	75	2406	49.93
42	72	3464	117.35	12	17	1673	140.55	12	33	2343	72.17	114	227	3401	98.6
3	14	4092	43.36	129	341	3866	75.7	8	23	1634	69.05	69	155	2668	87.48
24	119	2652	40.81	5	14	2515	71.49	4	23	2672	34.62	43	144	3739	58.81
8	27	2841	59.87	32	50	1977	127.56	16	56	2068	56.77	69	166	3813	81.72
25	134	6701	37.76	28	158	1896	35.57	14	13	2308	211.42	116	199	4394	114.31
31	164	6254	38.26					13	78	3637	33.18	14	52	5994	53.05
16	27	2796	119.2					55	75	2260	144.72	75	29	4264	492.39
83	113	4534	147.42					15	46	1676	64.75	123	389	5447	62.26
6	29	5177	41.87					24	73	4219	65.28	18	42	2992	84.24
24	28	2023	171.7					52	86	1850	119.56	312	329	3371	184.95
38	202	5084	38.08					12	20	3075	118.64	16	36	1625	87.34
9	36	4575	50.55					4	9	3315	88.09	73	167	4772	85.91
18	57	2265	63.79					52	49	1872	208.39	12	83	2345	28.54
39	60	3850	130.63					19	27	2849	138.93	15	48	2304	61.53
164	214	5627	153.73					59	147	4031	79.61	35	81	2857	84.93
19	157	3334	24.52					21	15	3660	273.52	31	58	2039	104.89
132	267	4961	99.59					270	345	2020	154.32	58	104	3178	109.41
37	60	4109	123.99					12	82	2170	29.14	30	94	3473	62.84
61	75	4796	163.04					30	90	3189	66.18	36	37	3423	189.69
205	318	3412	129.56					58	148	4697	77.74				
5	34	1611	29.79												
18	85	3463	42.85												

A352	28			A353	17			A22	40			A84	40		
Zeta:	344.09	Zeta err.:	10.36	Zeta:	344.09	Zeta err.:	10.36	Zeta:	344.94	Zeta err.:	27.24	Zeta:	344.94	Zeta err.:	27.24
		RhoD:	1146185			RhoD:	1138069			RhoD:	$9.92*10^6$			RhoD:	$9.62*10^6$
		Nd:	4392.941			Nd:	4351.971			Nd:	4798			Nd:	4798
Ns	Ni	Area(μm²)	Age (Ma)	Ns	Ni	Area(μm²)	Age (Ma)	Ns	Ni	Area(μm²)	Age (Ma)	Ns	Ni	Area(μm²)	Age (Ma)
42	160	3633	51.73	17	27	1886	122.32	11	62	2627	30.28	19	22	2672	141.72
26	86	3651	59.54	5	17	2872	57.43	44	30	1804	246.17	41	63	1810	107.08
3	3	1674	194.88	157	286	4719	106.78	17	36	1271	80.29	44	141	1950	51.57
15	60	1687	49.27	64	78	3189	158.95	25	41	1221	103.49	20	38	2237	86.74
184	235	3932	153.08	9	33	1965	53.27	32	34	1329	159.05	54	82	1927	108.35
45	56	3617	157.06	51	89	2496	111.42	26	99	4297	44.78	25	65	1924	63.5
8	57	1640	27.71	132	187	6573	136.98	2	48	1919	7.12	21	22	1415	156.46
3	15	2229	39.45	284	275	5600	199.43	8	192	2101	7.12	36	74	2924	80.21
13	8	1658	313.75	38	43	2681	171.04	6	20	1888	51.12	120	276	5253	71.74
32	68	2246	92.44	5	37	3278	26.45	14	60	3195	39.8	3	28	3347	17.75
15	16	1609	182.87	15	44	1685	66.52	4	33	1616	20.7	17	21	1540	132.93
7	35	1600	39.45	22	16	3136	264.19	1	76	3408	2.25	114	121	3108	154.45
165	118	2450	270.89	11	5	2664	417.66	10	60	2516	28.45	25	60	1265	68.76
9	19	1739	93.04	140	123	5204	219.46	5	13	3140	65.47	11	23	1219	78.87
2	10	2039	39.45	47	42	1798	215.83	9	23	2155	66.6	34	67	1049	83.65
76	113	3426	131.71	13	32	2092	79.19	32	82	2793	66.42	9	26	1416	57.18
32	42	2325	149.01	29	16	6067	346.03	11	39	3069	48.08	23	56	1736	67.79
4	4	1864	194.88					12	45	2006	45.46	25	19	1847	214.7
21	22	2832	186.14					18	33	1913	92.65	16	53	1942	49.89
23	18	1777	247.98					21	53	3417	67.44	47	88	2759	88.01
23	17	1603	262.27					51	108	1738	80.29	35	95	2370	60.84
3	6	1680	98.17					9	26	2067	58.95	24	35	1545	112.78
19	20	1600	185.27					21	57	1868	62.73	18	22	2281	134.34
3	16	1736	36.99					9	10	1508	152.17	11	19	2053	95.35
25	33	2109	148.17					17	37	2260	78.13	15	21	1778	117.44
4	21	3861	37.58					11	73	3379	25.73	10	6	3433	270.76
24	34	2378	138.17					3	9	1807	56.78	72	110	2815	107.7
7	19	1617	72.48					13	90	2542	24.67	39	64	1875	100.32
								15	87	4004	29.43	14	37	2151	62.48
								26	54	1677	81.85	47	124	2183	62.58
								3	29	4423	17.67	20	71	1965	46.57
								3	14	1466	36.56	80	189	3618	69.85
								25	73	3167	58.33	46	101	2496	75.13
								6	56	2401	18.31	149	269	4952	91.25
								10	45	3474	37.91	98	301	5278	53.79
								36	52	4066	117.37	18	71	4290	41.93
								30	34	3243	149.22	65	96	2544	111.37
								28	163	4367	29.32	16	30	1133	87.89
								56	66	2787	143.56	19	60	1714	52.33
								21	50	3397	71.46	22	87	2126	41.82

A90	36			A111	40			A208	40			A259	42		
Zeta:	344.94	Zeta err.:	27.24	Zeta:	344.94	Zeta err.:	27.24	Zeta:	344.94	Zeta err.:	27.24	Zeta:	344.94	Zeta err.:	27.24
		RhoD:	$9.58*10^6$			RhoD:	$9.58*10^6$			RhoD:	$9.3*10^6$			RhoD:	$9.12*10^6$
		Nd:	4798			Nd:	4798			Nd:	4798			Nd:	4798
Ns	Ni	Area(μm²)	Age (Ma)	Ns	Ni	Area(μm²)	Age (Ma)	Ns	Ni	Area(μm²)	Age (Ma)	Ns	Ni	Area(μm²)	Age (Ma)
11	53	1497	34.2	35	62	1361	92.6	18	28	3523	102.3	75	198	4452	59.31
10	45	2140	36.61	2	24	1658	13.75	19	33	2699	91.69	12	25	2474	75.06
7	58	2222	19.91	11	10	1488	179.23	73	193	7320	60.38	5	14	1687	55.93
2	7	1913	47.04	24	94	1171	42.05	8	20	2224	63.84	10	28	1627	55.93
7	29	2245	39.76	49	82	1233	97.98	11	20	2957	87.62	29	62	1913	73.16
2	13	2643	25.37	33	56	2032	96.64	18	22	2142	129.92	19	57	2933	52.22
43	118	5682	59.93	13	23	2026	92.72	44	42	3035	165.88	19	63	3309	47.26
10	70	2825	23.56	1	3	4260	54.84	21	29	3798	115.12	10	8	3067	193.68
116	148	2593	128.22	77	203	2878	62.37	30	35	2593	136.04	9	17	2769	82.74
18	53	2723	55.87	25	20	3363	203.29	35	26	2216	212.38	8	46	3351	27.3
8	20	2349	65.75	8	26	2151	50.64	61	67	2839	144.4	7	17	1922	64.44
33	86	2784	63.09	13	38	2206	56.28	17	32	4219	84.65	17	35	2337	75.95
57	97	1505	96.37	20	60	2302	54.84	30	56	1373	85.36	11	24	3571	71.69
25	134	2661	30.75	15	32	1533	76.99	43	39	1926	174.47	15	16	1523	145.8
3	16	2556	30.91	10	13	2332	125.86	18	16	1897	177.97	4	19	2497	33.03
9	27	3254	54.84	176	306	9024	94.34	22	39	2593	89.85	13	49	1841	41.6
57	126	5785	74.32	60	179	5056	55.15	20	31	1663	102.66	7	15	1749	72.99
7	29	2859	39.76	24	55	1507	71.7	38	40	3872	150.6	8	21	2697	59.64
84	135	2313	102	7	16	1425	71.88	35	36	3937	154.09	3	5	1357	93.69
46	48	2176	156.43	27	54	2435	82.09	18	41	1870	70.04	19	46	1792	64.64
24	177	1432	22.36	113	123	4503	150.03	6	40	1551	24.01	24	61	1689	61.59
22	7	3109	499.43	63	75	4200	137.32	55	78	2054	112.12	20	42	1923	74.47
13	125	3090	17.16	9	16	1603	92.28	37	90	2919	65.61	13	34	1896	59.86
11	37	2693	48.94	24	21	2182	186.12	28	44	3067	101.27	28	10	3323	426.03
24	47	2776	83.82	51	21	1502	389.27	14	30	2360	74.42	9	21	1324	67.06
12	26	2021	75.81	25	43	1916	95.35	49	98	3402	79.7	6	18	1524	52.22
1	23	2230	7.18	43	74	2229	95.3	2	3	3522	106.05	7	22	3097	49.85
28	24	2673	189.94	9	18	1571	82.09	4	63	3058	10.18	2	7	3582	44.78
21	51	1798	67.68	74	138	4682	88	9	13	2380	110.1	20	38	2940	82.26
5	13	1567	63.24	138	267	7964	84.84	19	85	2088	35.75	66	143	2983	72.19
5	29	1982	28.42	6	24	2250	41.17	58	60	2466	153.22	12	43	3226	43.75
42	221	2921	31.32	19	17	3007	182.07	39	40	2399	154.52	17	58	2944	45.94
4	13	4029	50.64	44	132	2353	54.84	19	64	1608	47.44	10	16	2011	97.57
32	73	4016	72.02	28	85	2518	54.2	33	41	1807	127.82	34	39	2746	135.69
64	154	2211	68.3	6	15	2972	65.75	28	69	5853	64.76	15	25	2923	93.69
19	57	1276	54.84	40	46	1478	142.1	13	21	3063	98.54	5	5	5020	155.4
				11	17	1895	106.03	20	30	2103	106.05	18	32	1870	87.88
				58	124	2391	76.82	42	116	2960	57.81	11	104	3158	16.62
				20	46	1860	71.44	8	21	1668	60.82	11	16	2112	107.24
				16	37	2176	71.06	17	61	1437	44.55	28	54	2823	81.05
												19	24	2427	123.34
												47	74	4332	99.14

A313	40			A323	20			A324	40			A330	30		
Zeta:	344.94	Zeta err.:	27.24	Zeta:	344.94	Zeta err.:	27.24	Zeta:	344.94	Zeta err.:	27.24	Zeta:	344.94	Zeta err.:	27.24
		RhoD:	$9.06*10^6$			RhoD:	$11.39*10^6$			RhoD:	$11.32*10^6$			RhoD:	$11.25*10^6$
		Nd:	4798			Nd:	4798			Nd:	4798			Nd:	4798
Ns	Ni	Area(μm^2)	Age (Ma)	Ns	Ni	Area(μm^2)	Age (Ma)	Ns	Ni	Area(μm^2)	Age (Ma)	Ns	Ni	Area(μm^2)	Age (Ma)
62	160	2156	60.27	25	37	2494	131.38	21	82	2942	49.81	89	186	2063	92.18
28	84	4235	51.88	11	72	5177	29.94	10	31	4361	62.67	22	64	4235	66.35
57	156	4006	56.84	106	121	3689	169.83	241	276	2896	168.26	35	119	3387	56.82
46	93	3721	76.83	64	160	3761	78.1	24	51	2719	91.23	33	71	4523	89.56
11	84	3112	20.43	30	49	2325	119.16	27	34	2413	153.21	5	16	2087	60.35
220	427	7285	80.01	20	33	2530	117.97	27	35	1512	148.88	107	151	5538	136.04
23	17	2339	208.02	27	49	1783	107.35	9	26	4980	67.23	123	178	2456	132.7
104	54	2646	294.13	64	115	2526	108.41	75	141	4627	103.02	98	150	4539	125.54
14	40	1538	54.46	76	100	1799	147.59	127	161	4050	152.2	23	64	4246	69.35
29	104	4061	43.43	12	32	4310	73.25	26	58	4440	86.93	405	575	8165	135.24
21	67	1536	48.79	26	42	3734	120.47	21	43	2286	94.65	32	131	5904	47.22
118	222	3514	82.53	12	65	2926	36.16	8	14	5756	110.61	7	19	2522	71.09
77	204	5379	58.71	55	126	3024	85.18	19	35	3314	105.12	62	130	2536	91.88
8	42	3375	29.69	60	106	3129	110.25	18	63	6433	55.54	80	114	2257	134.74
32	89	1909	55.94	9	32	2644	55.01	46	80	2393	111.29	46	53	1602	166.24
34	88	2307	60.09	34	76	3332	87.29	10	36	2717	54.01	168	156	3963	205.64
22	25	3514	136.06	4	6	1671	129.65	15	29	3411	100.2	36	45	2894	153.38
17	26	5535	101.37	67	75	2005	173.14	23	66	1895	67.68	157	192	548	156.74
72	107	3527	104.3	58	105	4504	107.61	38	90	2809	81.91	49	68	2446	138.32
49	98	5424	77.66	31	70	1340	86.41	23	70	1737	63.83	141	155	3815	174.13
18	25	1398	111.54					28	89	7279	61.13	178	309	6686	110.81
60	101	3490	92.16					83	94	3550	170.12	3	4	1921	143.9
82	214	2746	59.6					144	208	2717	133.77	80	85	2483	180.08
2	7	2424	44.49					5	5	2592	192.34	220	312	9143	135.38
44	29	1965	232.83					17	19	4498	172.36	19	27	2555	135.11
123	100	5487	189.39					45	85	3757	102.54	75	106	5091	135.84
32	136	1953	36.66					86	196	3329	85.1	32	64	3353	96.29
33	54	2922	94.79					145	223	4182	125.71	124	286	2351	83.58
80	154	2157	80.67					85	176	2747	93.61	22	65	4106	65.34
146	279	5640	81.26					15	84	4178	34.77	45	75	1887	115.38
65	90	2589	111.88					74	81	2085	175.94				
73	148	2021	76.62					50	65	3375	148.46				
20	26	4155	119.09					31	31	3517	192.34				
77	118	3048	101.17					14	29	3761	93.57				
20	67	3978	46.48					92	130	4340	136.71				
38	81	4964	72.89					52	110	2455	91.64				
31	161	5148	30.02					17	54	2038	61.17				
19	64	2099	46.22					13	22	3875	114.35				
28	152	3859	28.72					9	103	3354	17.04				
82	220	4250	57.98					238	352	7973	130.67				

3. Length measurements and AFT modeling

1	P4 （84-100Ma）	1	P5 (112-190Ma)	1	P7 (>270Ma)	4	P6 (222-270Ma)
length (um)	angle (°)	length (um)	angle(°)	length (um)	angle(°)	length (um)	angle(°)
9.83	62.58	11.01	2	11.57	84.58	9.77	0
10.97	54.35	15.13	48.67	11.2	5	9.6	24.91
10.21	62.18	15.76	87.03	12.41	86.6	11.72	29.71
13.02	43.07	9.46	54.39	10.84	27.79	9.82	38.34
13.84	7.02	10	7.21	10.52	78.62	12.91	0
13.22	84.23	12.57	89.11	13.05	7.99	9.76	66.92
10.21	45	9.83	69.89	13.57	62.32	11.41	66.49
10.87	85.76	12.69	2	12.13	62.73	9.57	60.82
14.67	41.72	13.68	13.87	14.3	84.78	13.99	84.73
10.27	8.87	14.29	54.02	10.52	69.23	12.88	54.64
10.1	89.94	10.96	61.44	14.14	75.19	11.56	86.24
12.75	56.19	12.85	54.26	14.57	58.76	14.59	20.78
13.48	4.97	14.31	59.43	13.58	7.04	11.38	43.57
12.58	12.34	9.45	1	11.95	26.13	11.48	36.63
13.12	21.62	10.64	89.47	15.84	84.58	14.35	27.16
14.03	47.61	10.93	65.17	13.26	66.99	15.23	40.83
12.18	79.19	12.33	20.89	12.14	9.73	10.22	60.37
15.75	20.37	14.25	76.3	14.4	8.34	10.48	82.43
13.35	34.18	14.67	83.14	14.6	52.16	11.09	31.61
10.75	55.64	13.81	73.42	10.81	89.05	15.22	12.35
13.74	0	15.26	59.56	12.49	39.3	12.53	70.63
13.47	74.52	14.84	77.3	11.83	76.54	13.7	27.24
9.31	11.64	15.07	84.74	9.6	68.44	12.63	13.52
8.75	85.03	13.35	75.4	9.48	75.94	14.19	63.16
9.81	45.66	11.92	72.76	9.24	21.61	12.87	8.71
9.48	76.71	14.1	6.31	13.5	39.68	11.74	18.36
9.67	25.4	11.72	13.46	12.7	44.57	13.17	78.27
11.33	68.66	11.83	61.81	13.55	7.26	15.31	88.33
9.99	58.43	11.39	68.25	11.03	53.28	14.96	32.14
12.96	38.95	12.12	41.68	13.25	56.38	13.58	55.16
9.44	30.82	8.86	82.87	15.25	9.62	15.5	85.2
11.52	71.49	12.68	29.53	14.57	12.61	12.9	55.93
9.45	71.49	13.76	68.59	9.61	20.64	11.54	46.61
10.45	76.05	13.25	36.9	10.42	22.01	12.37	33.21
12.18	60.01	11.95	7.77	9.83	77.98	11.36	79.17
10.71	42.06	10.68	36.89			12.58	85
11.76	0	14.04	1.2			12.71	21.56
11.56	48.13	11.95	7.86			12.25	80.24
9.15	21.15	11.85	52.55			12.72	47.75
12.6	40.3	13.49	79			14.11	40.81
12.94	47.26	9.9	4.4			12.54	64.86
13.3	32.64	12.23	3.66			9.84	30.96
		11.98	23.24			12.48	0
		9.71	0			12.66	24.29
		9.22	44.42			12.64	16.09
		10.17	52.31			12.8	28.94
		9.92	40.6			11.44	45.53
		10.69	41.36			10.85	51.91
		10.4	88.54			10.91	21.19
						12.92	43.41
						14.26	48.81
						10.11	59.78
						9.57	26.98
						9.61	78.79
						8.13	29.57
						12.92	65.95
						8.25	44.97
						14.32	55.3
						9.71	78.08
						13.52	54.95
						13.23	62.93
						13.85	48.32
						14.46	15.26
						11.3	59.93
						11.73	57.67
						14.54	76.6
						12.77	50.42
						12.64	48
						10.49	84.27
						13.74	19.37

5	P4 (84-100Ma)	5	P5(112-190Ma)	5	P6 (222-270Ma)	7	P5 (112-190Ma)
length (um)	angle(°)	length (um)	angle(°)	length (um)	angle(°)	length (um)	angle(°)
12.14	69.33	10.02	36.89	13.69	40.36	14.63	23.95
12.05	67.85	13.26	66.49	12.76	50.3	13.67	21.29
10.99	84.62	11.28	44.19	12.94	38.43	13.49	27.15
10.87	50.33	13.33	44.55	13.45	61.63	13.2	0
11.35	37.4	14.53	53.72	11.99	83.21	16.04	37.9
11.14	58.61	13.39	83.33	12.03	61.98	13.53	28.73
12.23	75.03	15.48	88.01	12.81	69.76	13.84	16.12
10.68	11.8	14.43	36.08	12.34	70.26	11.01	26.39
11.55	47.22	12.37	11.25	12.28	73.11	14.23	41.87
10.62	56.66	12.74	65.47	13.13	56.56	14.38	68.46
14.12	49.79	11.15	88.76	10.48	45.47	11.11	59.12
11.04	53.27	11.93	82.76	11.73	59	12.12	26.53
12.72	22.5	12.9	32.84	10.79	55.9	10.68	32.37
12.02	22.5	11.02	55.34	13.24	72.58	12.64	84.03
11.89	52.61	11.29	39.82	11.6	62.88	12.1	23.47
13.79	61.89	12.5	18.17	11.11	18.63	11.45	32.95
14.51	81.55	10.43	34.96	10.01	41.95	14.53	24.42
11.8	32.68	10.63	58.84	12.79	51.52	12.15	74.94
13.24	79.51	10.18	31.1	10.69	53.24	10.92	47.15
11.46	10.12	12.21	64.26	11.37	54	11.67	50.7
14.71	28.19	11.56	10.89	10.61	26.68	14.16	83.2
11.29	55.6	13.79	60.61	10.12	50.38	15.15	15.14
14	26.9	12.15	63.03	12.32	53.96	13.27	17.81
11.5	48.67	11.27	30.67	13.82	60.81	12.53	71.05
12.27	17.68	11.35	54.23	10.96	87.52	12.82	67.7
12.84	75.86	11.6	46.02	14.51	36.64	11.96	82.94
12.34	23.28	11.32	46.02	12.09	29.08	13.54	76.65
13.11	0	11.21	88.6	12.64	22.51	15.98	43.78
14.51	14.87	13.3	64.99	10.72	52.44	13.73	42.41
11.51	24.86	14.93	45.92	11.42	11.83	13.49	74.2
		15.56	83.46	10.4	87.52	14.56	84.68
		14.51	45.79	11.3	53.26	12.59	88.29
		11.77	35.66	11.51	4.29	12.24	70.68
		11.8	61.58	13.61	36.86	11.82	65.27
		12.17	49.03	11.47	41.13	11.01	73.89
		14.91	31.94	14.55	69.27		
		12.41	21.38	11.86	16.98		
		12.88	57.69	12.28	84		
		12.73	18.7	13.72	50.38		
		11.2	24.95	13.36	88.09		
		12.96	85.6	13.8	38.01		
		12.72	63.52	12.34	68.74		
		12.24	67.55	10.53	82.93		
		10.58	89.03	13.77	61.41		
		10.17	89.63	10.41	68.73		
		10.27	52.61	12.39	84.71		
		12.51	44.82	13.09	6.91		
				15.2	80.14		
				14.78	64.2		
				14.69	34.69		

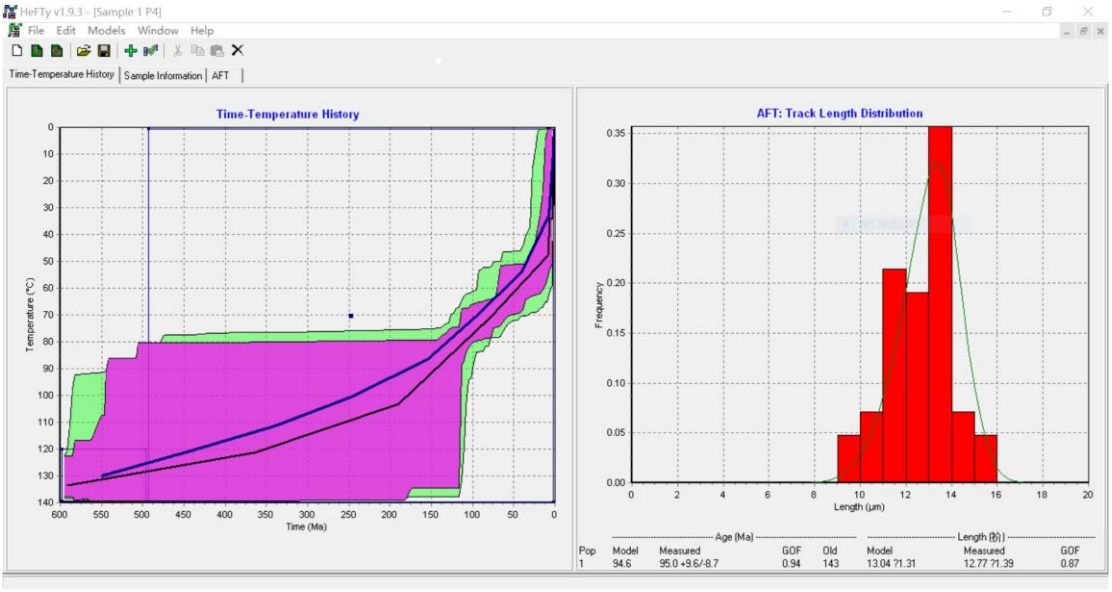
HeFTy v1.9.3 - [Sample 1 P4]
File Edit Models Window Help
Time-Temperature History | Sample Information | AFT
Time-Temperature History
Temperature (°C)
Time (Ma)
AFT: Track Length Distribution
Frequency
Length (µm)
Age (Ma)
Length (µm)
Pop Model Measured GOF Old Model Measured GOF
1 94.6 95.0 +9.6/-8.7 0.94 143 13.04 71.31 12.77 71.39 0.87

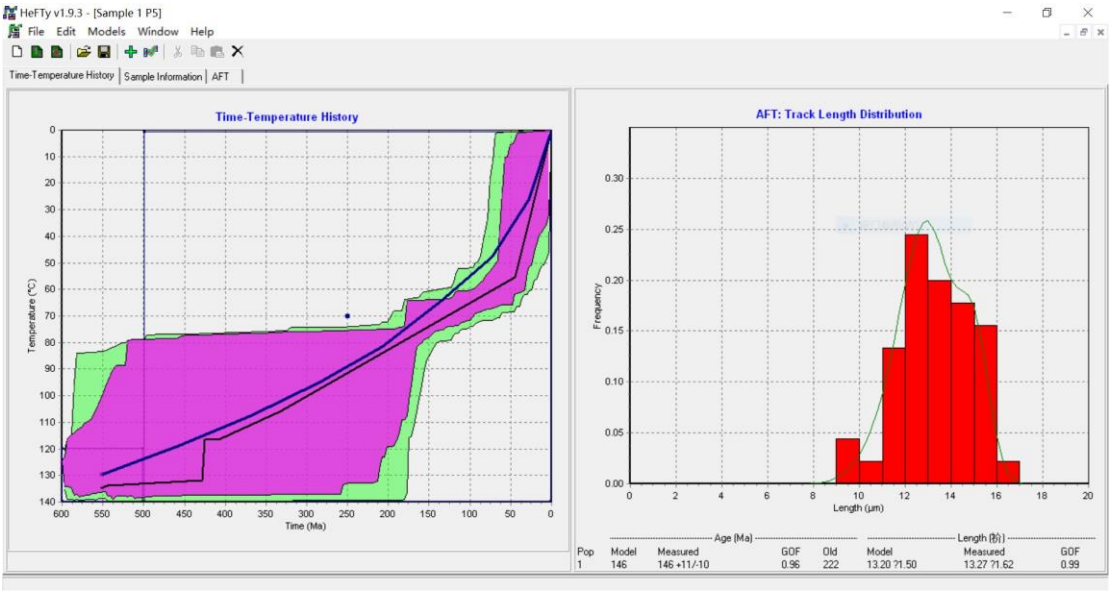
HeFTy v1.9.3 - [Sample 1 P5]
File Edit Models Window Help
Time-Temperature History | Sample Information | AFT
Time-Temperature History
Temperature (°C)
Time (Ma)
AFT: Track Length Distribution
Frequency
Length (µm)
Age (Ma)
Length (µm)
Pop Model Measured GOF Old Model Measured GOF
1 146 146 +11/-10 0.96 222 13.20 71.50 13.27 71.62 0.99

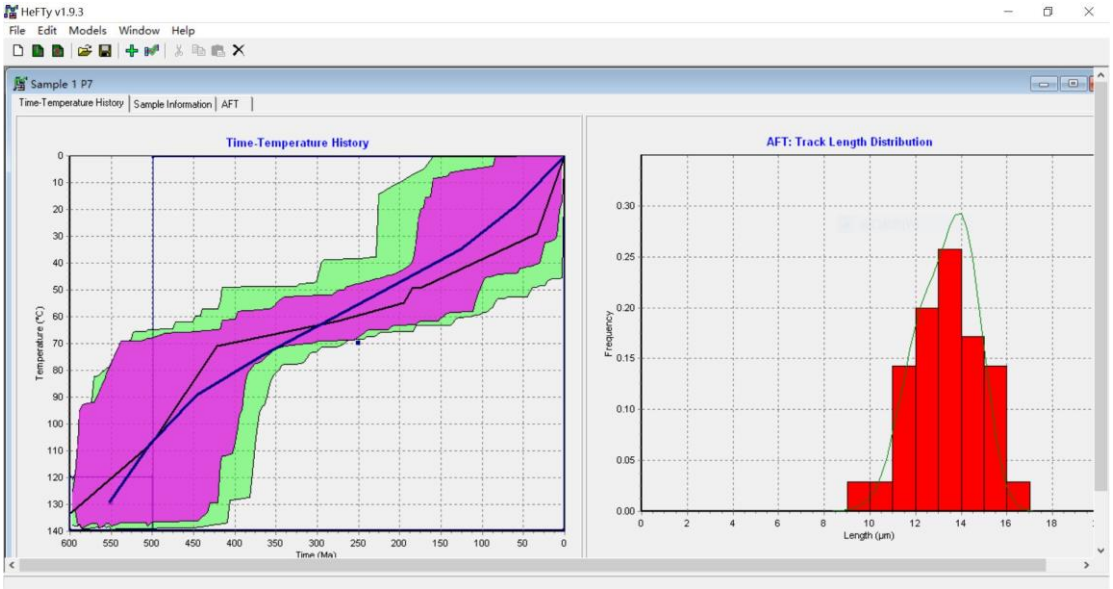
HeFTy v1.9.3
File Edit Models Window Help
Sample 1 P7
Time-Temperature History | Sample Information | AFT
Time-Temperature History
Temperature (°C)
Time (Ma)
AFT: Track Length Distribution
Frequency
Length (µm)

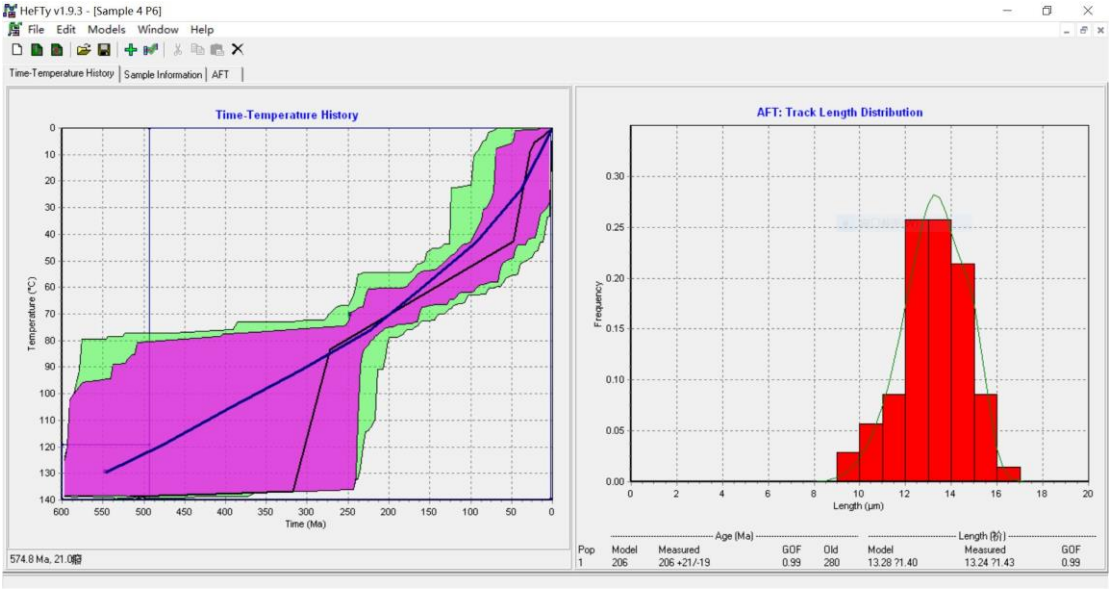
HeFTy v1.9.3 - [Sample 4 P6]
File Edit Models Window Help
Time-Temperature History | Sample Information | AFT
Time-Temperature History
Temperature (°C)
Time (Ma)
574.8 Ma, 21.0
AFT: Track Length Distribution
Frequency
Length (µm)
Age (Ma)
Length (µ)
Pop Model Measured GOF Old Model Measured GOF
1 206 206 +21/-19 0.99 280 13.28 71.40 13.24 71.43 0.99

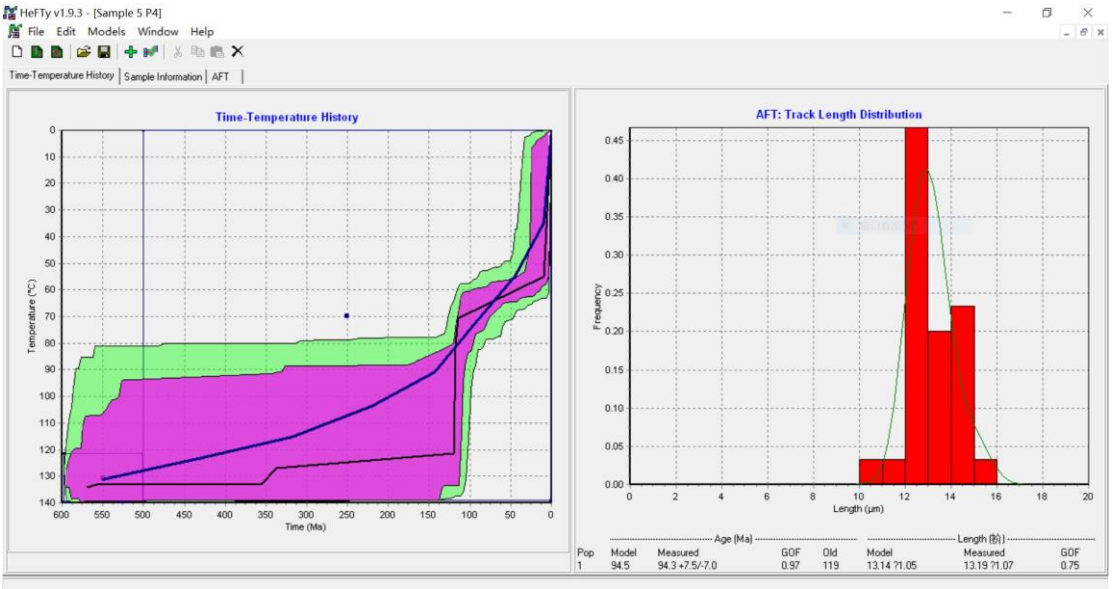
HeFTy v1.9.3 - [Sample 5 P4]
File Edit Models Window Help
Time-Temperature History | Sample Information | AFT
Time-Temperature History
Temperature (°C)
Time (Ma)
AFT: Track Length Distribution
Frequency
Length (µm)
Age (Ma)
Length (µ)
Pop Model Measured GOF Old Model Measured GOF
1 94.5 94.3 +7.5/-7.0 0.97 119 13.14 71.05 13.19 71.07 0.75

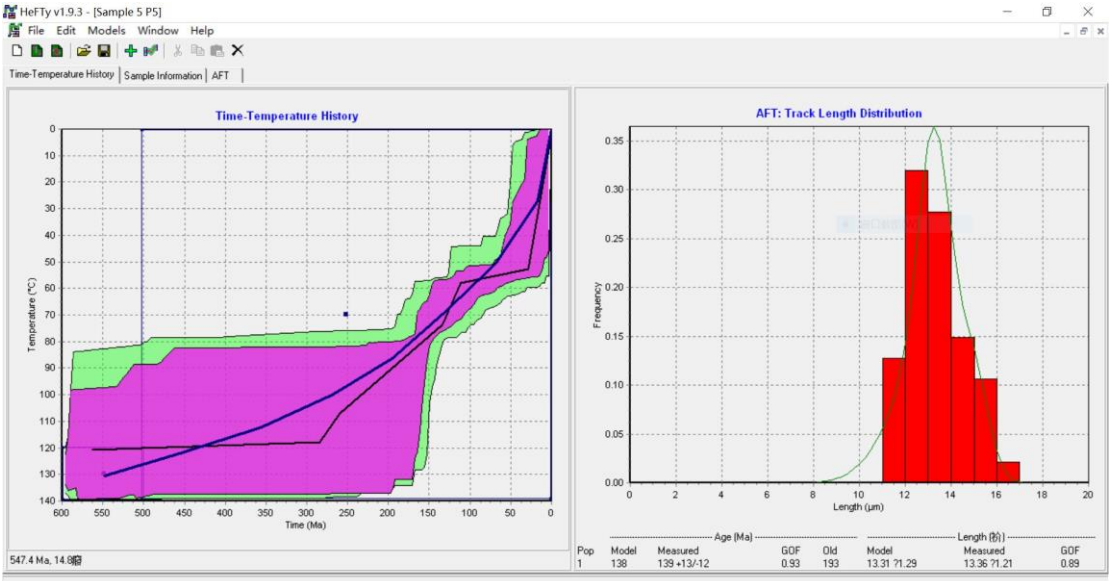
HeFTy v1.9.3 - [Sample 5 P5]
File Edit Models Window Help
Time-Temperature History | Sample Information | AFT
Time-Temperature History
Temperature (°C)
Time (Ma)
547.4 Ma, 14.8
AFT: Track Length Distribution
Frequency
Length (µm)
Age (Ma)
Length (µ)
Pop Model Measured GOF Old Model Measured GOF
1 138 139 +13/-12 0.93 193 13.31 71.29 13.36 71.21 0.89

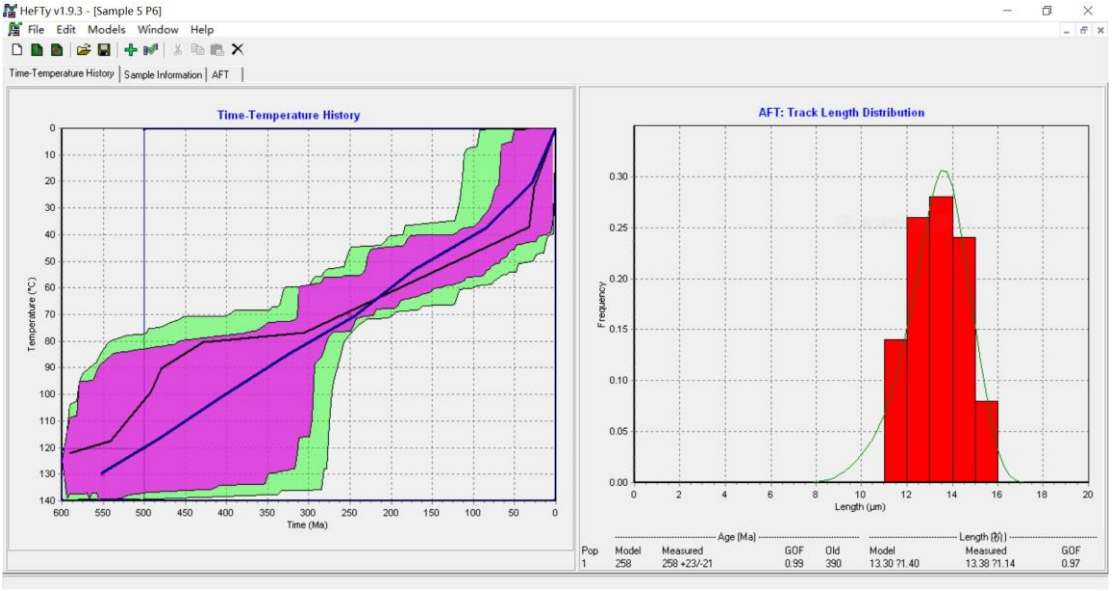
HeFTy v1.9.3 - [Sample 5 P6]
File Edit Models Window Help
Time-Temperature History | Sample Information | AFT
Time-Temperature History
Temperature (°C)
Time (Ma)
AFT: Track Length Distribution
Frequency
Length (µm)
Age (Ma)
Length (µ)
Pop Model Measured GOF Old Model Measured GOF
1 258 258 +23/-21 0.99 390 13.30 71.40 13.38 71.14 0.97

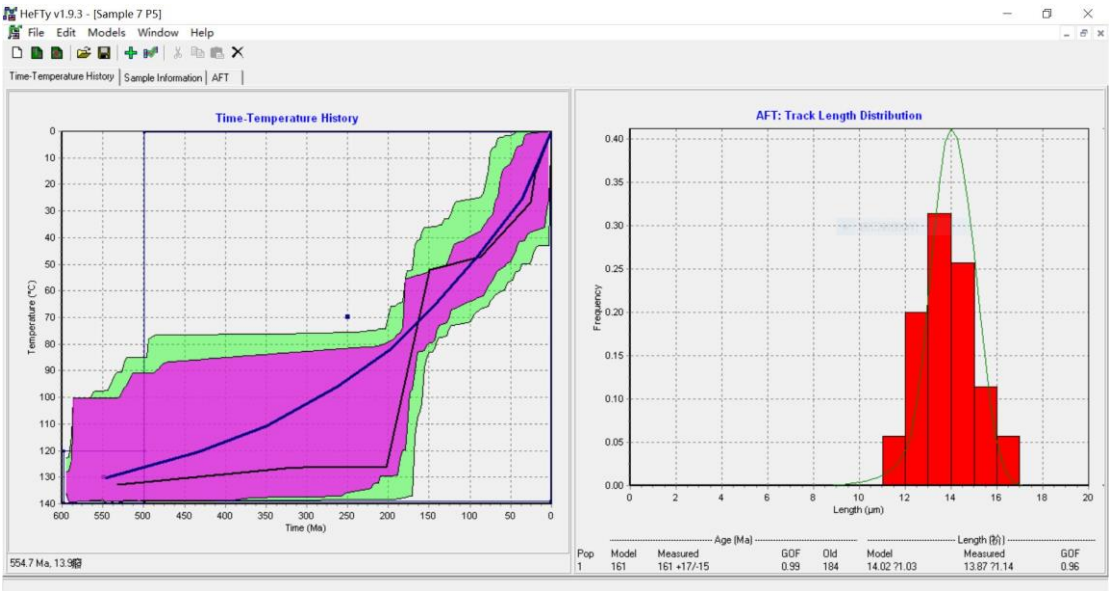
HeFTy v1.9.3 - [Sample 7 P5]
File Edit Models Window Help
Time-Temperature History | Sample Information | AFT
Time-Temperature History
Temperature (°C)
Time (Ma)
554.7 Ma, 13.9
AFT: Track Length Distribution
Frequency
Length (µm)
Age (Ma)
Length (µ)
Pop Model Measured GOF Old Model Measured GOF
1 161 161 +17/-15 0.99 184 14.02 71.03 13.87 71.14 0.96

4. MDS results (include age data from Perotti et al., 2018)

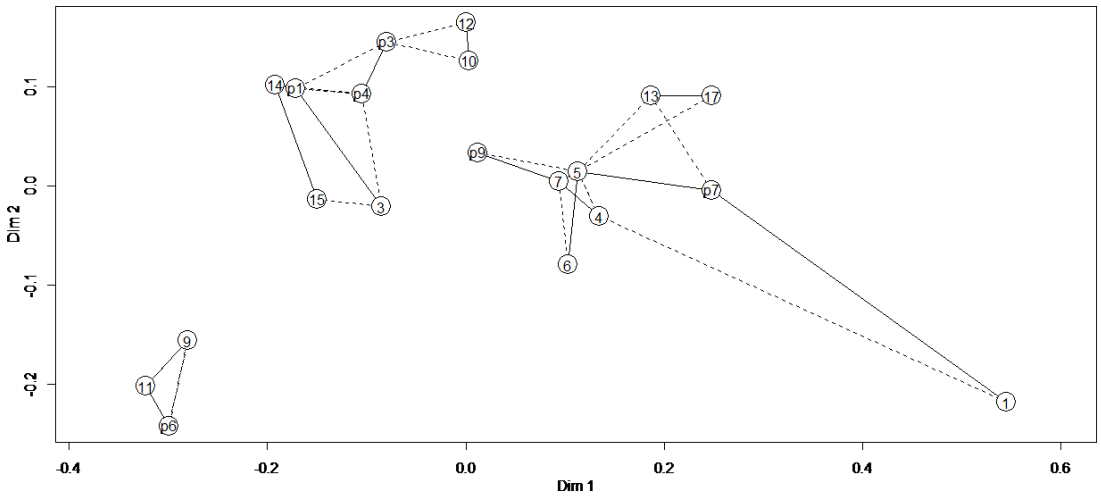

Multidimensional Scaling results of samples related to table 4.1 with samples from the published paper by Perotti et al., 2018. showing the relative of each sample. Samples 2, 8, 16, 18 and samples p2, p5, p8 are too less grains so not included. ‘similar’ samples cluster closely together, and ‘dissimilar’ samples plot far apart (Vermeesch, 2013). Location of samples showed in Fig 4.2.

References

Adam, P. M., Alan, F. C., Dunlap, W. J., 2009. Geochronology of Mount Morning, Antarctic a: two-phase evolution of a long-lived trachyte-basanite-phonolite eruptive center. Bull. Volcanol., 72: 357-371. doi.org/10.1007/s00445-009-0319-1

Adams, R. M., R. A., Fleming, C., Chang, C., McCarl, B. A. and Rosenzweig, C., 1995. A reassessment of the economic effects of global climate change on U.S. agriculture. Clim. Change, 30: 147-167. doi.org/10.1007/BF01091839

Adams, C. J., 1986. Geochronological studies of the Swanson Formation of Marie Byrd Land, West Antarctica, and correlation with northern Victoria Land, East Antarctica, and South Island, New Zealand. New Zeal. J. Geol. Geop., 29(3): 345-358. doi.org/10.1080/00288306.1986.10422157

Alley, R. B. and MacAyeal, D. R., 1993. West Antarctic ice sheet collapse: chimera or clear danger? Antarct. J. U.S., 28 (5): 59-60.

Allibone, A. H., Cox, S. C., Graham, I. J., Smillie, R. W., Johnstone, R. D., Ellery, S. G. and Palmer, K., 1993a. Granitoids of the Dry Valleys area, southern Victoria Land, Antarctica: plutons, field relationships, and isotopic dating. New Zeal. J. Geol. Geop., 36: 281-297.

Allibone, A. H., Cox, S. C. and Smillie, R. W., 1993b. Granitoids of the Dry Valleys area, southern Victoria Land: geochemistry and evolution along the early Paleozoic Antarctic Craton margin. New Zeal. J. Geol. Geop., 36: 299-316.

Allibone, A. H., Cox, S. C., Graham, I. J., Smillie, R. W., Johnstone, R. D., Ellery, S. G. and Palmer, K., 1993. Granitoids of the Dry Valleys area, southern Victoria Land, Antarctica: Plutons, field relationships, and isotopic dating. New Zeal. J. Geol. Geop., 36(3): 281-297. doi.org/10.1080/00288306.1993.9514576.

Amidon, W. H., Burbank, D. W. and Gehrels, G. E., 2005. U-Pb zircon ages as a sediment mixing tracer in the NepalHimalaya. Earth Planet. Sci. Lett., 235: 244-260. doi.org/10.1016/j.epsl.2005.03.019

Anderson, J. B., Shipp, S. S., Bartek, L. R., Reid, D. E., 1992. Evidence for a grounded ice sheet on the Ross Sea continental shelf during the late Pleistocene and preliminary paleodrainage reconstruction. AGU Antarct. Res. Ser., 57: 39-62. doi.org/10.1029/AR057p0039

Anderson, J. B., Shipp, S. S., Lowe, A. L., Wellner, J. S., Mosola, A. B., 2002. The Antarctic Ice Sheet during the Last Glacial Maximum and its subsequent retreat history: a review. Quat. Sci. Rev., 21: 49-70. doi.org/10.1016/S0277-3791(01)00083-X

Anderson, J. B., Bart P., Mckay R., Licht, K. J., Shipp, S. S., Lowe, A. L., Wellner, J. S. and Mosola, A. B., 2014. Ross Sea Paleo-Ice Sheet Drainage and Deglacial History during and since the LGM The Antarctic Ice Sheet during the Last Glacial Maximum and Its Subsequent Retreat History: A Review. Quat. Sci. Rev., 100: 31-54. doi.org/10.1016/j.quascirev.2013.08.020.

Andriessen, P. A., Helmes, M., Hooghiemstra, H., Riezebos, P. A., Van der Hammen, T., 1993. Absolute chronology of the Pliocene-Quaternary sediment sequence of the Bogota area, Colombia. Quatern. Sci. Rev., 12: 483-501.

Balestrieri, M. L., Bigazzi, G. and Ghezzo. C., 1997. Uplift-denudation of the Transantarctic Mountains between the David and the Mariner glaciers, northern Victoria Land (Antarctica); constraints by apatite fission-track analysis. The Antarctic region: geological evolution and processes. 547-554.

Balshaw, K. M., 1980. Antarctic glacial chronology reflected in the Oligocene through Pliocene sedimentary section in the Ross Sea. Ph.D. Thesis, Rice University, 140.

Barbarand, J., Carter, A., Wood, I. and Hurford, T., 2003a. Compositional and structural control of fission-track annealing in apatite. Chem. Geol.,198: 107-137. doi.org/10.1016/S0009-2541(02)00424-2

Barbarand, J., Carter, A. and Hurford, T., 2003b. Variation in apatite fission-track length measurement: implications for thermal history modelling. Chem. Geol., 198: 77-106. doi.org/10.1016/S0009-2541(02)00423-0

Barrett, P. J. and Scientific Staff, 1985. Plio-Pleistocene glacial sequence cored at CIROS-2, Ferrar Fjord, western McMurdo Sound. N. Z. Antarct. Rec., 6: 8-19.

Barrett, P. J., 1991. The Devonian to Triassic Beacon Super- group of the Transantarctic Mountains and correlatives in other parts of America. In: The Geology of Antarctica, Tingey, R. J., ed., Monographs on Geology and Geophysics, Oxford Univ. Press, Oxford, U. K., 17: 120-152.

Barrett, P. J. and Hambrey, M. J., 1992. Plio - Pleistocene sedimentation in Ferrar Fiord, Antarctica. Sedimentology, 39: 109-123. doi.org/10.1111/j.1365-3091.1992.tb01025.x

Barrett, B. E., Nicholls, K. W., Murray, T., Smith, A. M., and Vaughan, D. G., 2009. Rapid recent warming on Rutford Ice Stream, West Antarctica, from borehole thermometry. Geophys. Res. Lett., 36: L02708. doi.org/10.1029/2008GL036369

Bart, P. J., and Cone, A. N., 2012. Early Stall of West Antarctic Ice Sheet Advance on the Eastern Ross Sea Middle Shelf Followed by Retreat at 27, 500 14 C Yr BP. Palaeogeogr. Palaeoclimatol. Palaeoecol., 335-336: 52-60. doi.org/10.1016/j.palaeo.2011.08.007.

Behrendt, J. C., Donald, D., Blankenship, D. D., Alan, K. C., 1995. Glacial removal of late Cenozoic subglacially emplaced volcanic edifices by the West Antarctic ice sheet. Geology, 23(12): 1111-1114. doi.org/10.1130/0091-7613(1995)023<1111:GROLCS>2.3.CO;2

Behrendt, J., Finn, C., Blankenship, D. D., Morse, D. and Bell, R., 2004. Do the Volcanic Rocks Erupted in the West Antarctic Rift System Beneath the West Antarctic Ice Sheet (WAIS), Interpreted from Aeromagnetic Surveys, Define a Large Igneous Province? AGU Fall Meeting.

Berry, R. F., Jenner, G. A., Meffre, S. and Tubrett, M. N., 2001. A North American provenance for Neoproterozoic to Cambrian sandstones in Tasmania? Earth Planet. Sci. Lett., 56: 336-342. doi.org/10.1016/S0012-821X(01)00436-8

Bindschadler. R. A. and Scambos, T. A., 1991. Satellitc-image-derived velocity field of an Antarctic ice stream. Science, 252 (5003): 242-246. doi.org/10.10.1126/science.252.5003.242

Boulton, G. S., 1978. Boulder shapes and grain-size distributions of debris as indicators of transport paths through a glacier and till genesis. Sedimentology, 25: 773-799. doi.org/10.1111/j.1365-3091.1978.tb00329.x

Bradshaw, J. D., Andrews, P. B. and Field, B. D., 1983. Swanson formation and related rocks of Marie Byrd Land and a comparison with the Robertson Bay Group of northern Victoria Land, Antarct. Earth Sci., 1982: 274-279.

Brandon, M. T., 1992. Decomposition of fission-track grain age distributions. Am. J. Sci., 292: 535-564. doi.org/10.2475/ajs.292.8.535

Brand, J. F., 1979. Low Grade Metamorphic Rocks of the Ruppert and Hobbs Coasts of Marie Byrd Land, Antarctica, MSc thesis, Tex.Tech Univ., Lubbock, Tex., 49.

Braun, J., van der Beek, P., and Batt, G., 2006. Quantitative Thermochronology: Numerical Methods for the Interpretation of Thermochronological Data: Cambridge, New York, Cambridge University Press, 258.

Bursill, L. A. and Braunshausen, G., 1990. Heavy-ion irradiation tracks in zircon. Phil. Mag., 62: 395-420. doi.org/10.1080/01418619008244787

Burtner, R. L., Nigrini, A. and Donelick, R. A., 1994. Thermochronology of Lower Cretaceous source rocks in the Idaho-Wyoming Thrust Belt. Bull. Am. Assoc. Petrol. Geol., 78: 1613-1636.

Bushnell, V.C., 1974. Antarctic map folio series. Antarct. J. U. S., 6.

Cande, S., Stock, J., Mцller D., & Ishihara, T., 2000. Cenozoic motion between East and West Antarctica. Nature, 404: 145-150. doi.org/10.1038/35004501

Cande, S. C. and Stock, J. M., 2006. Constraints on the Timing of Extension in the Northern Basin, Ross Sea. In: Fütterer, D.K., Damaske, D., Kleinschmidt, G., Miller, H., Tessensohn, F., ed., Antarctica, Springer, Berlin, Heidelberg, 319-326. doi.org/10.1007/3-540-32934-X_40

Carlson, W. D., 1990. Mechanisms and kinetics of apatite fission-track annealing. Am. Mineral., 75: 1120-1139.

Carlson, W. D., Donelick, R. A., Ketcham, R. A.,1999. Variability of apatite fission-track annealing kinetics: I. Experimental results. Am. Mineral., 84: 1213-1223.

Carter, A. and Moss, S. J., 1999. Combined detrital-zircon fission-track and U-Pb dating: a new approach to understanding hinterland evolution. Geology, 27: 235-238.

Chadderton, L. T., 2003. Nuclear tracks in solids: registration physics and the compound spike. Radiat. Meas., 36: 13-34. doi.org/10.1016/S1350-4487(03)00094-5

Church, J. A., Woodworth, P. L., Aarup, T. and Wilson, W. S., ed., 2010. Understanding Sea-Level Rise and Variability. Wiley-Blackwell, Hoboken, N. J., USA, 428. doi.org/10.1002/9781444323276

Church, J. A., Gregory, J. M., White, N. J., Platten, S. M. and Mitrovica, J. X., 2011a. Understanding and projecting sea level change. Oceanography, 24: 130-143. doi.org/10.5670/oceanog.2011.33

Cloetingh, S. A. P. L., Ziegler, P. A., Bogaard, P. J. F., Andriessen, P. A. M., Artemieva, I. M., Bada, G., Van Balen, R. T., Beekman, F., Ben-Avraham, Z., Brun, J. P. and Bunge, H. P., 2007. TOPO-EUROPE: The geoscience of coupled deep Earth-surface processes. Glob. Planet. Change, 58(1): 1-118. doi.org/10.1016/j.gloplacha.2007.02.008

Cole, J. W. and Ewart, A., 1968. Contributions to the volcanic geology of the Black Island, Brown Peninsula, and Cape Bird areas, McMurdo Sound, Antarctica. New Zeal. J. Geol. Geop., 11: 793-828.

Cook, Y. A., and Craw, D., 2002. Neoproterozoic structural slices in the Ross Orogen, Skelton Glacier area, South Victoria Land, Antarctica, New Zeal. J. Geol. Geop., 45(1): 133-143. doi.org/10.1080/00288306.2002.9514965.

Cooper, A. K. and Davey, F. J., 1985. Episodic rifting of Phanerozoic rocks in the Victoria Land basin, western Ross Sea, Antarctica. Science, 229: 1085-1087. doi.org/10.1126/science.229.4718.1085

Cornamusini, G., and Talarico, F. M., 2016. Miocene Antarctic ice dynamics in the Ross Embayment (Western Ross Sea, Antarctica): Insights from provenance analyses of sedimentary clasts in the AND-2A drill core. Glob. Planet. Change, 146: 38-52. doi.org/10.1016/j.gloplacha.2016.09.001

Dalziel, I. W. D. and Elliot, D. H., 1982. West Antarctica: problem child of Gondwanaland. Tectonics, 1(1): 3-19. doi.org/10.1029/TC001i001p00003

Davey, F. J., Cande, S. C. and Stock, J. M., 2006. Extension in the western Ross Sea region-links between Adare Basin and Victoria Land Basin, Geophys. Res. Lett., 33: L20315. doi.org/10.1029/2006GL027383.

Davey, F. J., Granot, R., Cande, S. C., Stock, J. M., Selvans, M., and Ferraccioli, F. 2016. Synchronous oceanic spreading and continental rifting in West Antarctica, Geophys. Res. Lett., 43: 6162-6169. doi.org/10.1002/2016GL069087.

Degraaf-Surpless, K., Mahoney, J. B., Wooden, J. L. and Mcwilliams, M. O., 2003. Lithofacies control in detrital zircon provenance studies: insights from the cretaceous methow basin, southern Canadian Cordillera. Geol. Soc. Am. Bull., 115: 899-915. doi.org/10.1130/B25267.1

Denton, G. H., Hughes, T. J., 2000. Reconstruction of the Ross Ice Drainage System, Antarctica, at the Last Glacial Maximum. Geogr. Ann., 82(2-3): 143-166. doi.org/10.1111/j.0435-3676.2000.00120.x.

Dietze, M., Kreutzer, S., Burow, C., Fuchs, M., Fischer, M., and Schmidt, C., 2016. The abanico plot: visualizing chronometric data with individual standard errors. Quat. Geochronol., 31: 12-18. doi.org/10.1016/j.quageo.2015.09.003

Dodson, M. H., 1973. Closure temperature in cooling geochronological and petrological systems. Contrib. Mineral. Petrol., 40: 259-274.

Dolan, A. M., de Boer, B., Bernales, J., Hill, D. J. and Haywood, A. M., 2018. High climate model dependency of Pliocene Antarctic ice-sheet predictions. Nat. Commun., 9**:** 2799 doi:10.1038/s41467-018-05179-4

Domack, E. W., Jacobson, E. A., Shipp, S., Anderson, J. B., 1999. Late Pleistocene-Holocene retreat of the West Antarctic Ice Sheet in the Ross Sea: part 2 - sedimentologic and stratigraphic signature. Geol. Soc. Am. Bull., 111(10): 1517-1536. doi.org/10.1130/0016-7606(1999)111%3C1517:LPHROT%3E2.3.CO;2.

Donelick, R. A., 1993. A method of fission track analysis utilizing bulk chemical etching of apatite. Patent 5267274, U.S.A.

Donelick, R. A. 1993. Apatite etching characteristics versus chemical composition. Nucl. Tracks Radiat. Meas., 21(4): 604.

Donelick, R. A., Ketcham, R. A., Carlson, W. D., 1999. Variability of apatite fission track annealing kinetics: II. Crystallographic orientation effects. Am. Mineral., 84: 1224-1234.

Dunbar, R. B., Anderson, J. B., Domack, E. W. and Jacobs, S. S., 1985. Oceanographic influences on sedimentation along the Antarctic continental shelf: oceanology of the Antarctic Continental Shelf. Am. Geophys. Union Antarct. Res. Ser., 43: 291-312. doi.org/10.1029/AR043p0291.

Dunlap, A., Jaskierowicz, G., Jensen, J. and Della-Negra, S., 1997. Track separation due to dissociation of MeV C60 inside a solid. Nucl. Instr. Methods B, 132: 93-98. doi.org/10.1016/S0168-583X(97)00390-X

Durrani I. R. and Bull, R. K., 1987. Solid State Nuclear Track Detection (Principles, Methods and Application). Pergamon Press, Oxford. doi.org/10.1016/C2013-0-02771-5

Ehrmann, W., 1998. Implications of late Eocene to early Miocene clay mineral assemblages in McMurdo Sound (Ross Sea, Antarctica) on paleoclimate and ice dynamics. Palaegeogr. Palaeoclimatol. Palaeoecol., 139: 213-231. doi.org/10.1016/S0031-0182(97)00138-7

Ehrmann, W. and Polozek, K., 1999. The heavy mineral record in the Pliocene to Quaternary sediments of the CIROS-2 drill core, McMurdo Sound, Antarctica. Sedimentary Geology, 128: 223-244. doi.org/10.1016/S0037-0738(99)00071-8

Elliot, D. H., and Fleming, T. H., 2008. Physical volcanology and geological relationships of the Jurassic Ferrar Large Igneous Province, Antarctica, J. Volcanol. Geotherm. Res., 172(1-2): 20-37. doi.org/10.1016/j.jvolgeores.2006.02.016

Elliot, D. H., Fanning, C. M. and Hulett, S. R. W., 2015. Age provinces in the Antarctic craton: Evidence from detrital zircons in Permian strata from the Beardmore

Glacier region, Antarctica. Gondwana Res., 28:152-164. doi.org/10.1016/j.gr.2014.03.013

Farmer, G. L., Barber, D. and Andrews, J., 2003. Provenance of Late Quaternary ice-proximal sediments in the North Atlantic: Nd, Sr and Pb isotopic evidence. Earth Planet. Sci. Lett. Version 1, 209: 227-243. doi.org/10.1016/S0012-821X(03)00068-2

Farmer, L., 2004. Igneous petrology. Geotimes Version 1, 49 (7): 30-31.

Farmer, G. L., Licht, K. J., Swope, R. J. and Andrews, J., 2006. Isotopic constraints on the provenance of fine-grained sediment in LGM tills from the Ross Embayment, Antarctica. Earth Planet. Sci. Lett., 249(1-2): 90-107. doi.org/10.1016/j.epsl.2006.06.044

Farme, G. L. and Licht, K. J., 2016. Generation and fate of glacial sediments in the central Transantarctic Mountains based on radiogenic isotopes and implications for reconstructing past ice dynamics. Quat. Sci. Rev., 150: 98-109. doi.org/10.1016/j.quascirev.2016.08.002

Faure, G and Mensing, T. M., 1993. K-Ar dates and paleomagnetic evidence for Cretaceous alteration of Mesozoic basaltic lava flows, Mesa Range, northern Victoria Land, Antarctica. Chem. Geol., 109: 305-315. doi.org/10.1016/0009-2541(93)90077-V

Findlay, S. and Meyer, J. L., 1984. Significance of bacterial biomass and production as an organic carbon source in lotic detrital systems. Bull. Mar. Sci., 35: 318-325.

Fitzgerald, P. G., and Gleadow, A. J. W., 1988. Fission-track geochronology, tectonics and structure of the Transantarctic Mountains in northern Victoria Land, Antarctica. Chem. Geol., 73: 169-198. doi.org/10.1016/0168-9622(88)90014-0

Fitzgerald, P. G., 1992. The Transantarctic Mountains of southern Victoria Land: The application of apatite fission track analysis to a rift shoulder uplift. Tectonics, 11: 634-662. doi:10.1029/91TC02495

Fitzgerald, P. G., 1994. Thermochronologic constraints on post-Paleozoic tectonic evolution of the central Transantarctic Mountains, Antarctica. Tectonics, 13: 818-836. doi.org/10.1029/94TC00595

Fitzgerald, P. G. and Stump, E., 1997. Cretaceous and Cenozoic episodic denudation of the Transantarctic Mountains, Antarctica: New constraints from apatite fission track thermochronology in the Scott Glacier region. J. Geophys. Res.-Solid Earth Planets, 102: 7747-7765. doi.org/10.1029/96JB0 3898

Fitzgerald, P. G., 2002. Tectonics and landscape evolution of the Antarctic plate since the breakup of Gondwana, with an emphasis on the West Antarctic Rift System and the Transantarctic Mountains. Royal Soc. New Zeal. Bull., 35: 453-469.

Fitzgerald, P. G., Baldwin, S. L., Webb, L. E. and O'Sullivan, P. B., 2006. Interpretation of (U-Th)/He single grain ages from slowly cooled crustal terranes: A case study from the Transantarctic Mountains of southern Victoria Land: Chem. Geol., 225: 91-120. doi.org/10.1016/j.chemg eo.2005.09.001

Fitzgerald, P. G., and Baldwin, S. L., 2007. Thermochronologic constraints on Jurassic rift flank denudation in the Thiel Mountains, Antarctica. In: Antarctica: A Keystone in a Changing World - Online Proceedings for the 10th International Symposium on Antarctic Earth Sciences, Santa Barbara, California, U. S. A., Cooper, A., Raymond, C. and the 10th ISAES Editorial Team, U.S. Geol. Surv. Open File Rep., 2007-1047: 044. doi:10.3133/of2007-1047.srp044.

Fleischer, R. L., Price, P. B. and Walker, R. M., 1965. Effects of temperature, pressure, and ionization of the formation and stability of fission tracks in minerals and glasses. J. Geophy. Res., 70:149-502. doi.org/10.1029/JZ070i006p01497

Fleischer, R. L. and Hart, H. R., 1972. Fission track dating: techniques and problems. In: Calibration of hominoid evolution, Bishop, W. W., Miller, J. A. and Cole, S., ed., Scottish Academic Press, Edinburgh, 135-170.

Fleischer, R. L., Price, P. B. and Walker, R.M., 1975. Nuclear Tracks in Solids. Berkely: Univ. Calif. Press. 605.

Fleming, E. L., Jackman, C. H., Stolarski, R. S., and Considine, D. B., 1999. Simulation of stratospheric tracers using an improved empirically based two-dimensional model transport formulation. J. Geophys. Res., 104(D19): 23911-23934. doi:10.1029/1999JD900332.

Galbraith, R. F., 1981. On statistical models for fission track counts. Math. Geol., 13: 471-478.

Galbraith, R.F. and Green, P. F., 1990. Estimating the component ages in a finite mixture. Nucl. Tracks Radiat. Meas., 17: 197-206. doi.org/10.1016/1359-0189(90)90035-V

Galbraith, R. F. and Laslett, G. M., 1993. Statistical models for mixed fission track ages. Nucl. Tracks Radiat Meas., 21: 459-470. doi.org/10.1016/1359-0189(93)90185-C

Gallagher, K., Brown, R., Johnson, C., 1998. Fission track analysis and its applications to geological problems. Ann. Rev. Earth Planet. Sci., 26: 519-572. doi.org/10.1146/annurev.earth.26.1.519

Garver, J. I., Brandon, M.T., Roden-Tice, M. and Kamp, P. J. J., 1999. Exhumation history of orogenic highlands determined by detrital fission-track thermochronology. In: Exhumation Processes: Normal Faulting, Ductile Flow and Erosion, Ring, U., Brandon, M. T., Lister, G. S. and Willett, S. D., ed., Geol. Soc. Lond Spec. Pub., 154: 283-304. doi.org/10.1144/GSL.SP.1999.154.01.13

Gleadow, A. J. W., 1980. Fission track age of the KBSTuff and associated hominid remains in northern Kenya. Nature, 284: 225-230. doi.org/10.1038/284225a0

Gleadow, A. J. W., 1981. Fission-track dating methods: What are the real alternatives? Nucl. Tracks, 5: 3-14. doi.org/10.1016/0191-278X(81)90021-4

Gleadow, A. J. W. and Duddy, I. R., 1981. A natural long-term annealing experiment for apatite. Nucl. Tracks Radiat. Meas., 5: 169-174. doi.org/10.1016/0191-278X(81)90039-1

Gleadow, A. J. W., Duddy, I. R., Green, P. F. and Lovering, J. F., 1986. Confined fission track lengths in apatite: a diagnostic tool for thermal history analysis. Contrib. Mineral. Petrol., 94: 405-415. doi.org/10.1007/BF00376334

Gleadow, A. J. W. and Fitzgerald, P. G., 1987. Uplift history and structure of the Transantarctic Mountains: new evidence from fission track dating of basement apatites in the Dry Valleys area, southern Victoria Land. Earth. Planet. Sci. Lett., 82: 1-14. doi.org/10.1016/0012-821X(87)90102-6

Golledge, N. R., Christopher, J. F., Andrew, N. M., and Kevin, M. B., 2012. Dynamics of the Last Glacial Maximum Antarctic Ice-Sheet and Its Response to Ocean Forcing. P. N. A. S., 109(40): 16052-16056. doi.org/10.1073/pnas.1205385109.

Green, P. F., Duddy, I. R., Gleadow, A. J. W., Tingate, P. R. and Laslett, G. M.,1986. Thermal annealing of fission tracks in apatite, 1, A quantitative description. Chem. Geol., 59: 237-253. doi.org/10.1016/0168-9622(86)90074-6

Green, P. F., Duddy, I. R., Gleadow, A. J. W., and Lovering, J. F., 1989a. Apatite fission-track analysis as a paleotemperature indicator for hydrocarbon exploration. In: Thermal History of Sedimentary Basins: Methods and Case Histories, Naeser, N. D., McCulloh, T. H., ed., Springer-Verlag, New York, 181-195.

Green, P. F., Duddy, I. R., Laslett, G. M., Hegarty, K.A., Gleadow, A. J. W. and Lovering, J. F., 1989b. Thermal annealing of fission tracks in apatite 4. Quantitative

modeling techniques and extension to geological timescales. Chem. Geol., 79: 155-182. doi.org/10.1016/0168-9622(89)90018-3

Grindley, G.W. and Warren, G., 1964. Stratigraphic nomenclature and correlation in the western Ross Sea region. In: Antarctic Geology, Adie, R. J., ed., North Holland Publishing Co, Amsterdam, 314-333.

Gunn, B.M., 1962. Differentiation in Ferrar Dolerites, Antarctica. N. Z. J. Geol. Geophys., 5: 820-863.

Gunn, B. M. and Warren, G., 1962. Geology of Victoria Land between the Mawson and Mulock Glaciers, Antarctica. N. Z. Geol. Surv. Bull., 71: 1-157.

Gunn, B. M., and Warren, G., 1962. Geology of Victoria Land between the Mawson and Mulock Glaciers, Antarctica, N. Z. J. Geol. Geophys., 5: 407-426. doi:10.1080/00288306.1962. 10420097.

Haldorsen, S., 1981. Grain-size distribution of subglacial till and its relation to glacial crushing and abrasion. Boreas, 10: 91-105. doi.org/10.1111/j.1502-3885.1981.tb00472.x

Hall, K. and Buhmann, D., 1989. Palaeoenvironmental reconstruction from redeposited weathered clasts in the CIROS-1 drill core. Antarct. Sci., 1: 235-238. doi.org/10.1017/S0954102089000350

Hall, B. L. and Denton, G. H., 2000. Radiocarbon chronology of Ross Sea Drift, Eastern Taylor Valley, Antarctica: evidence for a grounded ice sheet in the Ross Sea at the last glacial maximum, Geogr. Ann., 82A: 305. doi.org/10.1111/j.0435-3676.2000.00127.x

Hambrey, M. J. and Barrett, P. J., 1993. Cenozoic sedimentary and climatic record, Ross Sea region, Antarctica. In: The Antarctic Paleoenvironment: A Perspective on Global Change, Kennett, J. P. and Warnke, D. A., ed., Antarct. Res. Ser., 60: 91-124. doi.org/10.1002/9781118668061.ch6

Hambrey, M. J., Barrett, P. J. and Powell R. D., 2002. Late Oligocene and early Miocene glacimarine sedimentation in the SW Ross Sea, Antarctica: The record from offshore drilling - Glacier-Influenced Sedimentation on High-Latitude Continental Margins. In: Dowdeswell, J. A. and Cofaigh, C. O., ed., Spec. Publ. Geol. Soc., London, 203: 105-28.

Harrington, H. J., 1965. Geology and morphology of Antarctica. Biogeography and ecology in Antarctica. Monogr. Biol., 15: 1-71.

Harry, D., Jourdan, L. A., and Sumant, J., 2018. Geodynamic models of the West Antarctic Rift System: Implications for the mantle thermal state. Geosphere, 14. doi.org/10.1130/GES01594.1.

Hauptvogel, D. W. and Passchier, S., 2012. Early–Middle Miocene (17–14Ma) Antarctic ice dynamics reconstructed from the heavy mineral provenance in the AND-2A drill core, Ross Sea, Antarctica. Glob. Planet. Change, 82-83: 38-50 https://doi.org/10.1016/j.gloplacha.2011.11.003.

Hollin, J. T., 1962. On the glacial history of Antarctica. J. Glaciol., 4: 173-195.

Hooke, R. L., Cummings, D. L., Lesemann, J. E., Sharpe, D. R., 2013. Genesis of dispersal plumes in till. Can. J. Earth Sci., 50: 847-855. doi.org/10.1139/cjes-2013-0018

Huerta, A., Blythe, A. E. and Utevsky, E., 2011. Collapse of a Mesozoic West Antarctic plateau: evidence from low temperature thermochronology and geodynamical modelling. Geol. Soc. Am. Annual Meeting, Minneapolis.

Hughes, T., 1973. Is the West Antarctic Ice Sheet disintegrating? J. Geophys. Res., 78: 7884-7910. doi.org/10.1029/JC078i033p07884

Hughes, T. J., 1977. West Antarctic ice streams. Reviews of Geophysics and Space Physics, 15(1): 1-46. doi.org/10.1029/RG015i001p00001.

Hurford, A. J., and Green, P. F., 1983. The zeta age calibration of fission track dating. Chem. Geol., 1: 285-317. doi.org/10.1016/S0009-2541(83)80026-6

Hurford, A. J., 1990. International Union of Geological Sciences Subcommission on Geochronology recommendation for the standardization of fission track dating calibration and data reporting. Nucl. Tracks, 17: 233-236. doi.org/10.1016/1359-0189(90)90040-5

Hurford, A. J. and Carter, A., 1991. The role of fission track dating in discrimination of provenance. *In:* Developments in Sedimentary Provenance Studies. Morton, A. C., Todd, S. P. and Haughton, P. D. W., ed., Geol. Soc. Spec. Pub., 57: 67-78.

Kellogg, T. B., Truesdale, R. S., Osterman, L. E., 1979. Late Quaternary extent of the West Antarctic Ice Sheet: new evidence from the Ross Sea cores. Geology, 7(5): 249-253. doi.org/10.1130/0091-7613(1979)7%3C249:LQEOTW%3E2.0.CO;2.

Ketcham, R. A., Donelick, R. A. and Carlson, W. D., 1999. Variability of apatite fission-track annealing kinetics: III. Extrapolation to geological time scales. Am. Mineral., 84: 1235-1255. doi.org/10.2138/am-1999-0903

Ketcham, R. A., 2005. The role of crystallographic angle in characterizing and modeling apatite fission-track length data. Radiat. Meas., 39: 595-601. doi.org/10.1016/j.radmeas.2004.07.008.

Ketcham, R. A., Andrew, C. A. Donelick, R., Barbarand, J. and Hurford, A. J., 2007. Improved measurement of fission-track annealing in apatite using C-axis projection. Am. Mineral., 92: 789-798. doi.org/10.2138/am.2007.2280.

Kohn, B. P., Pillans, B., McGlone, M. S., 1992. Zircon fission track ages for middle Pleistocene Rangitawa tephra, New Zealand: Stratigraphic and paleoclimatic significance. Palaeogeog. Palaleoclim. Palaeoecol., 95: 73-94. doi.org/10.1016/0031-0182(92)90166-3

Korhonen, F. J., Saito, S., Brown, M., Siddoway, C. S. and Day, J. M. D., 2010a. Multiple generations of granite in the Fosdick Mountains, Marie Byrd Land, West Antarctica; implications for polyphase intracrustal differentiation in a continental margin setting, J. Petrol., 51(3): 627-670. doi.org/10.1093/petrology/egp093.

Korhonen, F. J., Saito, S., Brown, M., Siddoway, C. S., and Day., J. M. D., 2010b. Modeling multiple melt loss events in the evolution of an active continental margin, Lithos., 116(3-4): 230-248. doi.org/10.1016/j.lithos.2009.09.004.

Korhonen, F. J., Brown, M. Grove, M., Siddoway, C. S., Baxter, E. F. and Inglis, J. D., 2012. Separating metamorphic events in the Fosdick migmatite-granite complex, West Antarctica, J. Metamorph. Geol., 30: 165-192. doi.org/10.1111/j.1525-1314.2011.00961.x.

Kowallis, B. J. and Heaton, J. S. and Bringhurst, K.,1986. Fission-track dating of volcanically derived sedimentary rocks. Geology, 14: 19-22. doi.org/10.1130/0091-7613(1986)14%3C19:FDOVDS%3E2.0.CO;2

Kyle, P. R., 1981. Glacial history of the McMurdo Sound area, as indicated by the distribution and nature of McMurdo volcanic rocks in the Dry Valley Drilling Project. In: Dry Valley Drilling Project, McGinnis, L. D., ed., Antarct. Res. Ser., AGU, Washington, DC, 33: 403-412. doi.org/10.1029/AR033

Kyle, P. R., 1990. McMurdo Volcanic Group, western Ross Embayment, Introduction. In: Volcanoes of the Antarctic Plate and Southern Oceans, Le Masurier, W. E. L. and Thomson, J.W., ed., Antarct. Res. Ser., AGU, Washington, DC, 48: 19-25. doi.org/10.1029/AR048

Lal, D., Rajan, R. S. and Tamhane, A. S., 1969. Chemical composition of nuclei of Z > 22 in cosmic rays using meteoric minerals as detectors. Nature, 221: 33-37.

Laslett, G. M., Kendall, W. S., Gleadow, A. J. W. and Duddy, I. R., 1982. Bias in measurement of fission-track length measurements. Nucl. Tracks Radiat. Meas., 6: 79-85. doi.org/10.1016/0735-245X(82)90031-X

LeMasurier, W. E. and Thomson, J. W., ed., 1990. Volcanoes of the Antarctic Plate and Southern Oceans. Antarct. Res. Ser., 48: 488. doi.org/10.1029/AR048

LeMasurier, W. E., 2008. Neogene extension and basin deepening in the West Antarctic rift inferred from comparisons with the East African rift and other analogs. Geology, 36: 247-250. doi.org/10.1130/G24363A.1.

LeMasurier, W. E., Choi, S. H., Kawachi, Y., Mukasa, S. B. and Rogers, N. W., 2011. Evolution of pantellerite-trachyte-phonolite volcanoes by fractional crystallization of basanite magma in a continental rift setting, Marie Byrd Land, Antarctica, Contrib. Mineral. Petrol., 162(6): 1175-1199. doi.org/10.1007/s00410-011-0646-z.

Levy, R., Cody, R., Crampton, G., Fielding, C., Golledge, N., Harwood, D., Henrys, S., Mckay R., Naish, T., Ohneiser, C., Wilson, G., Wilson, T. and Winter, D., 2012. Late Neogene climate and glacial history of the Southern Victoria Land coast from integrated drill core, seismic and outcrop data☆. Glob. Planet. Change, 96-97: 157-180.

Licht, K. J., Jennings, A.E., Andrews, J. T. and Williams, K. M., 1996. Chronology of late Wisconsin ice retreat from the western Ross Sea, Antarctica. Geology, 24(3): 223-226. doi.org/10.1130/0091-7613(1996)024%3C0223:COLWIR%3E2.3.CO;2.

Licht, K. J. and Fastook, J., 1998. Constraining a numerical ice sheet model with geologic data over one ice sheet advance/retreat cycle in the Ross Sea. Chapman Conference on the West Antarctic Ice Sheet, University of Maine, 25-26.

Licht, K. J., Dunbar, N. W., Andrews, J.T. and Jennings, A.E., 1999. Distinguishing subglacial till and glacial marine diamictons in the western Ross Sea, Antarctica: implications for a last glacial maximum grounding line. Geol. Soc. Am. Bull., 111(1): 91-103. doi.org/10.1130/0016-7606(1999)111%3C0091:DSTAGM%3E2.3.CO;2

Licht, K. J. and Andrews, J. T., 2002. A ^{14}C record of late Pleistocene ice advance and retreat in the central Ross Sea, Antarctica. Arct. Alp. Res., 34(3): 324-333. doi.org/10.1080/15230430.2002.12003501.

Licht, K. J., Lederer, J. R., and Swope, R. J., 2005. Provenance of LGM Glacial till (Sand Fraction) across the Ross Embayment, Antarctica. Quat. Sci. Rev., 24: 1499-1520. doi.org/10.1016/j.quascirev.2004.10.017.

Licht, K. J., Hennessy, A. J. and Welke, B. M., 2014. The U-Pb detrital zircon signature of West Antarctic ice stream tills in the Ross Embayment, with implications for Last Glacial Maximum ice flow reconstructions. Antarct. Sci., 26(6): 687-697. doi.org/10.1017/S0954102014000315.

Licht, K. J., and Hemming, S., 2017. Analysis of Antarctic glacigenic sediment provenance through geochemical and petrologic applications (Invited Review). Quat. Sci. Rev., 164: 1-24. doi.org/10.1016/j.quascirev.2017.03.009

Lisker, F. and Olesch, M., 1998. Cooling and Denudation History of Western Marie Byrd Land, Antarctica, Based on Apatite Fission-Tracks. doi.org/10.1007/978-94-015-9133-1_14.

Lisker, F., 2002. Review of fission track studies in northern Victoria Land, Antarctica - Passive margin evolution versus uplift of the Transantarctic Mountains. Tectonophysics, 349: 57-73. doi.org/10.1016/S0040-1951(02)00046-X.

Lisker, F., Läufer, A., Olesch, M., Rossetti, F. and Schäfer, T., 2006. The Transantarctic Beacon Basin: new insights from AFT data and structural data from the USARP Mountains and adjacent areas (northern Victoria Land, Antarctica). Basin Res., 18: 497-520. doi.org/10.1111/j.1365-2117.2006.00301.x.

Li, X., Zattin, M. and Olivetti, V., 2019. A Detrital Apatite Fission - Track Study of the CIROS - 2 Sedimentary Record: Tracing Ice Pathways in the Ross Sea Area over the Last 5 Ma. Terra Nova, 1-10. doi.org/10.1111/ter.12396.

MacAyeal, D. R. 1992. Irregular oscillations of the West Antarctic ice sheet. Nature, 359(6390): 29-32. doi.org/10.1038/359029a0

Malusà, M. G., and Fitzgerald, P. G., ed., 2018. Fission-Track Thermochronology and Its Application to Geology.

Malusà, M. G., and Garzanti, E., 2019. The Sedimentology of Detrital Thermochronology. In Fission-Track Thermochronology and its Application to Geology. Springer, Cham., 123-143.

Marchant, D. R., Swisher, C. C. and Berkeley, I., 1996. Late Cenozoic Antarctic Paleoclimate Reconstructed from Volcanic Ashes in the Dry Valleys Region of Southern Victoria Land. Quat. Res., 2: 181-94. doi.org/10.1130/0016-7606(1996)108%3C0181:LCAPRF%3E2.3.CO;2

McKay, R. M., Dunbar, G. B., Naish, T. R., Barrett, P. J., Carter, L. and Harper, M., 2008. Retreat history of the Ross Ice Sheet (Shelf) since the Last Glacial Maximum from deep-basin sediment cores around Ross Island. Palaeogeogr. Palaeoclimatol. Palaeoecol., 260(1-2): 245-261. doi.org/10.1016/j.palaeo.2007.08.015.

McKay, R., Browne, G., Carter, L., Cowan, E., Dunbar, G., Krissek, L., Naish, T., Powell, R., Reed, J., Talarico, F. and Wilch, T., 2009. The stratigraphic signature of the late Cenozoic Antarctic Ice Sheets in the Ross Embayment. GSA Bull., 121: 1537-1561. doi.org/10.1130/B26540.1

Milne, G. A., Gehrels, W. R., Hughes, C. W., and Mark, E., 2009. Identifying the Causes of Sea-Level Change. Nat. Geosci., 2: 471-478.

Miller, S. R., Fitzgerald, P. G. and Baldwin, S. L., 2010. Cenozoic range front faulting and development of the Transantarctic Mountains near Cape Surprise, Antarctica: Thermochronologic and geomorphologic constraints. Tectonics, 29: TC1003. doi.org/10.1029/2009TC002457

Molzahn, M., Wörner, G., Henjes-Kunst, F. and Rocholl, A., 1999. Constraints on the Cretaceous thermal event in the Transantarctic Mountains from alteration processes in Ferrar flood basalts. Glob. Planet. Change, 23: 45-60. doi.org/10.1016/S0921-8181(99)00050-8.

Mosola, A. B. and Anderson, J. B., 2006. Expansion and Rapid Retreat of the West Antarctic Ice Sheet in Eastern Ross Sea: Possible Consequence of over-Extended Ice Streams? Quat. Sci. Rev., 25: 2177-2196. doi.org/10.1016/j.quascirev.2005.12.013.

Mukasa, S. B. and Dalziel, I. W. D., 2000. Marie Byrd Land, West Antarctica: Evolution of Gondwana's Pacific margin constrained by zircon U-Pb geochronology and feldspar common-Pb isotopic compositions. Geol. Soc. Am. Bull., 112(4): 611-627. doi.org/10.1130/0016-7606(2000)112%3C611:MBLWAE%3E2.0.CO;2.

Naeser, C. W., Izett, G. A., Wilcox, R. E., 1973. Zircon fission-track ages of Pearlette family ash beds in Meade County, Kansas. Geology, 1: 187-189. doi.org/10.1130/0091-7613(1973)1%3C187:ZFAOPF%3E2.0.CO;2

Naeser, C. W., 1979. Fission track dating and geological annealing of fission tracks. In: Lectures in isotope, geology, Jäger, E. and Hunziker, J. C., ed., Springer-Verlag, New York, 154-169.

Naeser, C.W., 1981. The fading of fission tracks in the geological environment - data from deep drill holes. Nucl. Tracks Rad. Meas., 5: 248-250. doi.org/10.1016/0191-278X(81)90055-X

Naish T., Powell, R., Levy, R., Wilson, G., Scherer, R., Talarico, Krissek, F. L., Niessen, F., Pompilio, M., Wilson, T., Carter, L., DeConto, R., Huybers, P., McKay, R., Pollard, D., Ross, J., Winter, D., Barrett, P., Browne, G., Cody, R., Cowan, E., Crampton, J., Dunbar, G., Dunbar, N., Florindo, F., Gebhardt, C., Graham, I., Hannah, M., Hansaraj, D., Harwood, D., Helling, D., Henrys, S., Hinnov, L., Kuhn, G., Kyle, P., Laufer, A., Maffioli, P., Magens, D., Mandernack, K., McIntosh, W., Millan, C., Morin, R., Ohneiser, C., Paulsen, T., Persico, D., Raine, I., Reed, J., Riesselman, C., Sagnotti, L., Schmitt, D., Sjunneskog, C., Strong, P., Taviani, M., Vogel, S., Wilch, T.

and Williams, T., 2009. Obliquity-paced Pliocene West Antarctic ice sheet oscillations. Nature, 458: 322-329. doi.org/10.1038/nature07867

Nicholas, R. G, Levy, R. H., McKay, R. M., Fogwill, C. J., White, D. A., Graham, A. G. C., Smith, J. A., Hillenbrand C., Licht, K. J., Denton, G. H., Ackert, R. P., Maas, S. M. and Hall, B. L., 2013. Glaciology and geological signature of the Last Glacial Maximum Antarctic ice sheet. Quat. Sci. Rev., 78: 225-247. doi.org/10.1016/j.quascirev.2013.08.011.

Olivetti, V., Balestrieri, M. L., Rossetti, F. and Talarico, F. M., 2013. Tectonic and climatic signals from apatite detrital fission track analysis of the Cape Robert Project core records, south Victoria Land, Antarctica. Tectonophysics, 594: 80-90. doi.org/10.1016/j.tecto.2013.03.017

Olivetti, V., Balestrieri, M. L., Rossetti, F., Thomson, S. N., Talarico, F. M. and Zattin, M., 2015. Evidence of a full West Antarctic Ice Sheet back to the early Oligocene: Insight from double dating of detrital apatites in Ross Sea sediments. Terra Nova, 27: 238-246. doi.org/10.1111/ter.12153

Olivetti, V., Rossetti, F., Balestrieri, M. L., Pace, D., Cornamusini, G. and Talarico, F., 2018. Variability in uplift, exhumation and crustal deformation along the Transantarctic Mountains front in southern Victoria Land, Antarctica. Tectonophysics, 745: 229-244. doi.org/10.1016/j.tecto.2018.08.017

O'Sullivan, P. B. and Parrish, R. R., 1995. The importance of apatite composition and single grain ages when interpreting fission track data from plutonic rocks: a case study from the Coast Ranges, British Columbia. Earth Planet. Sci. Lett., 132: 213-224. doi.org/10.1016/0012-821X(95)00058-K

O'Sullivan P. B., Morwood, M., Hobbs, D., Aziz, F., Suminto, Situmorang, M., Raza, A. and Maas, R., 2001. Archeological implications of the geology and chronology of the Soa Basin, Flores, Indonesia. Geology, 29: 607-610. doi.org/10.1130/0091-7613(2001)029%3C0607:AIOTGA%3E2.0.CO;2

Pankhurst, R. J., Weaver, S. D. Bradshaw, J. D. Storey, B. C. and Ireland, T. R., 1998. Geochronology and geochemistry of pre-Jurassic superterranes in Marie Byrd Land, Antarctica, J. Geophys. Res., 103(B2): 2529-2547. doi.org/10.1029/97JB02605.

Paul, T. A., 1993. Transmission electron microscopy investigation of unetched fission tracks in fluorapatite-physical process of annealing. Nucl. Tracks Radiat. Meas., 21:507-511. doi.org/10.1016/1359-0189(93)90190-K

Perotti, M., Andreucci, B., Talarico, F. and Zattin M., 2017. Multi-analytical provenance analysis of Eastern Ross Sea LGM till sediments (Antarctica): Petrography, geochronology, and thermochronology detrital data. Geochem. Geophy. Geosy., 2275-2304. doi.org/10.1002/2016GC006728.

Perotti, M., Zurli, L., Sandroni, S., Cornamusini, G. and Talarico, F., 2018. Provenance of Ross Sea Drift in McMurdo Sound (Antarctica) and Implications for Middle-Quaternary to LGM Glacial Transport: New Evidence from Petrographic Data. Sediment. Geol., 371: 41-54. doi.org/10.1016/j.sedgeo.2018.04.009.

Pollard, D., and Deconto, R. M., 2009. Modelling West Antarctic Ice Sheet Growth and Collapse through the Past Five Million Years. Nature, 458(7236): 329-32. doi.org/10.1038/nature07809.

Prenzel, J., Lisker, F., Elsner, M., Schoner, R., Balestrieri, M. L., A. L. Läufer, Berner, U. and Spiegel, C., 2014. Burial and exhumation of the Eisenhower Range, Transantarctic Mountains, based on thermochronological, sedimentary rock maturity and petrographic constraints, Tectonophysics, 630: 113-130. doi.org/10.1016/j.tecto.2014.05.020

Reiners, P. W. and Ehlers, T. A., ed., 2005. Low Temperature Thermochronology: Techniques, Interpretations, Applications. Reviews in Mineralogy and Geochemistry, Chantilly, VA: Mineral. Soc. Am., Geochem. Soc., 58: 622.

Reiners, P. W. and Brandon, M., 2006. Using Thermochronology to Understand Orogenic Erosion. Annu. Rev. Earth Planet. Sci., 34: 419-466. doi: 10.1146/annurev.earth.34.031405.125202.

Rignot, E., Bamber, J. L., Van Den Broeke, M. R., Davis, C., Li, Y., Van De Berg, W. J. and Van Meijgaard, E., 2008. Recent Antarctic Ice Mass Loss from Radar Interferometry and Regional Climate Modelling. Nat. Geosci., 1: 106-110. doi.org/10.1038/ngeo102.

Roberts, A. P., Wilson, G. S., Harwood, D. M. and Verosub, K. L., 2003. Glaciation across the Oligocene-Miocene boundary in southern McMurdo Sound, Antarctica: new chronology from the CIROS-1drill hole. Palaegeogr. Palaeoclimatol. Palaeoecol., 198: 113-130. doi.org/10.1016/S0031-0182(03)00399-7

Ruiz, G. M. H., Seward, D. and Winkler, W., 2004. Detrital thermochronology - a new perspective on hinterland tectonics, an example from the Andean Amazon Basin, Ecuador. Basin Res.. doi.org/10.1111/j.1365-2117.2004.00239.x

Saito, S., Brown, M., Korhonen, F. J., McFadden, R. R. and Siddoway, C. S., 2013. Petrogenesis of Cretaceous mafic intrusive rocks, Fosdick Mountains, West Antarctica: Melting of the sub-continental arc mantle along the Gondwana margin, Gondwana Res., 23(4): 1567-1580. doi.org/10.1016/j.gr.2012.08.002.

Sandroni, S. and Talarico F. M., 2006. Analysis of clast lithologies from CIROS-2 core, New Harbour, Antarctica—Implications for ice flow directions during Plio-Pleistocene time. Palaegeogr. Palaeoclimatol. Palaeoecol., 231: 215-232. doi.org/10.1016/j.palaeo.2005.07.031

Shipp, S., Anderson, J. B., Domack, E. W., 1999. Late Pleistocene-Holocene retreat of the West Antarctic Ice Sheet system in the Ross Sea: part 1-geophysical results. Geol. Soc. Am. Bull., 111(10): 1486-1516. doi.org/10.1130/0016-7606(1999)111%3C1486:LPHROT%3E2.3.CO;2.

Shipp, S. S., Wellner J. S. and Anderson J. B., 2002. Retreat Signature of a Polar Ice Stream: Sub-Glacial Geomorphic Features and Sediments from the Ross Sea, Antarctica. Geol. Soc. Am. Bull., London, Special Publications, 203(1): 277-304 doi.org/10.1144/GSL.SP.2002.203.01.15

Siddoway, C. S., Richard, S. M., Fanning, C. M. and Luyendyk, B. P., 2004a. Origin and emplacement of a Middle Cretaceous gneiss dome, Fosdick Mountains, West Antarctica, in Gneiss. Gneiss Domes in Orogeny. doi.org/10.1130/0-8137-2380-9.267

Siddoway, C. S., Baldwin, S. L., Fitzgerald, P. G., Fanning, C. M. and Luyendyk, B. P., 2004a. Ross Sea mylonites and the timing of intracontinental extension within the West Antarctic rift system. Geology, 32: 57-60. doi:10.1130/G20005.1.

Siddoway, C. S., Sass, L. C. and Esser, R. P., 2005. Kinematic history of the Marie Byrd Land terrane, West Antarctica: Direct evidence from Cretaceous mafic dykes. In: Terrane Processes at the Margin of Gondwana, Vaughan, A., Leat, P. and Pankhurst, R. J., ed., Geol. Soc. London, Special Pub., 246: 417-438. doi.org/10.1144/GSL.SP.2005.246.01.17.

Spiegel, C., Lindow, J., Kamp, P. J. J., Meisel, O., Mukasa, S., Lisker, F., Kuhn, G., and Gohl, K., 2016. Tectonomorphic Evolution of Marie Byrd Land— Implications for Cenozoic Rifting Activity and Onset of West Antarctic Glaciation FRWARS. Global Planet. Change ,145: 98-115. doi.org/10.1016/j.gloplacha.2016.08.013.

Staiger, J. W., Marchant, D. R., Schaefer, J. M., Oberholzer, P., Johnson, J. V., Lewis, A. R. and Swanger, K. M., 2006. Plio-Pleistocene history of Ferrar Glacier, Antarctica: Implications for climate and ice sheet stability. Earth Planet. Sci. Lett., 243: 489-503. doi.org/10.1016/j.epsl.2006.01.037

Storti, F., Balestrieri, M. L., Balsamo, F. and Rossetti, F., 2008. Structural and thermochronological constraints on the evolution of the West Antarctic Rift System in central Victoria Land. Tectonics, 27: TC4012. doi.10.1029/2006TC002066.

Stuiver, M., Denton, G. H., Hughes, T. J. and Fastook, J. L., 1981. History of the marine ice sheets in West Antarctica during the last glaciation: a working hypothesis. In: The Last Great Ice Sheets, Denton, G. H. and Hughes, T. J. ed., Wiley-Interscience, New York, 319-439.

Stump, E. and Fitzgerald, P. G., 1992. Episodic uplift of the Transantarctic Mountains. Geology, 20: 161-164. doi.org/10.1130/0091-7613(1992)020<0161:EUOTTM>2.3.CO;2

Sumii, T., Tagami, T. and Nishimura, S., 1987. Anisotropic etching character of spontaneous tracks in zircon. Nucl. Tracks Radiat. Meas., 13: 275-277. doi.org/10.1016/1359-0189(87)90039-2

Tagami, T. and O'Sullivan, P. B., 2005. Fundamentals of fission-track thermochronology. Rev. Mineral. Geochem., 58: 19-47. doi.org/10.2138/rmg.2005.58.2

Talalay, P. G. and Pyneb, A. R., 2017. Geological drilling in McMurdo Dry Valleys and McMurdo Sound, Antarctica: Historical development. Cold Reg. Sci. Technol., 141: 131-162. doi.org/10.1016/j.coldregions.2017.06.007

Tinto, K. J., Padman, L., Siddoway, C. S., Springer, S.R., Fricker, H. A., Das, I., Caratori Tontini, F., Porter, D. F., Frearson, N.P., Howard, S. L., Siegfried, M. R., Mosbeux, C., Becker, M. K., Bertinato, C., Boghosian, A., Brady, N., Burton, B. L., Chu, W., Cordero S. I., Dhakal, T., Dong, L., Gustafson, C. D., Keeshin, S., Locke, C., Lockett, A., O'Brien, G., Spergel, J. J., Starke, S. E., Tankersley, M., Wearing, M. G. and Bell, R. E., 2019. Ross Ice Shelf response to climate driven by the tectonic imprint on seafloor bathymetry. Nat. Geosci. 12, 441-449. doi:10.1038/s41561-019-0370-2

Vaughan, D. G., Comiso, J. C., Allison, I., Carrasco, J., Kaser, G., Kwok, R., Mote, P., Murray T., Paul, F., Ren, J., Rignot, E., Solomina, O., Steffen, K. and Zhang, T., 2013. Observations: Cryosphere. In: Climate Change 2013: The Physical Science Basis. Contribution of Working Group I to the Fifth Assessment Report of the

Intergovernmental Panel on Climate Change, Stocker, T. F., Qin, D., Plattner, G. K., Tignor, M., Allen, S. K., Boschung, J., Nauels, A., Xia, Y., Bex, V. and Midgley, P. M., ed., Cambridge University Press, Cambridge, United Kingdom and New York, NY, USA.

Vermeesch, P., 2012. On the visualisation of detrital age distributions. Chem. Geolog., 312-313, 190-194. doi.org/10.1016/j.chemgeo.2012.04.021

Vermeesch, Pieter., 2013. Multi-Sample Comparison of Detrital Age Distributions. Chemical Geology, 341: 140–46. doi.org/10.1016/j.chemgeo.2013.01.010.

Vetter, J., Scholz, R., Dobrev, D. and Nistor, L., 1998. HREM investigation of latent tracks in GeS and mica induced by high energy ions. Nucl. Instr. Methods B, 141: 747-752. doi.org/10.1016/S0168-583X(98)00198-0

Wagner, G. A., 1968. Fission track dating of apatites. Earth Planet Sci. Lett., 4: 411-415. doi.org/10.1016/0012-821X(68)90072-1

Warren, G. A., 1969. Geology of Terra Nova Bay-McMurdo Sound Area Victoria Land (Sheet 14). In: Geologic Maps of Antarctic Plate XIII, Bushnell, V. C. and Craddock, C., ed., Antarctic Map Folio Series, Folio 12. Washington, DC; American Geographical Society.

Wagner, G. A., 1972. The geological interpretation of fission track ages. Trans. Am. Nucl. Soc., 15:117.

Wagner, G. A. and Van den haute, P., 1992. Fission-Track Dating. Kulwer Academy, Norwell, Massachusetts., 285.

Weaver, S. D., Bradshaw, J. D. and Adams, C. J., 1991. Granitoids of the Ford Ranges, Marie Byrd Land, Antarctica. In: Geological Evolution of Antarctica, Thompson, M. R. A. et al., ed., Cambridge Univ. Press, Cambridge, Mass., 345-351.

Weaver, S. D., Adams, C. J., Pankhurst, R. and Gibson, I. L., 1992. Granites of Edward VII Peninsula, Marie Byrd Land: Anorogenic magmatism related to Antarctic-New Zealand rifting, Earth Environ. Sci. Trans. R. Soc. Edinb., 83(1-2): 281-290, doi.org/10.1017/S0263593300007963.

Welke, B., Licht, K., Hennessy, A., Hemming, S., Pierce Davis, E. and Kassab, C., 2016. Applications of detrital geochronology and thermochronology from glacial deposits to the Paleozoic and Mesozoic therma l history of the Ross Embayment, Antarctica, Geochem.Geophys. Geosyst., 17: 2762-2780. doi:10.1002/2015GC005941

Yakymchuk, C., Brown, C. R. Brown, M., Siddoway, C. S., Fanning, C. M. and Korhonen, F. J., 2015. Paleozoic evolution of western Marie Byrd Land, Antarctica. Geol. Soc. Am. Bull., 127(9-10):1464-1484. doi.org/10.1130/B31136.1.

Zattin, M., Talarico, F. and Sandroni, S., 2010. Integrated provenance and detrital thermochronology studies in the ANDRILL AND-2A drill core: Late Oligocene-Early Miocene exhumation of the Transantarctic Mountains (southern Victoria Land, Antarctica). Terra Nova, 22: 361-368. doi.org/10.1111/j.1365-3121.2010.00958.x

Zattin, M., Andreucci, B., Thomson, S. N., Reiners, P. W. and Talarico, F. M., 2012. New constraints on the provenance of the ANDRILL AND-2A succession (western Ross Sea, Antarctica) from apatite triple dating. Geochem. Geophys. Geosyst., 13: Q10016. doi.org/10.1029/2012GC004357

Zattin, M., Pace, D., Andreucci, B., Rossetti, F. and Talarico, F. M., 2014. Cenozoic erosion of Transantarctic Mountains: a source-to-sink thermochronological study. Tectonophysics, 630: 158-165. doi.org/10.1016/j.tecto.2014.05.022